Optical Bistability and Stimulated Brillouin Scattering in a Nonlinear Fiber Resonator

THESIS

OPTICAL BISTABILITY AND STIMULATED BRILLOUIN SCATTERING IN A NONLINEAR FIBER RESONATOR

Hongpu LI

Graduate School
of
Science and Engineering

Shizuoka University

January 2000

THESIS

OPTICAL BISTABILITY AND STIMULATED BRILLOUIN SCATTERING IN A NONLINEAR FIBER RESONATOR

(非線形ファイバ共振器中の光双安定性及び誘導ブリルアン散乱)

李 洪譜

静岡大学

大学院理工学研究科

システム科学専攻

平成１２年１月

Acknowledgments

I would like to express my sincerely thanks to my supervisor, Professor Kazuhiko Ogusu, not only for selecting me as a Ph.D. student and helping me to apply for Monbusho Scholarship, but also for his earnest, careful, and patient guidance throughout all my research works.

I would like to thank Professor Akira Sasaki, Professor Hiroo Komura, Professor Akira Ichikawa, and Professor Junji Otsubo for their carefully reviewing and valuable comments on the manuscript. Also I would like to express my thanks to the many other professors at Shizuoka University, who offered me various helps in the experiment.

I would like to thank the Japanese Ministry of Education, Science, and Culture for providing me the scholarship during my studies in Japan. With it, I could concentrate all my attentions on this research.

I am greatly indebted to all of my friends in Ogusu' s laboratory.

Finally, I would give my deepest thanks to my wife and my son for their love, their support, understanding and patience during this period. Thanks also give to my parents and the parents of my wife, for their encourage and support.

Abstract

In this study, fiber-typed optical bistable devices, especially the kinds of fiber Fabry-Perot resonator and double-coupler fiber ring resonator have been studied in detail. Transient effect of stimulated Brillouin scattering (SBS), interplay between Kerr effect and Brillouin gain effect in a fiber and one-coupler fiber ring resonator has also been investigated in detail to give a guidance to the design of optical bistable devices. All contents are organized in seven chapters.

In chapter 1, a simple description for the background and purposes of this study has been given.

In chapter 2, experimental study for the nonlinear absorption and nonlinear refraction of BDN (bis(4-dimethylaminodithiobenzil)-nickel) in nitrobenzene solution is reported. First, saturable absorption properties of BDN are determined by using a transmission method. The response time of the dye solution is about 1.5 ns. Next, the nonlinear refraction is investigated by using a single beam z-scan and a two-color z-scan methods. It is found that the main origin of the nonlinear refractive index change is not the population redistribution of the dye molecules but the thermal effect. In particular, the nonlinear refraction in the nanosecond regime is attributed to density change due to propagation of an acoustic wave excited by the laser pulses. It is expected that the results and discussions presented in this chapter will be applicable for many absorbing materials.

In chapter 3, two iterative methods have been described for calculating the dynamic properties of the plane Fabry-Perot resonator filled with nonlinear fiber itself. The iterative method based on the midpoint rule however is not suitable because of numerical instability. Moreover, a steady-state analysis and linear stability analysis have been presented. The threshold powers for Ikeda instability in the bistable device have been examined. It is found that optical bistability is hardly affected by Ikeda instability since the instability threshold is much higher than the bistability switching power for the initial detuning where the bistable device is operated.

In chapter 4, the iterative method have been presented for calculating the dynamic properties of the double-coupler nonlinear fiber ring resonator when

an optical pulse with an arbitrary temporal profile is incident on it. Furthermore, a linear stability analysis has been performed to examine whether Ikeda instability affects bistable device application or not. Nearly the same results as that of chapter 3 have been obtained.

In chapter 5, theoretical and experimental results for the dynamics of SBS in a single-mode fiber have been given. It is found that SBS can occur even in the nanosecond region and steady state of SBS can be obtained when the pulse width of the incident light is 100-fold greater than that of the round-trip time within the fiber. Following the process of the transient SBS, pulse narrowing for the transmitted pulse is also observed. Moreover, it is found that SBS instability can occur when the nonlinear refractive index is one order of magnitude larger than that of the fused-silica fiber.

In chapter 6, theoretical results for the transient SBS and transient interplay between Kerr effect and Brillouin gain effect in a fiber ring resonator have been given. It is found that owing to the interaction of the nonlinear refraction with the SBS gain effect, a Stokes wave in the ring resonator is generally unstable for a high incident power. These instabilities depend strongly on the pump power and the parameters of the fiber resonator, including the finesse and the initial phase detuning of the cavity. It is also found that due to the occurrence of SBS, optical bistability described in chapter 4 cannot be observed in a fiber ring resonator made of fused-silica fiber. However, if other optical fibers with nonlinear refractive index at least one order larger than that of fused-silica fiber are used, transient optical bistability may be obtained at low power.

In chapter 7, all the results obtained from the above chapters are summarized. It is assured that in order to demonstrate optical bistability on experiment, SBS must be restrained in a fiber resonator. The most attractive way is the utilization of other kinds of fibers with nonlinear refractive index at least one order larger than that of fused-silica fiber. This method will make the optical bistability appeared at a power lower than the SBS threshold. As matter of the fact, large nonlinearity with two order larger than that of silica fiber has already been found in chalcogenide glass fibers, which make the exploitation of fiber optical bistable device probable. Further study for the restraint of SBS in a fiber ring resonator is needed.

Contents

Chapter 1. Introduction

1.1 Basis of Optical Nonlinear Effects

In intense electromagnetic fields, the response of optical fiber becomes nonlinear. As a result, the induced polarization P is not linear in the electric field E, but is expressed in power of the electric field:

$$P = \varepsilon_0 \left(\chi^{(1)} E + \chi^{(2)} EE + \chi^{(3)} EEE + \cdots \right), \tag{1.1}$$

where ε_0 is the free-space permittivity and $\chi^{(j)}$ (j=1, 2, $\cdots$) is jth order susceptibility. $\chi^{(j)}$ is a tensor of rank j+1. The linear susceptibility $\chi^{(1)}$ represents the dominant contribution to P. It can be divided into the linear refractive index n and the linear attenuation coefficient α. The second-order susceptibility $\chi^{(2)}$ is responsible for such nonlinear effects as second-harmonic generation and sum-frequency generation. However, it vanishes for silica fiber since SiO_2 is a symmetry molecular. The lowest-order nonlinear effects in a fiber originate from the third-order susceptibility $\chi^{(3)}$, which is responsible for the phenomena such as third-harmonic generation, four-wave mixing, and nonlinear refraction. However, the first two phenomena rarely occur unless the condition of phase matching is given, the last one is the most efficient nonlinear effect in a fiber.

A. Nonlinear Refraction

Nonlinear refraction refers to the intensity dependence of the refractive index resulting from the contribution of $\chi^{(3)}$, i.e., the refractive index is expressed by

$$n(|E|^2) = n_0 + n_2 |E|^2, \tag{1.2}$$

where n_0 is linear refractive index of the fiber, $|E|^2$ is the optical intensity inside the fiber, and n_2 is nonlinear refractive index related to $\chi^{(3)}$ by the relation

$$n_2 = \frac{3}{8n} \mathrm{Re}\left(\chi^{(3)}_{xxxx} \right), \tag{1.3}$$

where Re stands for the real part and the optical field is assumed to be linearly polarized so that only one component $\chi^{(3)}_{xxxx}$ of the fourth-rank tensor contributes to the refractive index.

B. Self- and Cross-phase modulation

The intensity dependence of the refractive index leads to a large number of interesting nonlinear effects; the two most widely studied are self-phase modulation (SPM) and cross-phase modulation (XPM). SPM refers to the self-induced phase shift experienced by an optical field during its propagation in optical fibers. The phase of an optical field changes by

$$\phi = nk_0L = (n + n_2|E|^2)k_0L, \tag{1.4}$$

where k_0 is the wave number and L is the fiber length. The intensity-dependent nonlinear phase shift $\phi_{NL} = n_2k_0L|E|^2$ is due to SPM.

XPM refers to the nonlinear phase shift of an optical field induced by a copropagating field at a different wavelength. When two optical fields at frequencies ω_1 and ω_2 copropagate simultaneously inside the fiber, the nonlinear phase shift for the fields at ω_1 and ω_2 are then given by

$$\phi_{NL}(\omega_1) = n_2k_0L(|E_1|^2 + 2|E_2|^2), \tag{1.5}$$

$$\phi_{NL}(\omega_2) = n_2k_0L(2|E_1|^2 + |E_2|^2). \tag{1.6}$$

The two terms on the right-hand of the Eq. (1.5) (Eq. (1.6)) are due to SPM (XPM) and XPM (SPM), respectively. The most important characteristic of XPM is that, for equally intense optical fields, the contribution of XPM to the nonlinear phase shift is twice compared with that of SPM.

1.2 Enhancement of Nonlinearities in a Single-mode Fiber

Table 1.1 shows the nonlinear effects and parameters for various materials [1], [2]. As is shown, the nonlinear refractive index of the fused-silica fiber is

Table 1.1 Nonlinear effects and parameters for various materials [1].

Nonlinear Effect	Typical material	$\|n_2\|$ (m^2/V^2)	τ (s)	α_0(cm^{-1})
Band filling	GaAs etc.	$\sim10^{-9}$	$\sim10^{-8}$	$\sim10^{2}$
Super lattice	GaAs/GaAlAs MQW	$\sim10^{-7}$	$\sim10^{-8}$	$\sim10^{4}$
π-electron excitation	PTS etc.	$\sim10^{-14}$	$<10^{-14}$	$\sim10^{-1}$
Thermal refraction	Zns, ZnSe etc.	$\sim10^{-10}$	$10^{-3}\sim1$	
Molecular orientatio	CS_2, Nitrobenzene	$\sim10^{-17}$	$\sim10^{-12}$	$\sim10^{-3}$
Liquid crystal	TN liquid crystal	$10^{-8}\sim10^{-6}$	~1	—
Photorefractive	$Bi_{12}SiO_{20}$, $BaTiO_3$	—	$\sim10^{-3}$	—
Kerr effect in SiO_2	Fused-silica fiber	$\sim10^{-22}$ [2]	$<10^{-14}$	$\sim10^{-5}$ [2]

about 1.0×10^{-22} m^2/V^2. Compared to most of other bulk nonlinear materials, it is found that this value is much small. In spite of this, the nonlinear effects in a optical fibers can be observed at relatively lower power level. Single-mode optical fiber is an attractive medium for nonlinear optics, because of its long interaction length, small core diameter with several micrometers, and extremely low loss (<1 dB/km). A figure of merit for the efficiency of nonlinear process in bulk media is the product $I\times L_{eff}$ where I is the optical intensity and L_{eff} is the effective length of the interaction. The ratio of this merit of single-mode fiber to that of bulk can be expressed by [2]

$$\frac{(I\cdot L_{eff})_{fiber}}{(I\cdot L_{eff})_{bulk}}=\frac{\lambda}{\pi\omega_0^2\alpha_0}, \tag{1.7}$$

where ω_0 is the beam spot size which is dependent on the fiber core radius. α_0 is the fiber loss. It is easily to see that the enhancement factor is in the range of 10^7 $\sim10^9$ for a conventional single-mode fiber. It is this tremendous enhancement in the efficiency of nonlinear processes that makes the fiber a suitable nonlinear medium for the observation of wide variety of nonlinear effects at relatively low power levels. Moreover, large enhancements can also be obtained by enclosing a single-mode fiber in an optical resonator. In this case, both the circulating intensity and the effective path length are increased, and threshold effects such as stimulated Brillouin scattering and optical bistability will appear. Most of the nonlinear effects and their applications reported to date are summarized in Table 1.2. Here we concen-

Table 1.2 Nonlinear effects in optical fiber and their applications.

Nonlinear effect	Application
Stimulated Brillouin scattering Stimulated Raman scattering	Light wavelength change Fiber optical amplifier Fiber sensor Mode-locked laser Pulse compression
Optical Kerr effect	Pulse shaping Optical switching Optical bistability
Four-wave mixing	Parametric amplification Squeezing Fiber sensor
Self- and cross-phase modulation	Optical Soliton transmission Optical pulse compression Fiber coupler
Photosensitive effect	DFB laser Narrow-band filter Temperature and pressure sensor
Second-harmonic generation	Light source Wavelength change

trate our study on the application of optical bistability and stimulated Brillouin scattering in a fiber resonator.

1.3 Fiber-typed Optical Bistable Devices

Bistability is a very common characteristic of nonlinear feedback system and can be found in many different fields such as ferromagnetism, electronics, or chemistry. The phenomenon of optical bistability was first predicted by Szoke et al. in 1969 [3] and then observed in a Fabry-Perot resonator filled with sodium [4]. Since then, optical bistability has been observed in different types of nonlinear resonators using materials with various nonlinearity mechanisms [5-11]. Optical bistable device refers to that the optical system could exhibit two states of output for the same input, a typical example of the input-output characteristics in such a device is shown in Fig. 1.1. For each incident power P_{in}, the transmission remains low until P_{in} is increased beyond the critical value P_{SH} (called switch-on power). The transmission then remains high even as P_{in} is decreased until another critical value P_{SL} (called switch-off power) is reached, and the device jumps to the off state. This type

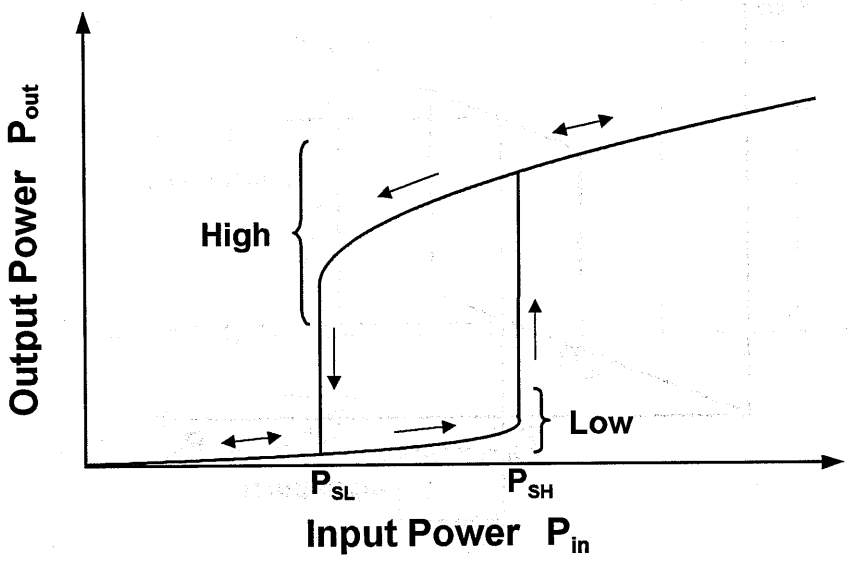

Fig. 1.1. Typical input-output characteristics for an optical bistable device.

of hysteresis is considered as evidence for optical bistability. Such a device could be used to perform many fundamental operations, such as optical latching switch, optical logic gate, pulse shaper, power limiter, and differential amplifier, etc. [12], some of them are shown in Fig. 1.2. So far, all observations of bistability have involved a combination of nonlineaities and feedback. Depending on the nonlinearities, optical bistability can be absorptive, increasing absorption, or dispersive. In the case of absorptive bistability, a saturable medium is generally inserted into a resonator [11,13]. Increasing-absorption optical bistability is based on an increase of the absorption at the operating wavelength with an increased of laser intensity. This kind of optical bistability is generally obtained in a semiconductor. For dispersive bistability, a medium with intensity-dependent refractive index is inserted into a resonator, which is based on optical Kerr effect. Recently, this kind of fiber optical bistable devices have received considerable attention because of the strong enhancement of fiber nonlinearities and their potential direct application to optical signal processing for optical communications.

The configurations of fiber bistable devices proposed to date can be classified into three groups as shown in Fig. 1.3. The first is in-line nonlinear

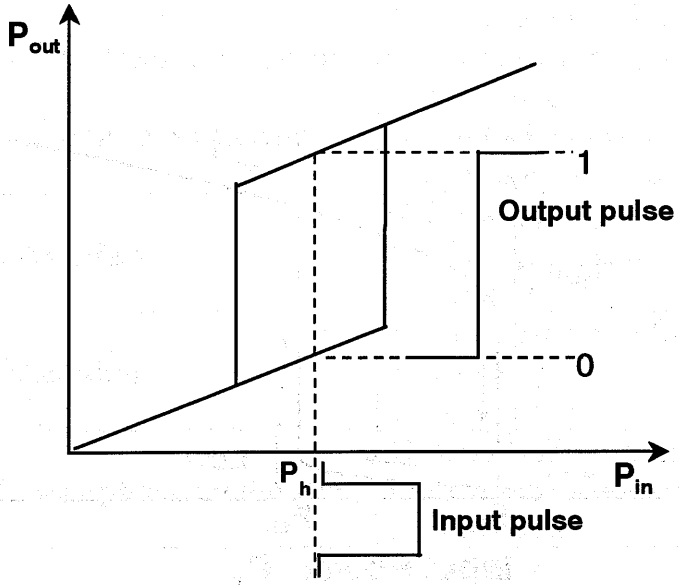

(a) latching switch

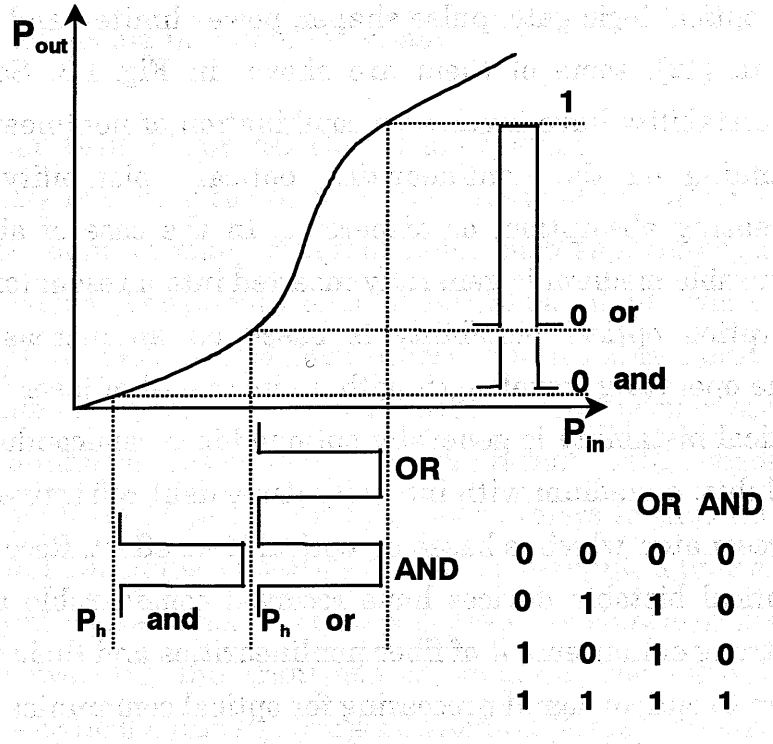

(b) logic gate

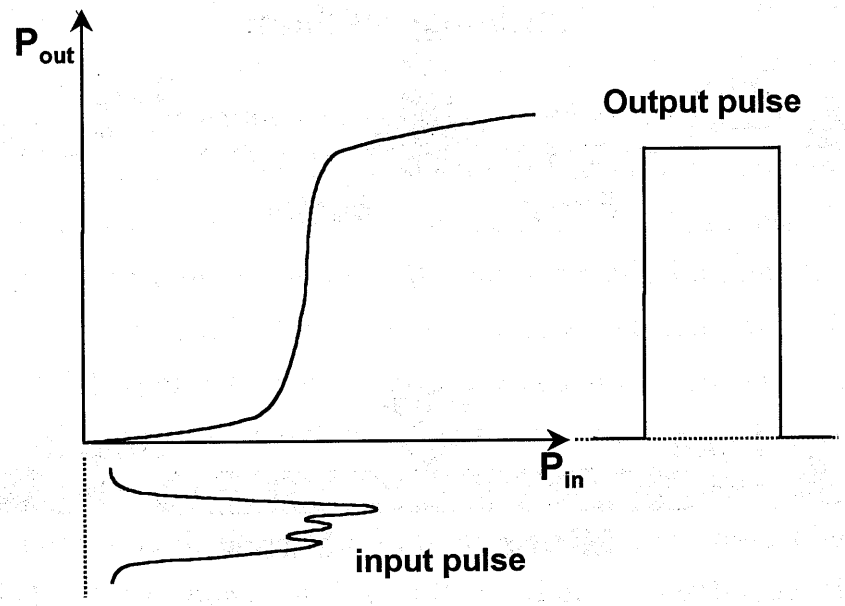

(c) pulse shaper

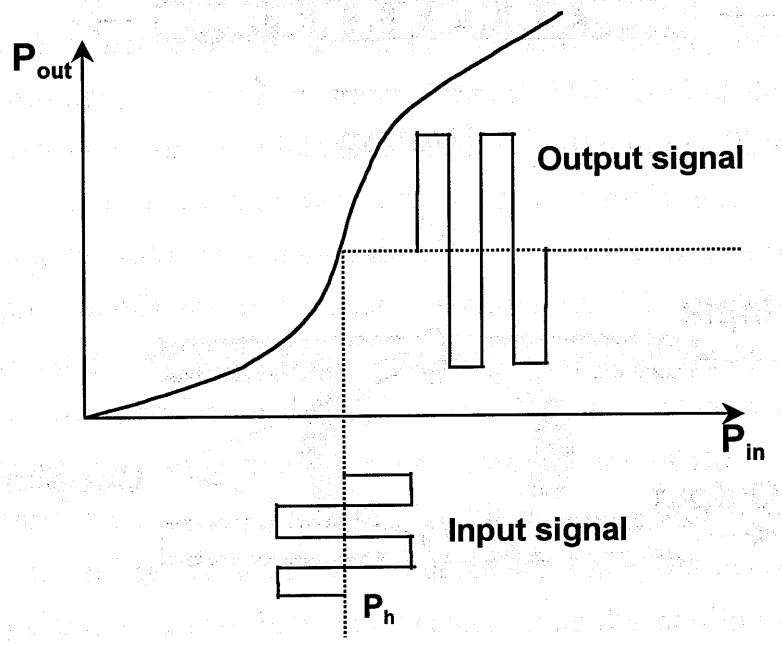

(d) differential amplifier

Fig. 1.2. Basic optical circuit elements: (a) latching switch, (b) logic gate, (c) pulse shaper, (d) differential amplifier.

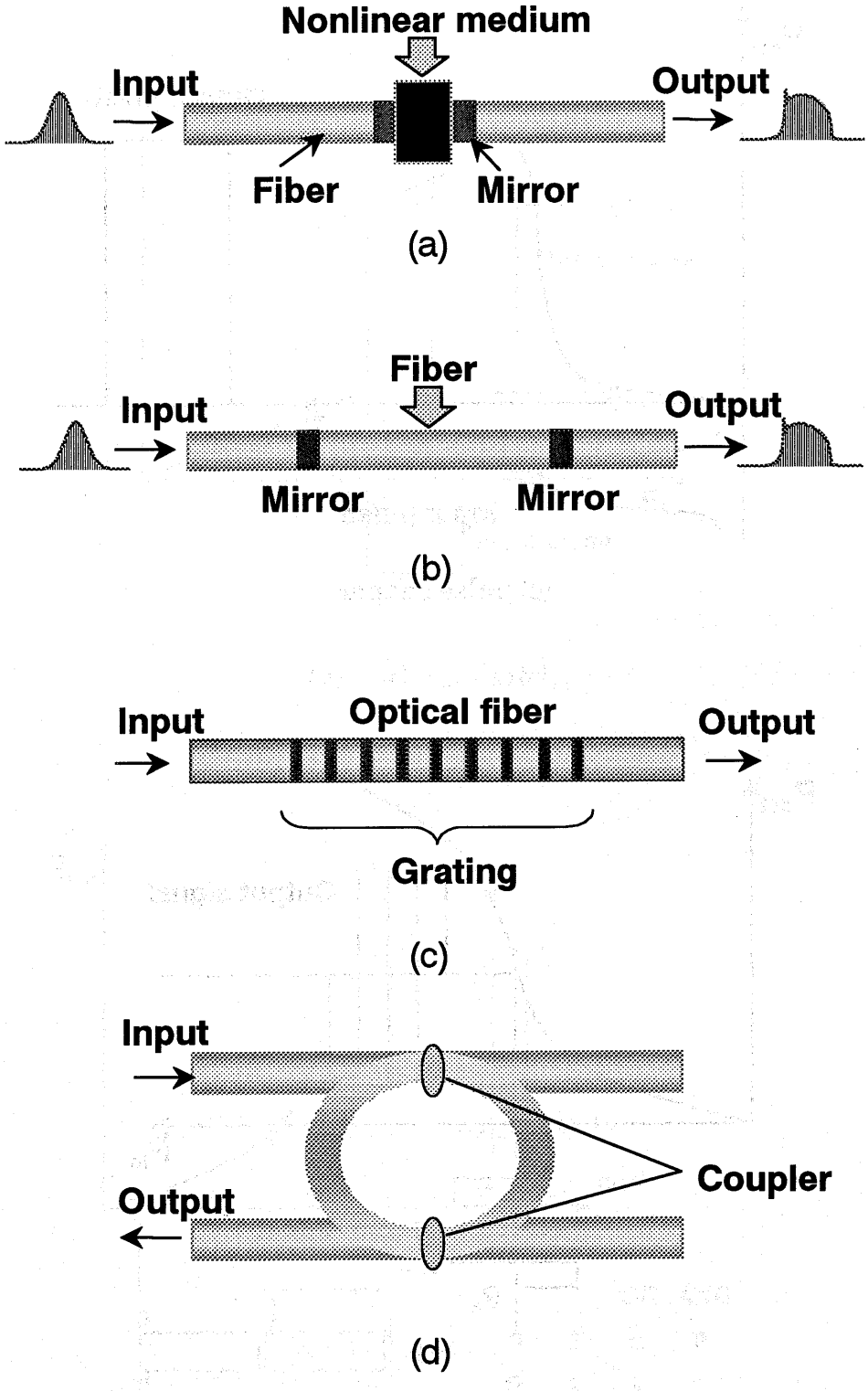

Fig. 1.3. Schematic of fiber-typed optical bistable devices: (a) medium-embedded resonator, (b) all-fiber Fabry-Perot resonator, (c) fiber grating resonator, and (d) fiber ring resonator.

Fabry-Perot resonator [10] including the medium-embedded fiber Fabry-Perot and all fiber Fabry-Perot resonator, as shown in Figs. 1.3(a) and (b), respectively. For the one shown in Fig. 1.3(a), a nonlinear material is embedded in a fiber resonator. Here a saturable absorber seems to be one of the best nonlinear materials. At the wavelength of 1.06 μm, bistable optical device using a saturable absorber BDN (bis(4-dimethylaminodithio-benzil)-nickel) has been reported [11]. It is generally believed that optical bistability observed in Ref. [11] arises from an intensity-dependent phase change due to the refractive index difference between the ground and first triplet states of the dye molecules and is not thermal, and that the dye is a potential nonlinear material [14]. The second group refers to nonlinear fiber grating resonator [15-17] as shown in Fig. 1.3(c), where a nonlinear distributed feedback structure (also called Brag fiber grating) is inserted into a fiber. The refractive index is periodically changed inside the fiber-grating region, bistable phenomenon can be observed in this device while no mirror is needed. The third is nonlinear fiber ring resonator, typical example is shown in Fig. 1.3(d), which consists of a fiber loop and two coupler called double-coupler nonlinear fiber ring resonator [18-20]. This kind of devices is based on the intensity-dependent phase shift accumulated over a fiber ring and one can decrease the switching power by making the ring longer.

So far, steady-state optical bistability in a nonlinear Fabry-Perot [21], a single-coupler nonlinear fiber ring resonator [22-24], double-coupler nonlinear fiber ring resonator, fiber double-ring resonator [25] and nonlinear fiber loop mirror with feedback [26] have been investigated theoretically. The double-coupler nonlinear fiber ring resonator is one of the most important configurations since transmission bistability is available in addition to reflection bistability as well as a nonlinear Fabry-Perot resonator. The operating principle of the fiber ring resonator or the nonlinear Fabry-Perot resonator is well understood using the steady-state analysis, for example, the graphical method developed by Marburger and Felber [21]. Transient analysis for the nonlinear Fabry-Perot resonator was first studied by Bischofberger and Shen [27] using the so-called multiple-beam interference method. Until present, the transient analyses of a single-coupler fiber ring resonator [28], [29], double-coupler fiber ring resonator [19], [30] and non-

linear fiber loop mirror with feedback [31] have already been carried out by using a multiple-beam interference method developed by Bischofberger and Shen or an iterative method developed by Ikeda [32]. However the iterative method has not yet been reported for the nonlinear Fabry-Perot resonator and the double-coupler fiber ring resonator.

In other respect, one feature of the dynamics of ring cavity or Fabry-Perot resonator containing a nonlinear medium with an instantaneous response time is the existence of instabilities. Ikeda et al. have first found that a fiber cavity can exhibit periodic and chaotic instabilities under certain conditions [32], [33]. Therefore dynamic properties including instabilities are very important for the design and implementation of bistable optical devices.

1.4 Stimulated Brillouin Scattering

Brillouin scattering is the scattering of light from acoustic disturbance in a medium. The principle of Brillouin scattering is illustrated schematically in Fig. 1.4 [34], where an incident optical wave interacts with an incoming or outgoing acoustic wave. Conservation of momentum and energy requires that the frequency and wave vector of the scattered wave (ν_s, k_s) be related to those of incident wave (ν_p, k_p) by the relations

$$\nu_s = \nu_p \pm \nu_A, \quad k_s = k_p \pm k_A, \tag{1.8}$$

where $\pm k_A$ and ν_A are the wave vector and frequency of acoustic wave, respectively. The negative sign in Eq. (1.8) corresponds to the Stokes-shifted wave scattered from an outgoing acoustic wave, and the positive sign corresponds to the anti-Stokes wave. The frequency shift of the Brillouin scattered wave is a maximum for $\theta = 180°$ scattering (i.e., backscattering). At this angle the frequency shift is called the Brillouin frequency and is defined as

$$\nu_B = 2\frac{v_A}{c/n_0}\nu_p, \tag{1.9}$$

where v_A is the velocity of the acoustic wave, n_0 is the linear refractive indexes, and c/n_0 is the velocity of the light in the medium. Spontaneous

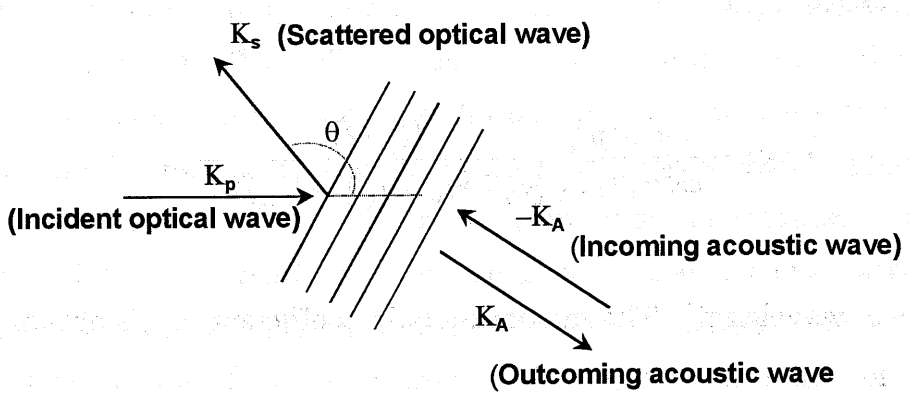

Fig. 1.4. The principle scheme of the Brillouin scattering.

Brillouin scattering occurs due to scattering from thermally excited phonons.

In laser scattering from acoustic disturbance, the incident laser and Brillouin scattered wave superimpose to form a traveling beat wave with frequency ν_A and wave vector k_A. If the laser is sufficiently intense, this beat wave can coherently drive the acoustic wave through electrostrictive, and possibly thermal forces. The enhanced acoustic wave more strongly scatters the incident laser radiation, which in return leads to a stronger beat wave. The mutual reinforcement results in an amplified Brillouin wave. The process is called stimulated Brillouin scattering (SBS). The most important parameters of SBS are the gain coefficient g_B and the acoustic lifetime (phonon damping time) Γ_A^{-1}. In general, SBS gain coefficient (SI units) is expressed as [34]

$$g_B = \frac{\gamma_e^2 \omega_p^2}{\varepsilon_0^2 \rho_0 n v_A c^3 \Gamma_A} \frac{(\Gamma_A/2)^2}{\left[\nu_B - (\nu_p - \nu_s)\right]^2 + (\Gamma_A/2)^2}, \tag{1.10}$$

where ρ_0 and n are the average density and the linear refractive indexes of the medium. γ_e is the electrostrictive coefficient. For solid material, it is given as

$$\gamma_e = \varepsilon_0 \rho_0 \frac{\partial \varepsilon}{\partial \rho} = \varepsilon_0 \rho_0 n^4 p_{12}, \tag{1.11}$$

where p_{12} is the photo-elastic constant of the medium. Equation (1.10) can also be expressed as

$$g_B = \frac{2\pi^2 n^7 p_{12}^2}{c\lambda^2 \rho_0 v_A \Gamma_A} \frac{(\Gamma_A/2)^2}{[\nu_B - (\nu_p - \nu_s)]^2 + (\Gamma_A/2)^2}, \tag{1.12}$$

λ is optical wavelength. The maximum gain coefficient g_{B0} is obtain

$$g_{B0} = \frac{2\pi^2 n^7 p_{12}^2}{c\lambda^2 \rho_0 v_A \Gamma_A}, \tag{1.13}$$

where it is noted that $\Gamma_A = 1/\tau_A = \pi\Delta\nu_B$, $\Delta\nu_B$ is the Brillouin linewidth (FWHM).

In a single-mode fiber, one can easily decrease the SBS threshold by increasing the fiber length. It is known that SBS can be produced at an input power level of a few milliwatts for a several kilometers single-mode fiber [35-37]. Dynamic behavior of SBS in a single-mode fiber was first investigated by Ippen and Stolen [38]. They found that there existed a relaxation oscillation in the Stokes radiation intensity. This phenomenon has been confirmed by Bar-Joseph et al. [39] and Dianov et al. [40] The pulse width used in these experiments is in the range of 0.2 to 1.0 μs, which is one or two order larger than the phonon damping time of the fiber. For SBS, if the pump-pulse width is less than or roughly equal to the phonon damping time, the transient effects must be considered. Dynamic behavior of SBS for a short fiber under a short pulsed pump (in a time region which is nearly the same order of magnitude as the phonon lifetime) has not been reported to date.

Compared with SBS in a single-mode fiber, SBS in a short and high-finesse fiber ring resonator is not widely studied to date. Steady state of SBS in a fiber ring resonator was first investigated by Stokes et al. [41] who presented a simple equation for the dependence of the Brillouin threshold on the resonator finesse and showed that the threshold of SBS would be greatly reduced in the resonator of high finesse. This result has also been confirmed

by Kadiwar and Giles [42], [43] through measuring the variation of finesse in a polarization-maintaining fiber ring resonator for changing input power. Since the transient effect of the acoustic wave and optical Kerr effect inducing self- and cross-phase modulations have been neglected in their theoretical model, no information about the instability of SBS has been given. Besides the above works, SBS in a cw-pumped low-finesse fiber ring resonator (also called Brillouin fiber ring laser) has recently attracted a considerable interest because of its varied types of dynamic behaviors [44-49]. The most important feature of this device is the existence of periodic intensity modulation in the created Stokes signal, which is also called self-pulsing and has recently been studied by Montes et al. in detail [44]. It is known that SBS instabilities including periodic, quasi-periodic and chaotic oscillations may arise only when the length of the fiber cavity is large enough [44], [46]. The experimental results also show that the Brillouin emission is stable for a short fiber at any input power. Therefore, physical origin of the instabilities in the fiber ring resonator is attributed to the existence of a large number of longitudinal modes beneath the Brillouin gain curve rather than the optical Kerr effect [44], [48]. Among most of the previous papers, both the pump and Stokes waves are assumed to be resonant within the cavity. The linear phase detuning of cavity for either the circulating pump wave or the Stoke waves has not been considered. Moreover, compared with researches into many different nonlinear effects and phenomena associated with optical fiber such as self- and cross-phase modulation, research for the effect of stimulated Brillouin scattering on optical bistability in a fiber ring resonator is less understood. This information is necessary for us to develop optical bistable devices in a high-finesse fiber ring resonator.

1.5 Purposes of this Study

In this study, fiber-typed optical bistable devices, especially the kinds of fiber Fabry-Perot resonator and double-coupler fiber ring resonator will be investigated in detail. Moreover, the transient effect of stimulated Brillouin scattering, the interplay between Kerr effect and Brillouin gain effect in a fiber and one-coupler fiber ring resonator will be investigated in order to give a guidance to the design of fiber bistable devices. All the works are outlined

as follows:

First, we investigate the nonlinear absorption and nonlinear refraction of BDN in nitrobenzene solution and to examine its potential utilization as nonlinear material for the development of a medium-embedded fiber bistable device with a response time less than several nanoseconds.

Second, we present an iterative method for analyzing the transient properties of the nonlinear Fabry-Perot resonator and apply it to perform a linear stability in terms of the input power.

Third, we perform a transient analysis of a double-coupler nonlinear fiber ring resonator using an iterative method and examine the instability. Investigate in detail the dynamic properties of optical bistability and instability to gain a good guide for demonstrating optical bistability in the double-coupler fiber ring resonator. Make sure whether Ikeda instability affect bistable device application or not.

Fourth, we examine the dynamic behavior of SBS in a single-mode fiber in a time region which has nearly the same order of magnitude as the phonon lifetime.

Fifth, we investigate the transient SBS in a fiber ring resonator and determine the factors which give rise to a instability in the output Stokes signal. Moreover, we investigate the transient interplay of the Kerr effect with the SBS gain effect in a fiber ring resonator try to determine whether the optical bistability could be observed in a fiber ring resonator.

References

[1] 神谷武志 編 「光情報材料」 丸善株式会 p. 173-178

[2] G. P. Agrawal, *Nonlinear Fiber Optics* (Academic, New York, 1995) Chap. 9.

[3] A. Szoke, V. Daneu, J. Goldhar, and N. A. Kurnit, "Bistable optical element and its applications," Appl. Phys. Lett. 15 (1969) 376.

[4] H. M. Gibbs, S. L. McCall, and T. N. C. Venkatesan, "Differential gain and bistability using a sodium-filled Fabry-Perot interferometer," Phys. Rev. Lett. 36 (1976) 1135.

[5] H. M. Gibbs, S. S. Tarng, J. L. Jewell, D. A. Weinberger, K. Tai, A. C. Gossard, S. L. McCall, A. Passner, and W. Wiegmann, "Room-temperature excitonic optical bistability in a GaAs-GaAlAs superlattice etalon," Appl. Phys. Lett. 41 (1982) 221.

[6] J. Yumoto, S. Fukushima, and K. Kubodera, "Observation of optical bistability in $CdS_{\chi}Se_{1-\chi}$-doped glasses with 25-psec switching time," Opt. Lett. 12 (1987) 832.

[7] A. C. Walker, J. S. Aitchison, S. Ritchie, and P. M. Rodgers, "Intrinsic optical bistability and multistability in a passive GaAlAs waveguide," Electron. Lett. 22 (1986) 366.

[8] B. G. Kim and E. Garmire, "Optical bistability and nonlinear switching due to increasing absorption in single-crystal ZnSe waveguides," Appl. Phys. Lett. 51 (1987) 475.

[9] M. Warren, W. Gibbons, K. Komatsu, D. Sarid, D. Hendricks, H. M. Gibbs, and M. Sugimoto, "Electronic optical bistability in GaAs/AlGaAs strib-loaded waveguide," Appl. Phys. Lett. 51 (1987) 1209.

[10] K. Ogusu and S. Yamamoto, "Nonlinear fiber Fabry-Perot resonator using thermo-optic effect," IEEE J. Lightwave Technol. 11 (1993) 1774.

[11] Z. F. Zhu and E. M. Garmire, "Optical Bistability in BDN Dye," IEEE J. Quantum Electron. QE-19 (1983) 495.

[12] H. M. Gibbs, *Optical Bistability: Controlling Light with Light* (Academic Press, Orlando, 1985).

[13] E. Arimondo, D. Dangoisse, C. Gabbanini, E. Menchi, and F. Papoff, "Dynamic behavior of bistability in a laser with a saturble absorbtion," J. Opt. Soc. Am. B 4 (1987) 892.

[14] A. Yabe, Y. Taniguchi, H. Masuhara, and H. Matsuda, *Yükichohaku-maku Nyumon* (*Introduction to ultra-thin organic films*), (Baifukan, Tokyo, 1989) p.191 [in Japanese].

[15] H. G. Winful, J. H. Marburger, and E. Garmire, "Theory of bistability in nonlinear distributed feedback structures," Appl. Phys. Lett. **35** (1979) 379.

[16] C. M. de Sterke and J. E. Sipe, "Switching dynamics of finite periodic nonlinear media: A numerical study," Phys. Rev. A **42**, (1990) 2858.

[17] B. J. Eggleton, C. M. de Sterke, R. E. Slusher, and J. E. Sipe, "Distributed feedback pulse generator based on nonlinear fibre grating," Electron. Lett. **32** (1996) 2341.

[18] F. J. Fraile-Peláez, J. Capmany, and M. A. Muriel, "Transmission bistability in a double-coupler fiber ring resonator," Opt. Lett. **16** (1991) 907.

[19] K. Ogusu, H. Shigekuni, and Y. Yokota, "Dynamic transmission properties of a nonlinear fiber ring resonator," Opt. Lett. **20** (1995) 2288.

[20] T. Fukushima and T. Sakamoto, "Kerr-effect-induced S-R flip-flop operation in an optical fiber loop resonator with double couplers," Opt. Lett. **20** (1995) 1119.

[21] J. H. Marburger and F. S. Felber, "Theory of a lossless nonlinear Fabry-Perot interferometer," Phys. Rev. A **17** (1978) 335.

[22] B. Crosignani, B. Daino, P. Di Porto, and S. Wabnitz, "Optical multistability in a fiber-optic passive-loop resonator," Opt. Commun. **59** (1986) 309.

[23] Y. H. Ja, "Kerr bistability in a 3×3 coupler optical fiber ring resonator," Appl. Opt. **32** (1993) 5310.

[24] L. Luo and P. L. Chu, "Optical bistability in a coupled fiber ring resonator system with nonlinear absorptive medium," Opt. Commun. **129** (1996) 224.

[25] Y. H. Ja, "Multiple bistability in an optical-fiber double-ring resonator utilizing the Kerr effect," IEEE J. Quantum Electron. **30** (1994) 329.

[26] C.-X. Shi, "Nonlinear fiber loop mirror with optical feedback," Opt. Commun. **107** (1994) 276.

[27] T. Bischofberger and Y. R. Shen, "Theoretical and experimental study of the dynamic behavior of a nonlinear Fabry-Perot interferometer," Phys. Rev. A 19 (1979) 1169.

[28] K. Ogusu, "Dynamic behavior of reflection optical bistability in a nonlinear fiber ring resonator," IEEE J. Quantum Electron. 32 (1996) 1537.

[29] K. Ogusu, A. L. Steele, J. E. Hoad, and S. Lynch, "Corrections to and comments on "dynamic behavior of reflection optical bistability in a nonlinear fiber ring resonator"," IEEE J. Quantum Electron. 33 (1997) 2128.

[30] F. J. Fraile-Peláez, M. Prol, D. J. Santos, and J. M. Soto-Crespo, "Transient analysis of a nonlinear fiber ring resonator," Appl. Phys. Lett. 63 (1993) 1477.

[31] A. L. Steele, S. Lynch, and J. E. Hoad, "Analysis of optical instabilities and bistability in a nonlinear optical fiber loop mirror with feedback," Opt. Commun. 137 (1997) 136.

[32] K. Ikeda, "Multiple-valued stationary state and its instability of the transmitted light by a ring cavity system," Opt. Commun. 30 (1979) 257.

[33] K. Ikeda, H. Daido, and O. Akimoto, "Optical turbulence: chaotic behavior of transmitted light from a ring cavity," Phys. Rev. Lett. 45 (1980) 709.

[34] R. L. Sutherland, *Handbook of Nonlinear Optics* (Marcel Dekker, New York, 1996) Chap. 13.

[35] N. Uesugi, M. Ikeda, and Y. Sasaki, "Maximum single frequency input power in a long optical fibre determined by stimulated Brillouin scattering," Electron. Lett. 17 (1981) 379.

[36] D. Cotter, "Observation of stimulated Brillouin scattering in low-loss silica fiber at 1.3 μm," Electron. Lett. 18 (1982) 495.

[37] Y. Aoki, K. Tajima, and I. Mito, "Observation of stimulated Brillouin scattering in single-mode fibres with single-frequency laser-diode pumping," Opt. Quantum Electron. 19 (1987) 141.

[38] E. P. Ippen and R. H. Stolen, "Stimulated Brillouin scattering in optical fibers," Appl. Phys. Lett. 21 (1972) 539.

[39] I. Bar-Joseph, A. A. Friesem, E. Lichtman, and R. G. Waarts, "Steady and relaxation oscillations of stimulated Brillouin scattering in single-mode optical fibers," J. Opt. Soc. Am. B 2 (1985) 1606.

[40] E. M. Dianov, A. Ya. Karasik, A. V. Lutchnikov, and A. N. Pilipetskii, "Saturation effects at backward-stimulated scattering in the single-mode regime of interaction," Opt. Quantum Electron. 21 (1989) 381.

[41] L. F. Stokes, M. Chodorow, and H. J. Shaw, "All-fiber stimulated Brillouin ring laser with submilliwatt pump threshold," Opt. Lett. 7 (1982) 509.

[42] R. Kadiwar and I. P. Giles, "Effects of stimulated Brillouin scattering on the performance of polarization-maintaining all-fiber ring resonators," Opt. Lett. 14 (1989) 332.

[43] P. Bayvel, I. P. Giles, and P. M. Radmore, "Transient and steady-state characteristics of a Brillouin amplifier based on an all-fiber single-mode ring resonator, " Opt. Quantum Electron. 21 (1989) S113.

[44] C. Montes, D. Bahloul, I. Bongrand, J. Botineau, G. Cheval, A. Mamhoud, E. Picholle, and A. Picozzi, "Self-pulsing and dynamic bistability in cw-pumped Brillouin fiber ring lasers," J. Opt. Soc. Am. B 16 (1999) 932.

[45] C. Montes, A. Mamhoud, and E. Picholle, "Bifurcation in a cw-pumped Brillouin fiber-ring laser: Coherent soliton morphogenesis," Phys. Rev. A 49 (1994) 1344.

[46] S. Randoux, V. Lecoeuche, B. Segard, and J. Zemmouri, "Dynamical analysis of Brillouin fiber lasers: An experimental approach," Phys. Rev. A 51 (1995) 4345.

[47] S. Randoux, V. Lecoeuche, B. Segard, and J. Zemmouri, "Dynamical behavior of a Brillouin fiber ring laser emitting two Stokes components," Phys. Rev. A 52 (1995) 2327.

[48] V. Lecoeuche, B. Segard, and J. Zemmouri, "Modes of destabilization of Brillouin fiber ring lasers," Opt. Commun. 134 (1997) 547.

[49] E. Picholle and A. Picozzi, "Guided-acoustic-wave resonances in the dynamics of simulated Brillouin fiber ring laser," Opt. Commun. 135 (1997) 327.

Chapter 2. Optical Bistable Device Based on a Saturable Absorber BDN

2.1 Introduction

In this chapter, the nonlinear absorption and nonlinear refraction of BDN in nitrobenzene are studied in detail using a nonlinear transmission method [1] and two kinds of z-scan methods [2], [3], respectively, to examine its potential application as nonlinear material for the development of a novel fiber bistable device with a response time less than 2~3 ns. We show that the main origin of the intensity-dependent refractive index change is neither the population redistribution of the dye molecules nor the saturable absorption, but thermal effect.

2.2 Saturable Absorption of BDN

BDN is a nickel complex and has a strong absorption in the infrared region. The absence of fluorescence from the dye at 1.06 μm or any other infrared wavelength and a response time of 0.2~9 ns were reported [4], [5]. Structural formula of BDN is shown in Fig. 2.1, which is the transition-metal complex. Absorption spectrum of BDN in a mixture of nitrobenzene is shown in Fig. 2.2. From the figure, we can see that there exists strong absorption in the near infrared waveband. The electronic structure of this dye molecule can be described by a four-level model as shown in Fig. 2.3. Energy levels 1 and 2

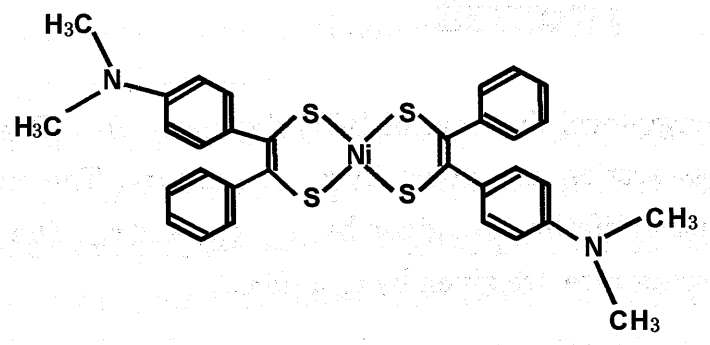

Fig. 2.1. Structural formula of BDN.

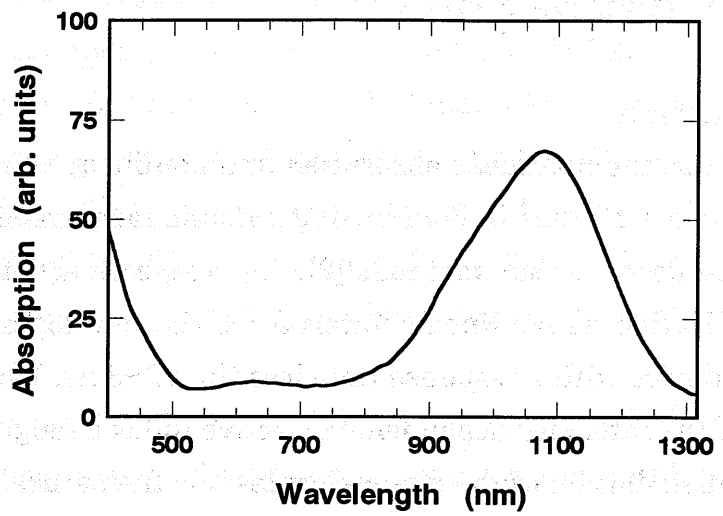

Fig. 2.2. Absorption spectrum of BDN in a mixture of nitrobenzene.

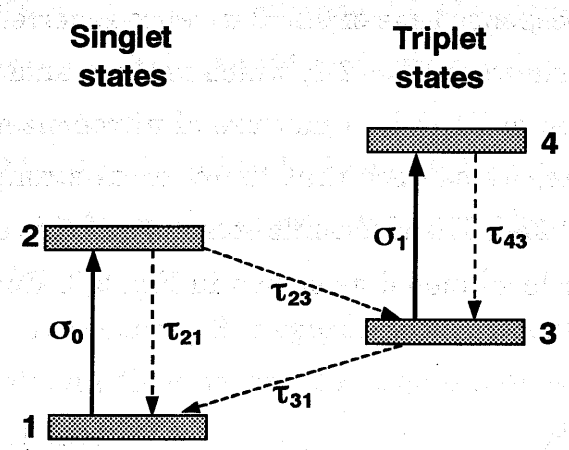

Fig. 2.3. Energy-level diagram of BDN dye molecules. The absorption cross section are given by σ_0, σ_1, and σ_2. The intralevel relaxation lifetime are given by τ_{21}, τ_{32}, and τ_{54}. The intersystem crossing rate are given by τ_{24} and τ_{41}.

are the ground state and the first excited singlet state, respectively, and levels 3 and 4 are the excited triplet states. σ_0 and σ_1 are the absorption cross sections for the 1-2 and 3-4 transitions, respectively. τ_{21}, τ_{31}, and τ_{43} are the

relaxation times of levels 2, 3, and 4, respectively. When a laser pulse is incident into a absorbing dye sample, optical excitation from the ground state 1 to the first singlet state 2 takes place and then the excited state relaxes very quickly to the lowest triplet state 3 ($\tau_{23} \approx 0$). In general, the relaxation rate from the higher-lying triplet state is very fast, i.e., $\tau_{43} \approx 0$. Therefore the population of level 4 can be ignored and the response time τ of the dye is given by the transition time τ_{31}. Saturable absorption or reverse saturable absorption of many organic dyes can be explained by using such a four-level model. From the rate equations of the four-level model, the steady-state optical intensity I in the dye sample is given by [6]

$$\frac{dI}{dz} = -I\alpha_0 \frac{I_s + \eta I}{I_s + I}, \tag{2.1}$$

where z is the depth in the medium, $I_s = (h\nu/\sigma_0\tau_{31})(\tau_{23}/\tau_{21} + 1) \approx h\nu/\sigma_0\tau_{31}$ is the saturation intensity, $\eta = \sigma_1/\sigma_0$ is the cross section ratio, and $\alpha_0 (= N\sigma_0$, where N is the total density of the dye) is the absorption coefficient of the ground state. Solving Eq. (2.1) for an incident intensity I_{in} at z=0, the transmittance T of the sample with thickness d is given by

$$T = T_0 \exp\left[(\eta - 1)\ln\left(\frac{\eta I_s + I_{in}}{\eta I_s + T I_{in}}\right)\right], \tag{2.2}$$

where $T_0 = \exp(-\alpha_0 d)$ is the linear transmittance for $I_{in} \to 0$. If $\eta < 1$, i.e., $\sigma_1 < \sigma_0$, saturable absorption is obtained. If $\eta > 1$, i.e., $\sigma_1 > \sigma_0$, reverse saturable absorption is obtained [1].

In our experiment, we use a Q-switched YLF laser operating at 1.047 μm as the light source and nitrobenzene as the solvent of BDN because of its high boiling point and good solvability. The thickness of the sample is 160 μm. Repetition rate of the pulses is 100 Hz and the pulse width is 22.5 ns. The laser beam is focused at the sample position with a focal lens to obtain a high optical intensity. Moreover we use a neutral-density filter to change the incident intensity while keeping the temporal and spatial profiles of the incident pulses constant. To decrease the effect of self-defocusing of the beam

in the dye solution on the output power measurement, we detect the total transmitted beam through a lens. Figure 2.4 shows the measured transmittance T as a function of the input intensity for four BDN concentrations. The BDN solution exhibits saturable absorption. We investigate the saturable absorption properties using the four-level model. The most important parameters are the saturation Intensity I_s and the ratio of two absorption cross sections η. We can easily determine these parameters by fitting the experimental data to the theoretical values calculated from Eq. (2.2). The solid lines in Fig. 2.4 are the best-fit curves. Moreover we can obtain the response time τ of BDN in nitrobenzene and the nonsaturable absorption coefficient α_1 by using $\tau = h\nu/\sigma_0 I_s$ and $\alpha_1 = \eta\alpha_0$, respectively. All results obtained from the best fit are summarized in Table 2.1. The excited state is less absorbing than the ground state (i.e., $\eta=\sigma_1/\sigma_0<1$) and the magnitude of η increases slightly with increasing BDN concentration. The calculated response time is about 1.5 ns, which agrees with experimental data in Ref. [5], where the response times for different solvents were measured by using a flash-photolysis technique.

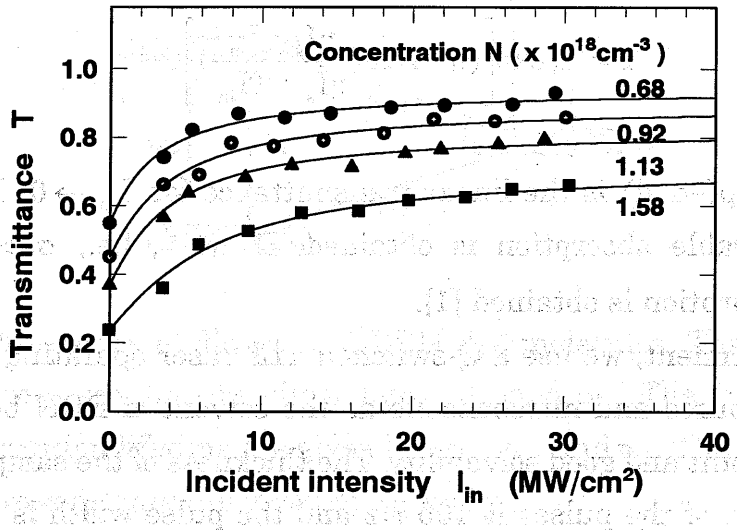

Fig. 2.4. Transmittance of BDN in nitrobenzene solution versus the incident intensity for four BDN concentrations N. The solid curves are theoretical predictions based on Eq. (2.2).

Table 2.1. Linear and nonlinear parameters of BDN in nitrobenzene at various concentrations N. Here $\eta = \sigma_1 / \sigma_0$ and $\alpha_1 = \eta\alpha_0$.

$N(x10^{18}cm^{-3})$	$\sigma_0(x10^{-17}cm^2)$	$\alpha_0(cm^{-1})$	$I_s(MW/cm^2)$	η	$\alpha_1(cm^{-1})$	τ (ns)
0.68	5.6	37.6	2.0	0.10	3.8	1.7
0.92	5.6	51.5	2.3	0.13	6.7	1.5
1.13	5.6	62.7	2.0	0.19	11.9	1.7
1.58	5.6	87.7	2.7	0.22	19.3	1.3

2.3 Nonlinear Refractive Index Change

A. Experiment Using the Single Beam Z-scan Method

The single beam z-scan method [2] is used to determine the change in the nonlinear refractive index. Principle of this method is illustrated in Fig. 2.5 Light transmits through a thin sample with the focal lens. The transmittance of a sample is measured through a finite aperture in the far field as the sample is moved along the direction of light propagation. Due to the nonlinear refractive index of the sample, the medium acts like intensity-dependent lens, whether it is negative or positive lens depend on the sign of the nonlinear refractive index of the sample. Such lens' effect will make the aperture transmittance (as function of sample position) depend on the magnitude and the sign of nonlinear refractive index (n_2). For example, a material with positive n_2, as shown in Fig. 2.5, for $z<0$, the lensing effect would causes the beam to come to focus earlier, so that it diverges more rapidly in the far field. This result is that the aperture transmittance decreases. On the other hand, for $z>0$, the lensing effect causes the beam divergence to decrease, resulting in an increased aperture transmittance. Near $z=0$, this lensing effect has little effect on a focused beam. Obviously, a material with negative n_2 will produce a similar curve, but with the peak and valley reversed about $z=0$. If a Gaussian TEM_{00} beam is focused on a thin nonlinear medium, then the following approximation equation can be obtained [2]

$$\Delta T_{p-V} \approx \pm 0.406(1-S)^{0.25}\left|\Delta\Phi_0\right|, \qquad (2.3)$$

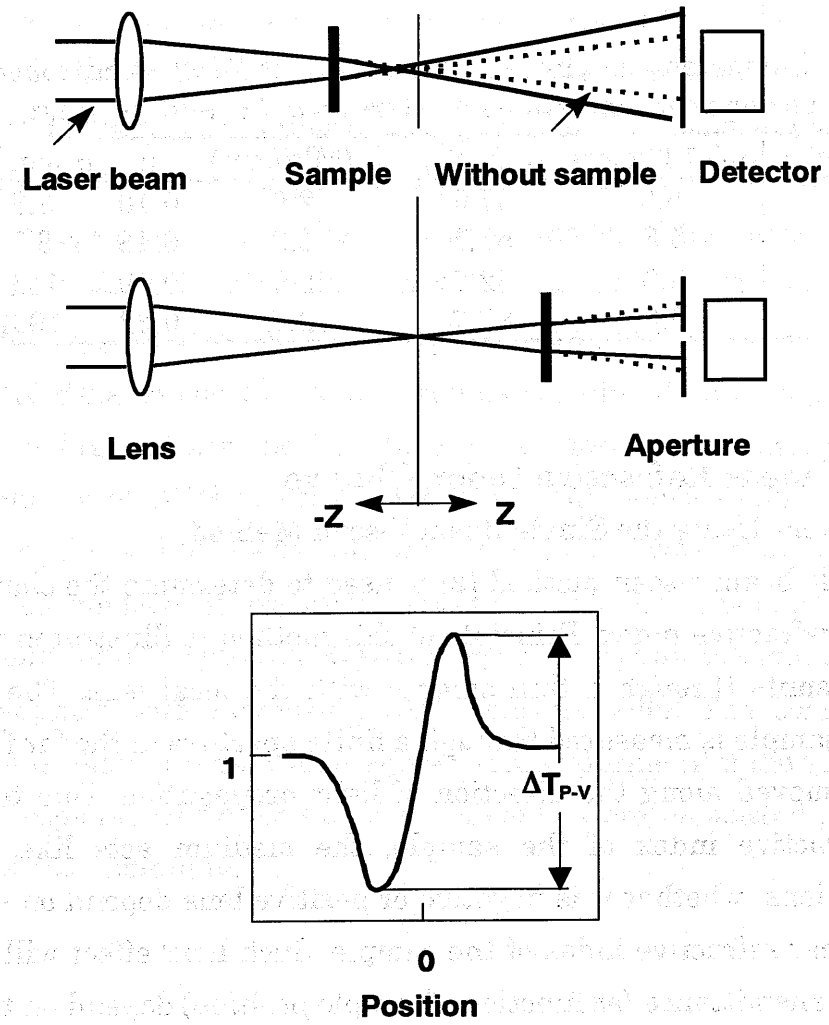

Fig. 2.5. Principle of the z-scan method.

where ΔT_{p-V} is the difference between the normalized peak and valley transmittance (as shown in Fig. 2.5), S is the linear transmittance and $\Delta\Phi_0$ is the change of on-axis phase. The sign and magnitude of the nonlinear refraction can be deduced from such a transmittance curve (z-scan).

In the experiment, we use the same light source and the same sample cell in all the experiments. The concentration of BDN is 0.68×10^{18} cm^{-3}. A 70-mm focal-length lens provides a tight focusing and the spot size ω is about 47 μm. An aperture is placed at a distance of 30 cm from the sample and its linear transmittance S is 0.4. Figure 2.6 shows an example of the experimental results, where the average input power is 1.32 mW and the repetition rate of incident pulses is 100 Hz. Figure 2.6(a) is the measured z-scan transmittance with a fully-open aperture (S=1). Since the z-scan trace without an aperture

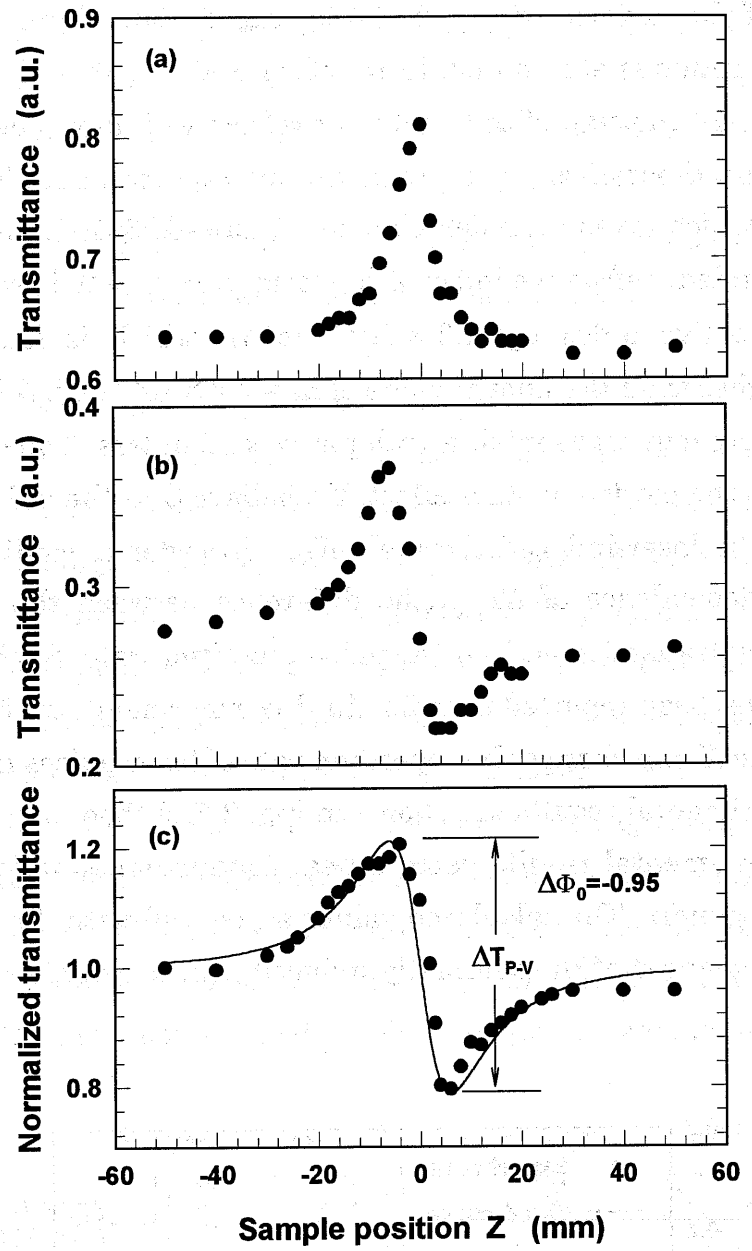

Fig. 2.6. Single beam z-scan results. (a) no aperture (S = 1), (b) 40% aperture (S = 0.4), and (c) normalized results of the division of (b)/(a). The solid curve is the theoretical fit with $\Delta\Phi_o$ = -0.95.

is insensitive to nonlinear refraction, only the effect of nonlinear absorption can be obtained. The transmittance has a peak at the focus (z=0), which is the property of a saturable absorber. In this case, the incident intensity at the focus is 8 MW/cm^2. Figure 2.6(b) shows the measured z-scan transmittance with a 40% aperture (S=0.4), that includes the effects of both the nonlinear refraction and saturable absorption. Fig. 2.6(c) shows the normal-

ized results of the division of Fig. 2.6(b) by Fig. 2.6(a), where the effect of saturable absorption is eliminated. In this figure, the peak-valley configuration indicates that the sign of the nonlinear refractive index is negative. The solid line is the theoretical result with the average on-axis phase change $\Delta\Phi_0 = -0.95$, which gives an index change of $\Delta n = -0.96\times10^{-3}$. Assuming the intensity-dependent refractive index of the form $n = n_0 + n_2 I$, we obtain the nonlinear refractive index $n_2 = -1.2 \times 10^{-10}$ cm^2/W, which is four orders of magnitude higher than the known value of $n_2 = 2.8 \times 10^{-14}$ cm^2/W [7] obtained using degenerate four-wave mixing with picosecond pulses. The origin of the nonlinearity is the electronic Kerr effect. We believe that the index change is attributed to the laser-induced thermal effect. In order to confirm this, we measure the dependence of $\Delta T_{P\text{-}V}$ (the difference between the normalized peak and valley transmittance) on the pulse repetition rate. Such an experiment has not yet been reported thus far. In this experiment, we fix the input power at 1.32 mW and change the repetition rate of laser pulses from 0.1 to 1 kHz. The experimental results are shown in Fig. 2.7. A theoretical consideration of the experimental results using a heat conduction equation [8], [9] is given in the Appendix. The calculated values agree well with the experimental ones. This means that the thermally-induced nonlinearity is dominant in

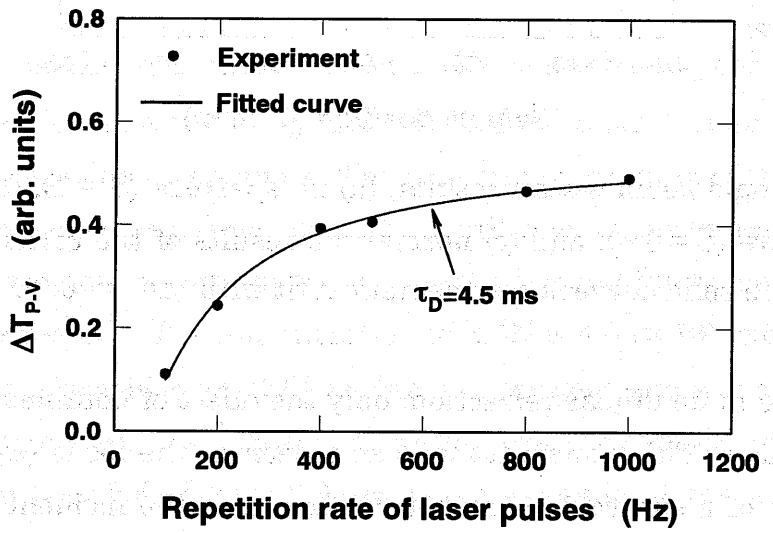

Fig. 2.7. $\Delta T_{P\text{-}V}$ as a function of the pulse repetition rate.

the nonlinearity mechanism of the BDN solution. Moreover, it should be noted that the thermal diffusion time τ_D can be determined by using Eq. (A7): it is 4.5 ms in our case. Using the thermal diffusion time $\tau_D = (\omega_0)^2\rho c_p/4q$ [see Eq. (A3)] and with the known values of ρc_p=1.85 J/Kcm^3, $q=1.5\times10^{-3}$ W/cm [10], we obtain τ_D= 6.8 ms. It approximately agrees with the experimental result determined by the single beam z-scan.

B. Experiment Using the Two-color Z-scan Method

As described in above section, one can measure the thermally-induced nonlinearity using a single beam z-scan, but cannot investigate the rise time of the index change. Similarly to Ref. [9], we here measure the fall time and the rise time of the index change using a two-color z-scan method [3]. Fig. 2.8 shows an experimental setup for the z-scan. The high intensity of a pulsed pump beam induces phase distortion of a CW probe beam that propagates through the medium. The thermally induced index change is determined by the detection of the intensity of the probe field passing through a diaphragm in front of the detector. A Q-switched YLF laser (λ=1.047 μm) is used as the pumping source and a CW He-Ne laser (λ= 0.633 μm) is used as the probe beam. The pump beam is set at vertical polarization by a half-wavelength plate (HWP1) and a polarizer (PR), while the probe beam is set at horizontal

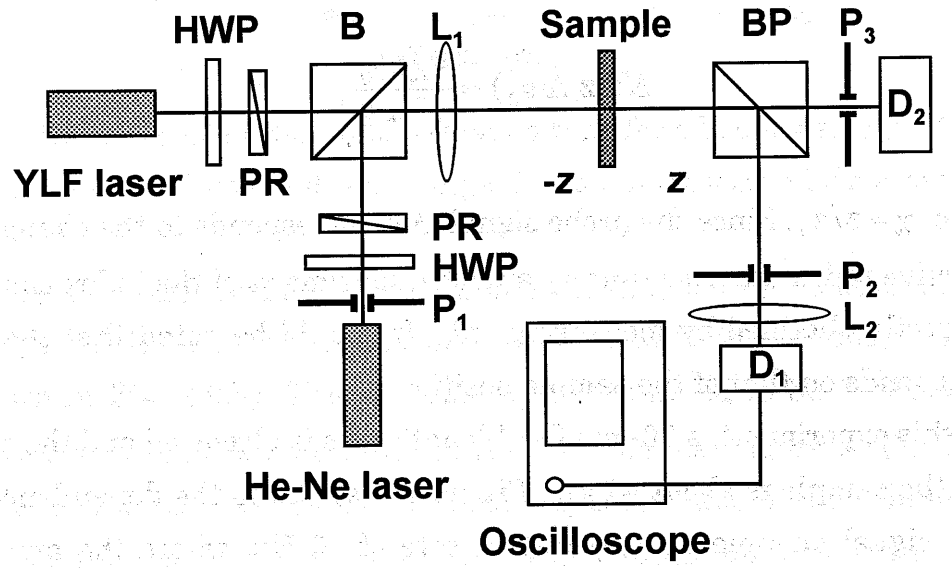

Fig. 2.8. Schematic of a two-color z-scan experimental setup.

polarization. The transmitted probe beam is adjusted by the pinhole P_1 to keep the probe beam size at the focus equal to that of the pump beam. BP is a beam splitter. P_2 and P_3 are diaphragms. D_1 and D_2 are pin photodiodes with a response time of 0.5 ns, and D_2 is used to measure the transmitted pump beam. The variation of the probe signal is detected with D_1 and displayed on a digital oscilloscope. If the power of the probe beam is set to be much lower than the pump power and the absorption coefficient of the BDN solution at 0.633 μm is less than that at 1.047 μm, the thermal effects resulting from the probe beam can be neglected. When the sample is located at position z with respect to the focus, in the limit of a small nonlinear phase shift, the normalized z-scan transmittance T can be written as [2]

$$T(z,\Delta\Phi_0) = \frac{\left|E_a(z,r=0,\Delta\phi_0)\right|^2}{\left|E_a(z,r=0,\Delta\phi_0=0)\right|^2}, \tag{2.4}$$

where E_a is the electrical field at the aperture P_2 plane and $\Delta\phi_0$ is the on-axis phase shift of the electrical field within the sample. The phase shift $\Delta\phi_0$ is related to the on-axis phase shift at the focus $\Delta\Phi_0$ by $\Delta\phi_0 = \Delta\Phi_0/(1+z^2/z_0^2)$, where $z_0 = k(\omega_0)^2/2$ is the diffraction length of the beam. Using the far-field condition, transmittance change can be described as [2]

$$\Delta T(z,\Delta\Phi_0) \approx \frac{4\chi\Delta\phi_0}{\chi^2+9}, \tag{2.5}$$

where $\chi = z/z_0$. Since the probe signal ΔT corresponds to the change in the refractive index, the rise time τ_{th} and the fall time τ_F of the index change can be directly obtained by measuring ΔT. It should be noted that the sign of ΔT depends on that of the sample position.

In this experiment, a 70-mm focal-length lens is also used and the spot size ω_0 at the sample is about 47 μm. Figure 2.9(a) shows the dependence of the probe signal on time at a repetition rate of 16 Hz, where the arrow lines represent the input pumping pulses. As a laser pulse is incident, the probe

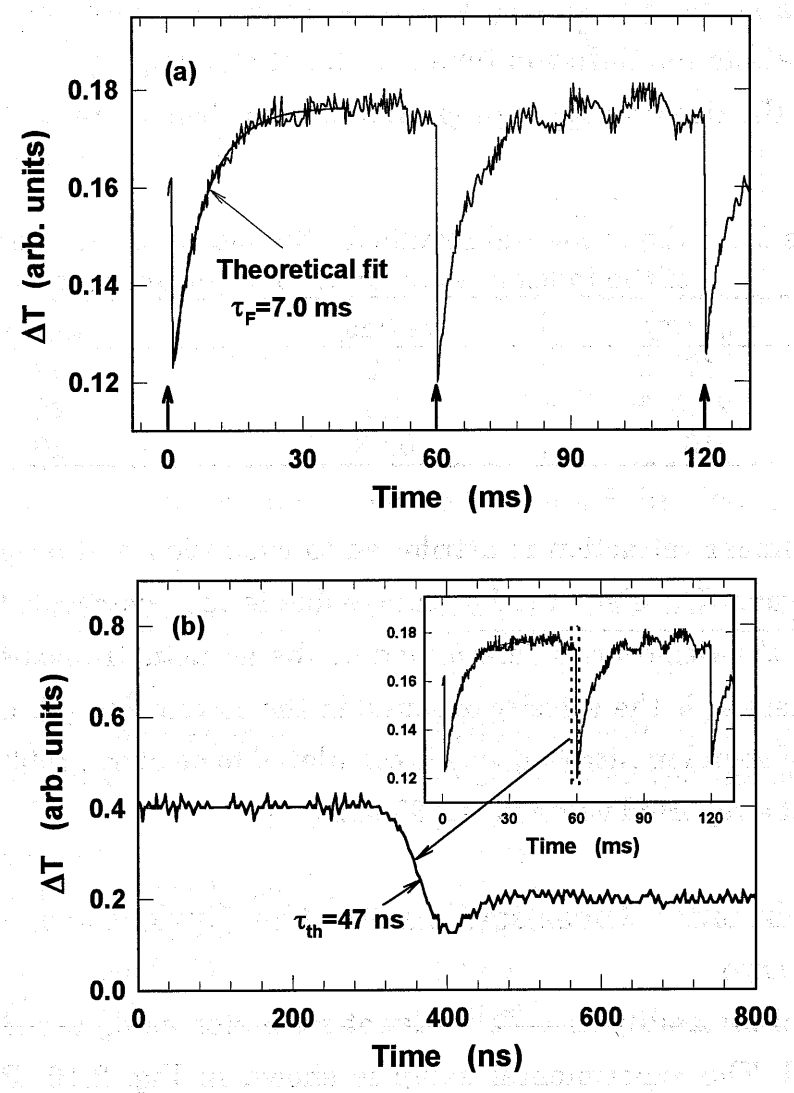

Fig. 2.9. Dependence of the probe signal on time for a beam size $\omega_0 = 47$ μm. (a) In a millisecond time range, (b) In a nanoseccond time range.

signal ΔT is relaxed with a fall time. Using the exponential function (i.e., $1-\exp(-t/\tau_F)$), the fitted curve to the experimental results is obtained, which is also shown in Fig. 2.9(a). The fall time τ_F is estimated to be 7 ms, which agrees well with the thermal diffusion time τ_D= 6.8 ms. Figure 2.9(b) shows the dependence of the variation of the probe signal on time in the nanosecond regime. The relaxing curve is not a simple exponential function and the rise time of index change τ_{th} is about 47 ns. The same experiment was conducted for other beam spot sizes of 16 and 23.5 μm. The obtained experimental

results for the fall time and the rise time of the index change are summarized in Table 2.2. It is confirmed that the fall time is proportional to the square of the beam spot size ω_0 and they agree well with the theoretical values for the thermal diffusion time calculated by using $\tau_D = (\omega_0)^2 \rho c_p / 4q$. It is found that the rise time τ_{th} is proportional to the beam size ω_0. This means

Table 2.2. Experimental results for the fall time and the rise time of the index change for different beam spot sizes ω_0.

ω_0 (μm)	τ_F (ms)	τ_{th} (ns)
47	7.0	47
23.5	1.8	25
16	0.86	16

that the nonlinear refraction is attributed to excitation and propagation of an acoustic wave. The sign of index change due to the photoacoustic effect is negative and the rise time is determined by the acoustic transmit time, i.e., $\tau_{th} \approx \omega_0 / v_A$, where v_A is the velocity of sound in the solvent [2], [9]. In our case, the velocity of sound in nitrobenzene is calculated to be about 1000 m/s and it agrees with the reported value v_A =1463 m/s [11].

2.4 Experimental Investigation for the Optical Bistability in BDN Dye

Here optical bistability in a Fabry-Perot resonator using the BDN dye is demonstrated. The experimental setup is shown in Fig. 2.10. Parameters used in the experiment are listed in Table 2.3. The resonator consists of two multilayer mirrors separated by 200 μm and the BDN concentration is 1.9 mg/ml. The initial phase detuning is a key factor to determine the appearance of optical bistability, which is adjusted by changing the incident angle θ. Typical an experimental result is shown in Fig. 2.11, where the input peak power is 450 W. Figure 2.11 (a) shows the temporal profiles of incident and transmitted pulse in F-P resonator. Figure 2.11(b) shows the input-output characteristics. It is found that a rough hysteresis loop is obtained in the output-input curve.

Finally, it must be discussed whether one can use the dye BDN as a non-

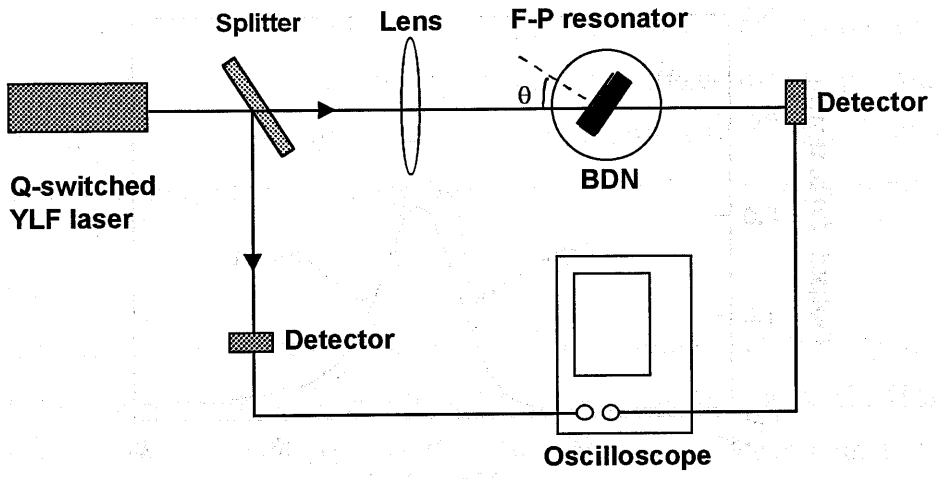

Fig. 2.10. Experimental setup based on bulk Fabry-Perot resonator.

Table 2.3. Parameters used in the experiment for observing bistability.

Medium	BDN in nitrobenzene solvent
Concentration	1.9 mg/ml
Length of the resonator	200 μm (bulk resonator)
Light source	LD pumping Q-switched YLF
Wavelength	1.047 μm
Pulse width	23 ns
Frequency of the laser pulses	1 KHz
Average output power	10 mW
Mirror reflectivity	90%
Focal lens	16 mm

linear material to develop a novel bistable optical device with a response time less than a few nanoseconds. In view of the above theoretical and experimental results, we think that the dye is not suitable for such a device application, since the observed nonlinear refraction is not the population redistribution of the dye molecules but the thermal effects. In fact, we tried to dope the dye into a polymer. However no measurable nonlinear refraction could be obtained using the same z-scan method. We therefore consider that optical bistability observed in our experiment results from strong self-defocusing induced by the photoacoustic effect.

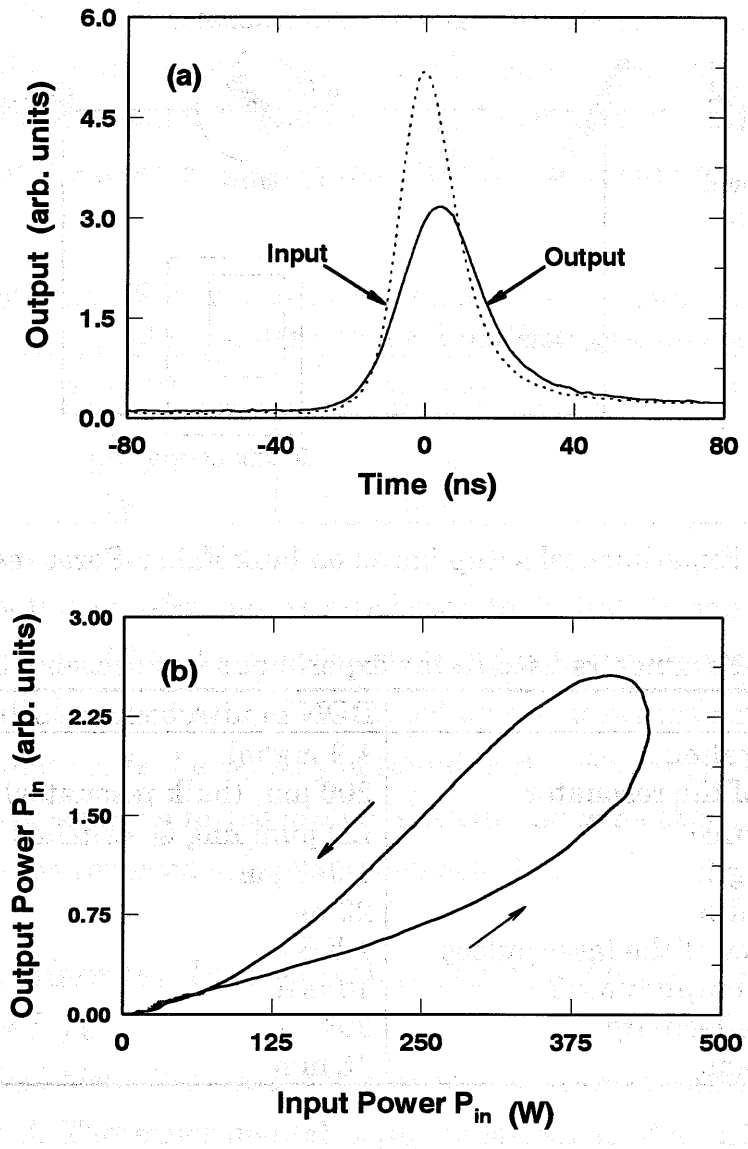

Fig. 2.11. Experimental results for the bulk F-P resonator.
(a) Temporal profiles of input and output pulses.
(b) Input-output characteristics.

2.5 Conclusion

A nonlinear transmission experiment and z-scan experiment are performed to clarify the origin of the nonlinearities of a BDN-nitrobenzene solution in the nanosecond regime. The saturable absorption properties were first determined by using a transmission. The response time of the dye solution is about 1.5 ns. Next, the nonlinear refraction was investigated by using a single beam z-scan and a two-color z-scan. The main origin of the

nonlinear refractive index change is not the population redistribution of the dye molecules but the thermal effect. In particular, the nonlinear refraction in the nanosecond regime is attributed to density change due to propagation of an acoustic wave excited by the laser pulses. The results and discussions presented in this chapter will be applicable for many absorbing materials.

Appendix

For convenience, we assume that the incident pulse duration τ_p is much smaller than the period of laser pulse T_0, as shown in Fig. 2.12. Here the dependence of optical intensity I(t) on time can be regarded as the comb function,

$$I(t) = I_0 \sum_{i=1}^{\infty} \delta(t - iT_0), \tag{A1}$$

where I_0 represents the peak intensity of the incident pulse. Moreover, if we consider only the thermal effect, the temperature distribution can be described by the following heat conduction equation [8], [9]:

$$\rho c_p \frac{\partial \Delta D(r,t)}{\partial t} - q\left[\frac{\partial^2 \Delta D(r,t)}{\partial^2 r} + \frac{1}{r}\frac{\partial \Delta D(r,t)}{\partial r}\right] = \alpha I(r,t), \tag{A2}$$

where ΔD is the change in temperature, α is the absorption coefficient of the

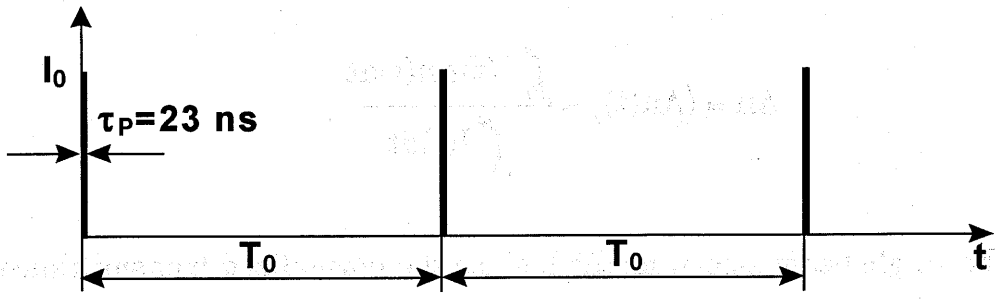

Fig. 2.12. Simple model for the incident pulses.

sample, ρ is the density, c_p is the specific heat, and q is the thermal conductivity. The right hand side of the above equation acts as a heat source. Assuming the Gaussian profile of the pulse and neglecting the second derivative with respect to r in Eq. (A2), we can obtain the following equation:

$$\tau_D \frac{\partial \Delta D(t)}{\partial t} + \Delta D(t) = \frac{\alpha \omega_0^2}{4q} I(t), \tag{A3}$$

where $\tau_D = (\omega_0)^2 \rho c_p / 4q$ is the thermal relaxation time and ω_0 is the radius of the beam waist. The steady-state solution of Eq. (A3) is given by

$$\Delta D(t) = \left(\frac{\alpha \omega_0^2 I_0}{4q\tau_D} \right) \left(\frac{\exp(-(t - iT_0)/\tau_D)}{1 - \exp(T_0/\tau_D)} \right), \tag{A4}$$

$$iT_0 < t < (i+1)T_0,$$

where i is an integer. Since the change in the refractive index $\Delta n(t)$ is proportional to $\Delta D(t)$, we have

$$\Delta n(t) = \frac{\partial n}{\partial D} \left(\frac{\alpha \omega_0^2 I_0}{4q\tau_D} \right) \left(\frac{\exp(-(t - iT_0)/\tau_D)}{1 - \exp(T_0/\tau_D)} \right), \tag{A5}$$

$$iT_0 < t < (i+1)T_0,$$

where $\partial n/\partial D$ is the thermo-optic coefficient. The time-averaged index change is expressed as

$$\Delta n = \langle \Delta n(t) \rangle = \frac{\int_0^\infty I(t) \Delta n(t) dt}{\int_0^\infty I(t) dt}. \tag{A6}$$

In the single beam z-scan method, since the normalized transmittance ΔT_{P-V} is proportional to the change in on-axis refractive index, we can obtain the following equation:

$$\Delta T_{P-V} \propto \frac{I_0 \exp(-\frac{T_0}{\tau_D})}{1-\exp(-\frac{T_0}{\tau_D})} \propto \frac{P_{in}}{f} \frac{\exp(-\frac{1}{f\tau_D})}{1-\exp(-\frac{1}{f\tau_D})}, \quad \text{(A7)}$$

where f is the repetition rate of the incident laser pulses, P_{in} is the input power (in our case, it is set to be a constant). We can determine the thermal relaxation time τ_D by fitting Eq. (A7) to the experimental results in Fig. 2.7.

References

[1] R. L. Sutherland, *Handbook of Nonlinear Optics*, (Marcel Dekker, New York, 1996).

[2] M. Sheik-Bahae, A. A. Said, T. Wei, D. J. Hagan, and E. W. Van Stryland, "Sensitive Measurement of Optical Nonlinearities Using a Single Beam," IEEE. J. Quantum Electron. **26** (1990) 760.

[3] M. Sheik-Bahae, J. Wang, R. DeSalvo, D. J. Hagan, and E. W. Van Stryland, "Measurement of nondegenerate nonlinearities using a two-color Z-scan," Opt. Lett. **17** (1992) 258.

[4] K. H. Drexhage and G. A. Reynolds, "New dye solution for mode-locking Infrared Lasers," Opt. Commun. **10** (1974) 18.

[5] D. Magde, B. A. Bushaw, and M. W. Windsor, "Picosecond flash photolysis and spectroscopy: bis-(4-dimethylaminodithiobenzil)-Ni(II), BDN," Chem. Phys. Lett. **28** (1974) 263.

[6] M. Hercher, "An analysis of aaturable absorbers," Appl. Opt. **6** (1967) 947.

[7] C. Maloney, H. Byrne, W. M. Dennis, and W. Blau, "Picosecond optical phase conjugation using conjugated organic molecules," Chem. Phys. **121** (1988) 21.

[8] S. A. Akhmanov, D. P. Krindach, A. V. Migulin, A. P. Sukhorukov, and R. V.Khokhlov, "Thermal self-actions of laser beams," IEEE J. Quantum Electron. **QE-4** (1968) 568.

[9] P. Brochard, V. G. Mazza, and R. Cabanel, "Thermal nonlinear refraction in dye solutions: a study of the transient regime," J. Opt. Soc. Am. B **14** (1997) 405.

[10] K. Ogusu, Y. Kohtani, and H. Shao, "Laser-induced diffraction rings from an absorbing solution," Opt. Rev. **3** (1996) 232.

[11] R. C. Weast and M. J. Astle, *CRC Handbook of Chemistry and Physics*, (CRC Press, Boca Raton, 1981-1982) p. E-45.

Chapter 3. Optical Bistability in a Nonlinear Fiber Fabry-Perot Resonastor

3.1 Introduction

In this chapter, optical bistability in a nonlinear fiber Fabry-Perot resonator is investigated. Bischofberger and Shen have studied the dynamic behavior of dispersive optical bistability from the quasi-stead-state case to the extremely transient situations using a multiple-beam interference approach [1]. However the iterative method first developed by Ikeda [2] has not yet been reported for the nonlinear Fabry-Perot resonator. Here we present an iterative method for analyzing the transient properties of the nonlinear fiber Fabry-Perot resonator and apply it to linear stability in terms of the input power. We plan to develop a nonlinear fiber Fabry-Perot resonator utilizing the Kerr nonlinearity of the optical fiber as shown in Fig. 3.1(a), and hence these analyses are required to obtain a good guide for the design.

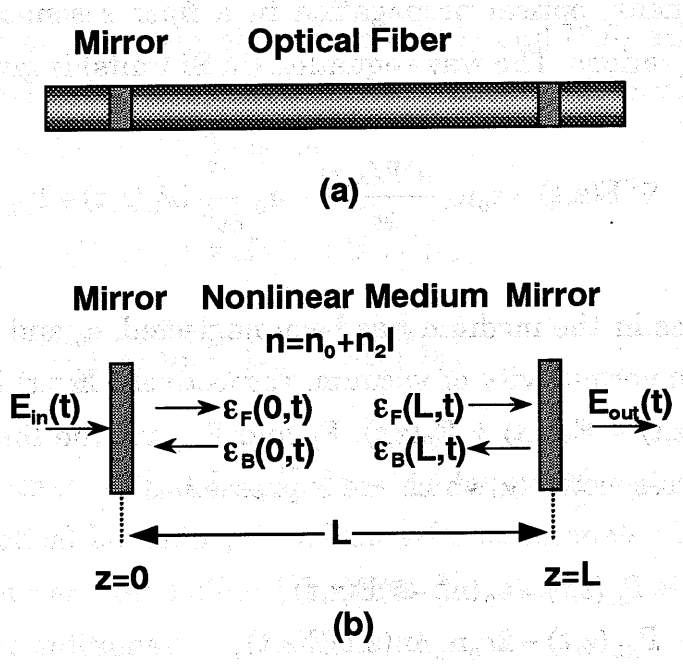

Fig. 3.1. (a) Schematic diagram of a nonlinear fiber Fabry-Perot resonator and (b) its plane-wave model.

3.2 Analysis of Transient Optical Bistability and Stability in a Nonlinear Fiber Fabry-Perot Resonator

3.2.1 Basic Theory

Figure 3.1 shows a schematic diagram of a nonlinear fiber Fabry-Perot resonator and a plane-wave model with the definition of each field for analysis. The forward and backward propagating waves in the cavity can be approximately expressed as plane waves propagating along the z axis by

$$E_F(z,t) = \tfrac{1}{2}\varepsilon_F(z,t)\exp[j(\omega t - n_0 k_0 z)] + \text{c.c.}, \tag{3.1}$$

$$E_B(z,t) = \tfrac{1}{2}\varepsilon_B(z,t)\exp[j(\omega t + n_0 k_0 z)] + \text{c.c.}, \tag{3.2}$$

where ω and k_0 are the angular frequency and wave number in the free-space. ε_F and ε_B are the complex amplitudes of the forward and backward waves, respectively. n_0 is the linear refractive index of the fiber. Like all electromagnetic phenomena, optical propagation in a fiber resonator is governed by Maxwell's equations. The wave equation (in SI units) is given as

$$\nabla^2 E(z,t) = \varepsilon_0\mu_0 \frac{\partial^2 E(z,t)}{\partial t^2} + \mu_0 \frac{\partial^2}{\partial t^2}\{P_L(z,t) + P_{NL}(z,t)\}, \tag{3.3}$$

where the loss in the medium has been neglected. ε_0 and μ_0 are the electric and magnetic permittivity of vacuum, respectively. E(z,t) is the total optical field, i.e., $E(z,t) = E_F(z,t) + E_B(z,t)$. P_L and P_{NL} are the linear and nonlinear polarization, respectively, which are expressed as

$$P_L(z,t) = \varepsilon_0(n_0^2 - 1)E(z,t), \tag{3.4}$$

$$P_{NL}(z,t) = 2\varepsilon_0 n_0 \Delta n(z,t) E(z,t), \tag{3.5}$$

where $\Delta n(t,z)$ is the variation of refractive index arising from the interference of the forward and backward propagating waves in the cavity. For Kerr material, it obeys the Debye relaxation equation [3]

$$\tau\frac{\partial\Delta n}{\partial t}+\Delta n=n_2\left|E(z,t)\right|^2/2, \tag{3.6}$$

where τ and n_2 are the response time and nonlinear refractive index of the Kerr medium, respectively. For a fused-silica fiber, since its response time is very small ($\sim 10^{-15}$ s), it is general assumed that the nonlinearity takes place instantaneously. Substituting Eqs. (3.1)-(3.2) and Eqs. (3.4)-(3.6) into Eq. (3.3), using a slowly varying amplitude approximation, and setting τ =0, the following amplitude equations are obtained,

$$\frac{\partial\varepsilon_F(z,t)}{\partial z}+\frac{n_0}{c}\frac{\partial\varepsilon_F(z,t)}{\partial t}=-jn_2k_0\{\left|\varepsilon_F(z,t)\right|^2+2\left|\varepsilon_B(z,t)\right|^2\}\varepsilon_F(z,t), \tag{3.7}$$

$$-\frac{\partial\varepsilon_B(z,t)}{\partial z}+\frac{n_0}{c}\frac{\partial\varepsilon_B(z,t)}{\partial t}=-jn_2k_0\{\left|\varepsilon_B(z,t)\right|^2+2\left|\varepsilon_F(z,t)\right|^2\}\varepsilon_B(z,t). \tag{3.8}$$

The factor of two on the right side of Eqs. (3.7) and (3.8) arises from the standing-wave effect (i.e., the so-called cross-phase modulation). In case of steady-state, Eqs. (3.7) and (3.8) become

$$\frac{\partial\varepsilon_F}{\partial z}=-jn_2k_0\{\left|\varepsilon_F\right|^2+2\left|\varepsilon_B\right|^2\}\varepsilon_F, \tag{3.9}$$

$$-\frac{\partial\varepsilon_B}{\partial z}=-jn_2k_0\{\left|\varepsilon_B\right|^2+2\left|\varepsilon_F\right|^2\}\varepsilon_B. \tag{3.10}$$

It is easy to show that $|\varepsilon_B|^2$ and $|\varepsilon_F|^2$ do not change with z. Analysis for the steady-state of optical bistability in a Fabry-Perot resonator has been performed by Marburger and Felber [3] using the above equations and the related boundary conditions.

3.2.2 Transient Analysis Based on Iterative Method

A. Formulation

In Fig. 3.1, the resonator consists of a nonlinear medium of thickness L and two identical mirrors of reflectivity R. For Kerr medium, the nonlinear

refractive index is given by

$$n = n_0 + n_2|E|^2 = n_0 + \frac{2\eta_0 n_2}{n_0} I = n_0 + \frac{2\eta_0 n_2}{n_0}\frac{P}{S_{eff}}, \tag{3.11}$$

where η_0 is the wave impedance in the vacuum, I, P, and E are the optical intensity, optical power, and optical electric field, respectively. S_{eff} is the effective mode area of the fiber. First, we derive the transmitted wave $E_{out}(t)$ when an optical pulse with slowly time-varying electric field $E_{in}(t)$ is incident on the nonlinear resonator. The boundary conditions for the input mirror at z=0 and the output mirror at z=L may be expressed as

$$\varepsilon_F(0,t) = (1+r)E_{in}(t) - r\varepsilon_B(0,t), \tag{3.12}$$

$$E_{out}(t) = (1-r)\varepsilon_F(L,t), \tag{3.13}$$

$$\varepsilon_B(L,t) = -r\varepsilon_F(L,t), \tag{3.14}$$

where $r(=\sqrt{R})$ is the amplitude reflectivity of the mirrors. In the limit of instantaneous relaxation of the nonlinearity, the forward wave at z = L is related to that at z=0 as follows:

$$\varepsilon_F(L,t) = \varepsilon_F(0, t-\tau_R)\exp[-j(\phi_0 + \phi_{NF}(t-\tau_R))], \tag{3.15}$$

where $\tau_R(=n_0L/c)$ is the cavity transit (half-round-trip) time. $\phi_0(=n_0k_0L)$ is the linear phase shift and $\phi_{NF}(t-\tau_R)$ is the nonlinear phase shift given by

$$\phi_{NF}(t-\tau_R) = (n_2k_0)\int_0^L \left(|\varepsilon_F(z, t-\tau_R + n_0z/c)|^2 + 2|\varepsilon_B(z, t-\tau_R + n_0z/c)|^2 \right) dz. \tag{3.16}$$

Note that, in Eq. (3.16), the contribution of the backward intensity to the phase shift is double that of the forward intensity due to the cross-phase modulation. Since the integration of the backward intensity cannot be carried out exactly, we approximate Eq. (3.16) by applying adequate numerical integration formulas:

$$\phi_{NF}(t-\tau_R) \cong n_2 k_0 (L|\varepsilon_F(0,t-\tau_R)|^2 + 2L\frac{|\varepsilon_B(0,t-\tau_R)| + |\varepsilon_B(d,t)|}{2}), \quad (3.17a)$$

$$= n_2 k_0 L(|\varepsilon_F(L,t)|^2 + |\varepsilon_B(L,t-2\tau_R)|^2 + |\varepsilon_B(L,t)|^2),$$

$$\cong n_2 k_0 L(|\varepsilon_F(0,t-\tau_R)|^2 + 2|\varepsilon_B(L,t-\tau_R)|^2). \quad (3.17b)$$

Equation (3.17a) is the approximation due to a trapezoid rule. Here we use relations, $|\varepsilon_B(0,t-\tau_R)|^2=|\varepsilon_B(L,t-2\tau_R)|^2$ and $|\varepsilon_F(0,t-\tau_R)|^2=|\varepsilon_F(L,t)|^2$, which hold because of no loss. On the other hand, Eq. (3.17b) is the approximation due to a midpoint rule. Similarly, the backward wave at z=0 is related to that at z=L as follows:

$$\varepsilon_B(0,t) = \varepsilon_B(L,t-\tau_R)\exp[-j(\phi_0 + \phi_{NB}(t-\tau_R))], \quad (3.18)$$

where the nonlinear phase shift $\phi_{NB}(t-\tau_R)$ is given by

$$\phi_{NB}(t-\tau_R) = n_2 k_0 \int_0^L \{ 2|\varepsilon_F(L-z,t-\tau_R + n_1 z/c)|^2 + |\varepsilon_B(L-z,t-\tau_R + n_1 z/c)|^2 \}\, dz,$$

$$\cong n_2 k_0 L(|\varepsilon_B(L,t-\tau_R)|^2 + |\varepsilon_F(L,t-\tau_R)|^2 + |\varepsilon_F(0,t)|^2), \quad (3.19a)$$

$$\cong n_2 k_0 d(|\varepsilon_B(L,t-\tau_R)|^2 + 2|\varepsilon_F(0,t-\tau_R)|^2). \quad (3.19b)$$

Equation (3.19a) is the trapezoid approximation. Equation (3.19b) is the midpoint approximation and $|\varepsilon_F(L,t-\tau_R)|^2=|\varepsilon_F(0,t-2\tau_R)|^2$ is used. Substituting Eq. (3.15) into Eq. (3.13), we obtain the transmitted field

$$E_{out}(t) = (1-r)\varepsilon_F(0,t-\tau_R)\exp[-j(\phi_0 + \phi_{NF}(t-\tau_R))]. \quad (3.20)$$

Here, using Eqs. (3.12)-(3.14) and (3.18), the field $\varepsilon_F(0,t-\tau_R)$ can be expressed as

$$\varepsilon_F(0,t-\tau_R) = (1+r)E_{in}(t-\tau_R) + \frac{R}{1-r}E_{out}(t-2\tau_R) \quad (3.21)$$
$$\times \exp[-j(\phi_0 + \phi_{NB}(t-2\tau_R))].$$

Further, substituting Eq. (3.21) into Eq. (3.20), we obtain the final expression for the transmitted field

$$E_{out}(t) = TE_{in}(t-\tau_R)\exp[-j(\phi_0 + \phi_{NF}(t-\tau_R))] + RE_{out}(t-2\tau_R)\exp[-j(2\phi_0 + \phi_{NF}(t-\tau_R) + \phi_{NB}(t-2\tau_R))], \quad (3.22)$$

where T(=1-R) is the transmissivity of the mirrors. In our case, we may regard the values of $E_{in}(t-\tau_R)$ and $E_{out}(t-2\tau_R)$ as known. The problem is the calculation of nonlinear phase shifts $\phi_{NF}(t-\tau_R)$ and $\phi_{NB}(t-2\tau_R)$. It should be noted that the forward and backward intensities at the output mirror (z=L) can be related to the output intensities in terms of the transmissivity $T=|E_{out}(t)|^2/(n_0|\varepsilon_F(L,t)|^2)$.

Under the trapezoid approximation, the two nonlinear phase shifts are given by

$$\phi_{NF}(t-\tau_R) = A\left((1+R)|E_{out}(t)|^2 + R|E_{out}(t-2\tau_R)|^2\right), \quad (3.23)$$

$$\phi_{NB}(t-2\tau_R) = A\left((1+R)|E_{out}(t-2\tau_R)|^2 + |E_{out}(t)|^2\right), \quad (3.24)$$

where $A = n_2 k_0 L/n_0 T$. Substitution of Eqs. (3.23) and (3.24) into Eq. (3.22) gives the final difference equation describing the dynamics of the nonlinear resonator. Since the equation is an implicit formula for the transmitted field $E_{out}(t)$, i.e., $E_{out}(t)$ to be determined is a function of itself, a self-consistent solution for the transmitted field on the computer must be determined.

Under the midpoint approximation, on the other hand, the two nonlinear phase shifts are given by

$$\phi_{NF}(t-\tau_R) = A\left(n_0 T|\varepsilon_F(0,t-\tau_R)|^2 + 2R|E_{out}(t-\tau_R)|^2\right), \quad (3.25)$$

$$\phi_{NB}(t-2\tau_R) = A\left(R|E_{out}(t-2\tau_R)|^2 + 2|E_{out}(t-\tau_R)|^2\right), \quad (3.26)$$

where we can calculate $|\varepsilon_F(0,t-\tau_R)|^2$ in Eq. (3.25) from Eqs. (3.21) and (3.26). Substitution of these equations into Eq. (3.22) gives the final difference equation. The equation is explicit, in contrast to the case of trapezoid approximation.

B. Linear Stability Analysis

Setting $E_{in}(t) = E_{in}$ and $E_{out}(t) = E_{out}(t - 2\tau_R) = E_t$ in Eq. (3.22), we have the following equation for the steady-state solution E_t:

$$E_t = TE_{in}\exp\left\{-j\left(\phi_0 + A(1+2R)|E_t|^2\right)\right\} + RE_t\exp\left\{-j\left(2\phi_0 + 3A(1+R)|E_t|^2\right)\right\} \quad (3.27)$$

From the above equation, we have the transmissivity as

$$\frac{|E_t|^2}{|E_{in}|^2} = \frac{1}{1 + F\cdot\sin^2\left(\phi_o + \frac{3A(1+R)}{2}|E_t|^2\right)}, \quad (3.28)$$

where $F(= 4R/(1-R)^2)$ is the finesse of the cavity. Since the right-hand side of Eq. (3.28) is a function of $|E_t|^2$, the input-output characteristics can be determined by computing the input intensity $|E_{in}|^2$ for a given output intensity $|E_t|^2$. In the linear case, A=0 and resonance takes place when $\phi_0 = k_0 n_0 L = M\pi$ (where M is an integer). We hereafter define the initial detuning of the cavity as $\Delta\phi_0 = 2(\phi_0 - M\pi)$.

According to Refs. [4] and [5], we add a slight perturbation $\varepsilon(t)$ to the steady-state solution E_{out} in one round-trip time as

$$E_{out}(t) = E_t + \varepsilon(t), \quad |\varepsilon| \le E_{out}, \quad (3.29)$$

with

$$\varepsilon(t) = \delta\exp(j\sigma t) + \mu\exp(-j\sigma t). \quad (3.30)$$

Substituting Eq. (3.29) into Eq. (3.22) with Eqs. (3.23) and (3.24), we have the following difference equation for perturbation:

$$\begin{aligned} E_{out}(t + 2\tau_R) &= E_t + \varepsilon(t + 2\tau_R) \\ &= E_t + \delta\exp(j\sigma t)\exp(j2\sigma\tau_R) + \mu\exp(-j\sigma t)\exp(-j2\sigma\tau_R). \end{aligned} \quad (3.31)$$

Since the perturbation from the steady-state is assumed in a period of round-trip, Eq.(3.31) becomes

$$
\begin{aligned}
E_{out}(t+2\tau_R) = (1-R)E_{in}\exp\Big\{-j\big(\phi_0 + A(1+R)(E_t+\varepsilon(t+2\tau_R))(E_t^*+\varepsilon(t+2\tau_R)^*\big)+ \\
A*R(E_t+\varepsilon(t))(E_t^*+\varepsilon(t)^*)\Big)\Big\}+R*(E_t+\varepsilon(t))\times \\
\exp\Big\{-j\big(2\phi_0 + A(2+R)(E_t+\varepsilon(t+2\tau_R))(E_t^*+\varepsilon(t+2\tau_R)^*\big) \\
+A(1+2R)(E_t+\varepsilon(t))(E_t^*+\varepsilon(t)^*)\Big)\Big\},
\end{aligned}
\tag{3.32}
$$

after some algebra, including a series expansion and neglecting the terms which include the powers of $\varepsilon(t)$ and $\varepsilon(t+2\tau_R)$ greater than 1, we can obtain the following equation:

$$
\begin{aligned}
&\varepsilon(t+2\tau_R) = -jUA\Big((1+R)\big(E_t\varepsilon^*(t+2\tau_R)+E_t^*\varepsilon(t+2\tau_R)\big)+R\big(E_t\varepsilon^*(t)+E_t^*\varepsilon(t)\big)\Big) \\
&-jVE_tA\Big((2+R)\big(E_t\varepsilon^*(t+2\tau_R)+E_t^*\varepsilon(t+2\tau_R)\big)+(1+2R)\big(E_t\varepsilon^*(t)+E_t^*\varepsilon(t)\big)\Big) \\
&+V\varepsilon(t),
\end{aligned}
\tag{3.33}
$$

where

$$U = (1-R)E_{in}\exp\Big(-j\big(\phi_0 + A(1+2R)|E_t|^2\big)\Big), \tag{3.34}$$

$$V = R*\exp\Big(-j\big(2\phi_0 + 3A(1+R)|E_t|^2\big)\Big). \tag{3.35}$$

On the other hand, the perturbation $\varepsilon(t+2\tau_R)$ is given by

$$\varepsilon(t+2\tau_R) = \delta\exp(j\sigma t)\exp(j2\sigma\tau_R) + \mu\exp(-j\sigma t)\exp(-j2\sigma\tau_R). \tag{3.36}$$

Substituting Eq. (3.26) into Eq. (3.23) and further expressing Eq. (3.23) in matrix form, we have the following eigenvalue problem:

$$
\begin{bmatrix} B_1\exp(j2\sigma\tau_R)+B_2-\lambda & C_1\exp(j2\sigma\tau_R)+C_2 \\ C_1^*\exp(j2\sigma\tau_R)+C_2^* & B_1^*\exp(j2\sigma\tau_R)+B_2^* \end{bmatrix}\begin{bmatrix}\delta \\ \mu^*\end{bmatrix} = 0, \tag{3.37}
$$

with

$$B_1 = -jUA(1+R)E_t^* - jVA(2+R)|E_t|^2 - 1, \tag{3.38}$$

$$B_2 = -jUARE_t^* - jVA(1+2R)|E_t|^2 + V, \tag{3.39}$$

$$C_1 = -jUA(1+R)E_t - jVA(2+R)E_t^2, \tag{3.40}$$

$$C_2 = -jUARE_t - jVA(1+2R)E_t^2, \tag{3.41}$$

where $\lambda = \exp(j2\sigma\tau_R)$ is an eigenvalue to be determined. Note that Eq. (3.37) is a pseudo-eigenvalue problem since the element of the matrix contains the eigenvalue λ. Setting the determinant of the coefficient matrix equal to zero, we have the following characteristic equation:

$$\lambda^2\left(|B_1 - 1|^2 - |C_1|^2\right) + 2\lambda \mathrm{Re}\left((B_1 - 1)B_2^* - C_1C_2^*\right) + \left(|B_2|^2 - |C_2|^2\right) = 0. \qquad (3.42)$$

The steady-state solution E_{out} is stable only when the absolute value of λ is less than unity.

C. Numerical Results and Discussion

In this section, we present the numerical results for the dynamic properties of a nonlinear Fabry-Perot resonator made of fused optical fiber and two reflection mirrors. All numerical results presented here are calculated for the fiber parameters shown in Table 3.1 in correspondence with the practical

Table 3.1. The related parameters used in the theoretical calculation.

Medium	Single-mode fiber
Linear refractive index n_0	1.454
Nonlinear refractive index n_2	1×10^{-22} m^2/V^2
Effective mode area S_{eff}	50 μm^2
Fiber loss α	0
Wavelength λ.	1.06 μm

conditions. As an incident pulse, we take the following Gaussian temporal pulse of

$$E_{in}(t) = E_0 \exp\left[-\ln\sqrt{2}\left(\frac{t}{\tau_P/2}\right)^2\right], \qquad (3.43)$$

where τ_P is the pulse width defined by full width at half-maximum of the power.

First, we present the numerical results calculated by the iterative method based on the two approximations and compare them with those determined by the multiple-beam method. Figure 3.2 shows the typical numerical results

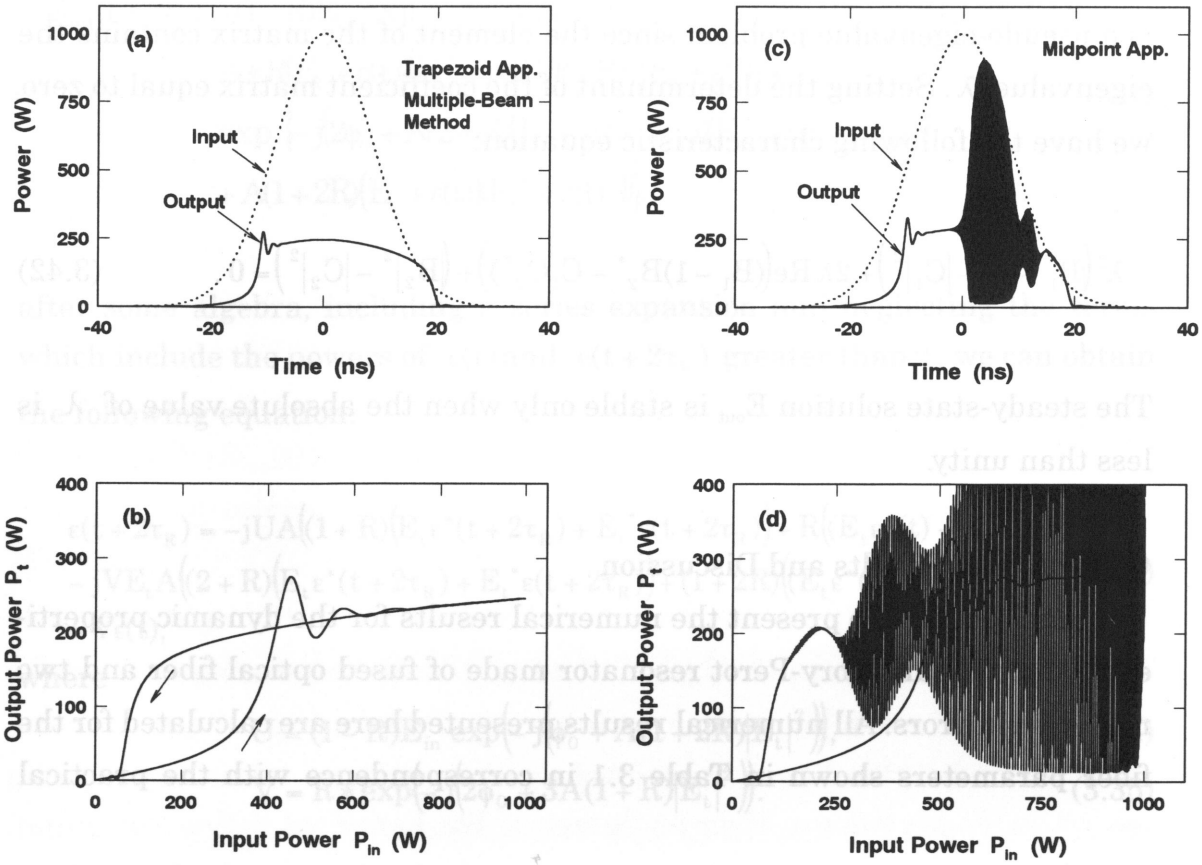

Fig. 3.2. Nonlinear pulse response and input-output characteristics of the fiber Fabry-Perot resonator with τ_p = 20 ns, L = 1 cm, R = 0.9, and $\Delta\phi_0$=-0.1π. The results are calculated by three methods: (a) iterative method using the trapezoid rule and multiple-beam method (note that the two results are indistinguishable), (b) iterative method using the midpoint rule.

for the temporal change of the output pulse and the corresponding input-output characteristics when an optical pulse of 20-ns pulse width and 1-kW peak power is incident on the fiber resonator with L=1 cm, R=0.9 and $\Delta\phi_0 = -0.1\pi$. The numerical results calculated by the iterative method using the trapezoid rule agree with those given by the multiple-beam method to three significant figures. Therefore, those results are indistinguishable when plotted, as true for the case of the nonlinear ring resonator. We can see, however, that instability takes place at the high-transmission level in the midpoint approximation (shown in Figs. 3.2 (c) and 3.2(d)); moreover, there is a large discrepancy between the magnitudes of the output power calculated

with the two approximations. The present phenomenon is not the inherent instability of the nonlinear resonator but numerical instability in the computation procedure.

Next, we present the numerical results of linear stability analysis. Figure 3.3 shows a typical example of the stationary input-output characteristics and unstable regions. Unstable regions exist in the positive-slope branch as well as in the negative-slope branch. The negative-branch instability leads to optical bistability and the positive-branch instability is called Ikeda instability. We here focus on the positive-branch unstable regions marked by A and B and define threshold power P^{I}_{UL}, P^{I}_{UH}(where I=A, B) for Ikeda instability. We also define switch-on and switch-off powers, P_{SH}, P_{SL}, respectively. Figure 3.4 shows the dependence of Ikeda instability threshold and bistability switching powers on the initial detuning $\Delta\phi_0$ for the mirror reflectivity R=0.9 and 0.8 and a resonator length of L=10 cm. Note that the results in Fig. 3.4 are useful for other lengths of the resonator since these threshold and switching powers are inversely proportional to the resonator length. The switch-on power P_{SH} increase with initial detuning $|\Delta\phi_0|$. As the initial detuning $|\Delta\phi_0|$ decreases, the width of the hysteresis loop, $P_{SH}-P_{SL}$, decreases and vanishes at a critical point $\Delta\phi_0 = -\Delta\phi_d$ (in this case, $\Delta\phi_d = 0.10\pi$

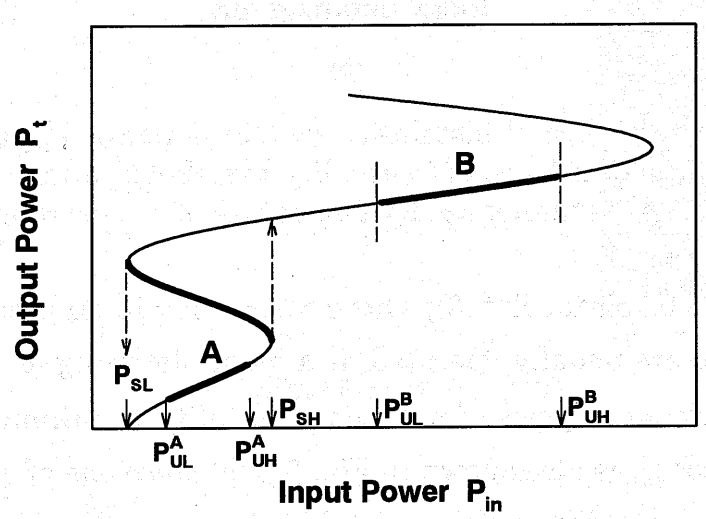

Fig. 3.3. Typical curve of steady-state optical bistability and unstable region.

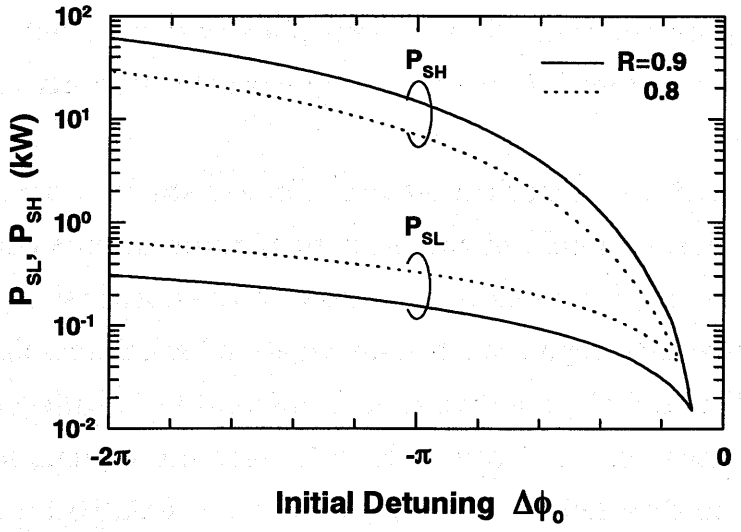

(a)

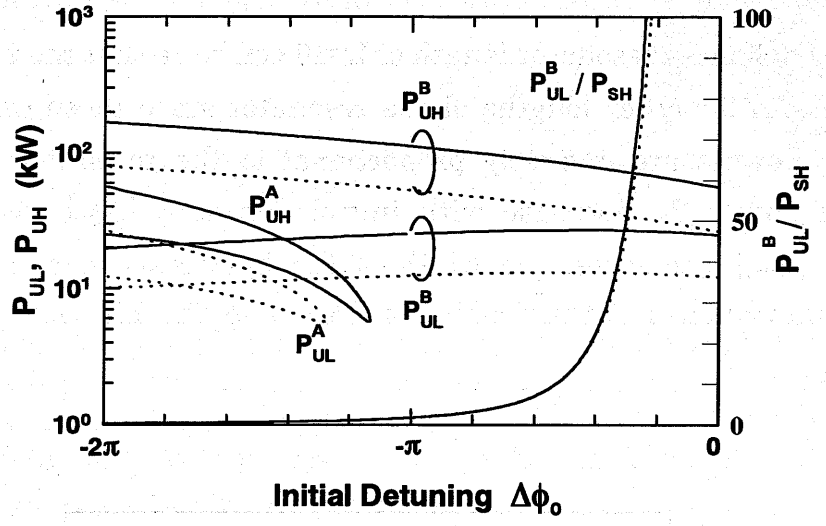

(b)

Fig. 3.4. (a) Dependence of bistability switching power P_{SH} and P_{SL} on $\Delta\phi_0$ and (b) dependence of instability threshold power P_{UL} and P_{UH} on the initial detuning $\Delta\phi_0$ for two values of mirror reflectivity R.

for R=0.9, $\Delta\phi_d = 0.15\pi$ for R=0.8), where we can obtain differential gain. The bistable devices are usually operated at a small detuning of $\pi < \Delta\phi_0 < \Delta\phi_d$. The ratio of minimum power for Ikeda instability to minimum power for bistability, P^B_{UL}/P_{SH}, is also shown in Fig. 3.4 (b) since one of our interests is whether Ikeda instability affects bistable device application or not. The power ratio P^B_{UL}/P_{SH}, is found to increase with decreasing detuning and to

exceed 100 near the differential gain region. The instability threshold power P^{B}_{UL} also becomes less than P^{A}_{UL} in the low-transmission state for $\Delta\phi_0 < -\pi$. However, it should be noted that, since $P^{A}_{UL} < P_{SH}$ in such a region, the output is unstable in the low-transmission state before being switched to the high-transmission state. We therefore conclude that Ikeda instability hardly affects bistable device application since bistable devices are always operated at near resonance. It is interesting to compare the results for the instability threshold with those given by Firth in Ref. [4], a stability map defined by the intracavity intensity and initial detuning is shown for a special case of zero transmission. Although it generally agrees with that in Fig. 3.4, we can see a few disagreements. The instability threshold P^{B}_{UL} in the high-transmission state does not increase with detuning $|\Delta\phi_0|$; moreover all the instability threshold powers P^{I}_{UL}, P^{I}_{UH} decrease with decrease in mirror reflectivity. Next, we show an example of the numerical results where instability takes place in addition to optical bistability. Figure 3.5 shows the input-output characteristics of the fiber resonator when an input pulse with 10-μs pulse duration and 40-kW peak power is incident in the resonator with L = 10 cm, $\Delta\phi_0 = -0.4\pi$, and R= 0.9. It is found that Ikeda instability occurs when the

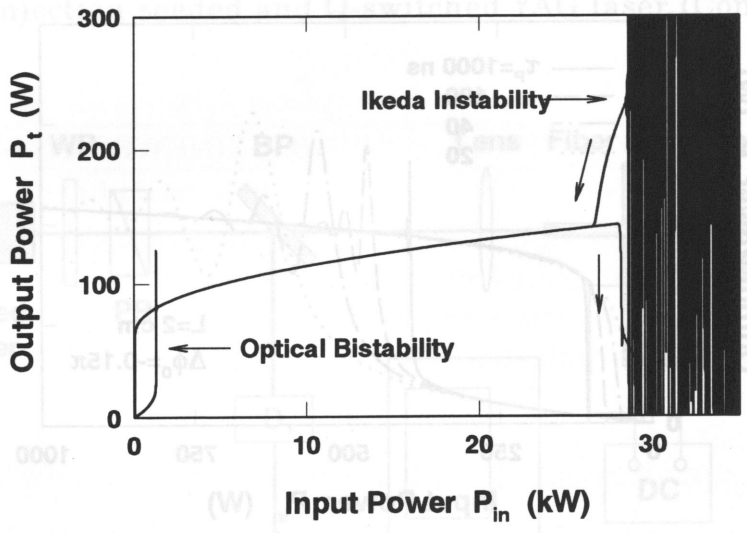

Fig. 3.5. Input-output characteristics of the fiber Fabry-Perot resonator with L=10 cm, $\Delta\phi_0 = -0.4\pi$, $\tau_P = 10$ μs, and R = 0.9, where both optical bistability and Ikeda instability occurs.

incident power P_{in}=28.0 kW, according to the linear stability analysis shown in Fig. 3.4, the threshold power for Ikeda instability is P_{UL}^{B}=26.9 kW, it approximately agrees with the transient results.

Finally, we present the numerical results for transient optical bistability calculated from the iterative method based on the trapezoid rule. Figure 3.6 shows the input-output characteristics of the fiber resonator with L = 2 cm, $\Delta\phi_0 = -0.15\pi$, and R= 0.9 for several values of the input pulse duration τ_P. As the pulse width is increased, the width of the hysteresis loop decreases and approaches one of steady-state solution. An overshoot and undershoot in the transient analysis exist, however, even if the pulse width reaches infinity. In the quasi-steady state, the switching speed of the bistable device is governed by the cavity decay time $t_C = 2n_1L/(1-R^2)c$. In present case, $t_C \approx 1.0$ ns. We can have the quasi-steady-state for $\tau_P > 500t_C - 1000t_C$. Figure 3.7 shows transient optical bistability in the fiber resonator with L = 2 cm and R = 0.9 for several values of initial detuning $|\Delta\phi_0|$. The width of hysteresis loop and switching power increase with increasing detuning $|\Delta\phi_0|$ as predicted by the steady-state analysis. It is also found that as the detuning is increased, the shape of the hysteresis loop sharpens.

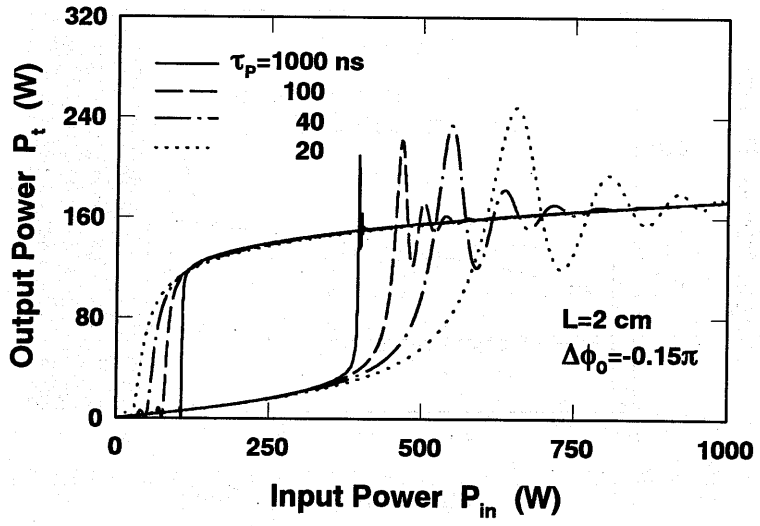

Fig. 3.6. Transient optical bistability in the fiber Fabry-Perot resonator with L = 2 cm, $\Delta\phi_0$= -0.15π, and R = 0.9 for several valuse of initial input pulse duration τ_p.

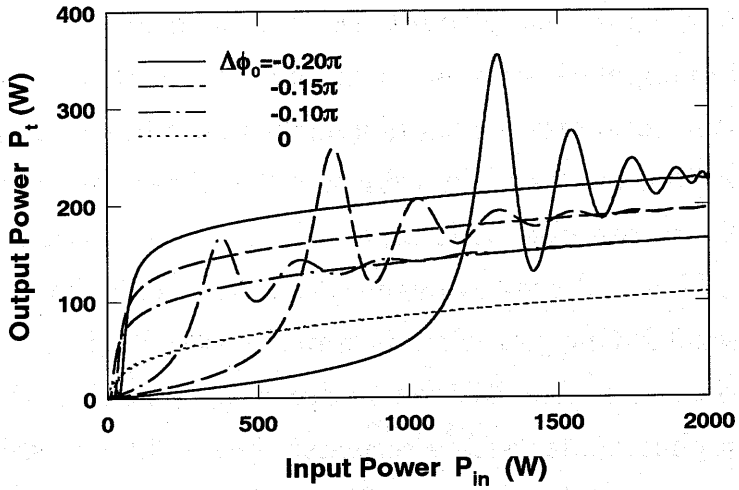

Fig. 3.7. Transient optical bistability in the fiber Fabry-Perot resonator with L = 2 cm and R = 0.9 for several values of initial detuning $\Delta\phi_0$. The pulse width of the input pulse is τ_p = 20 ns.

3.3 Experiment on a Nonlinear Fiber Fabry-Perot Resonator

In this section, we try to demonstrate optical bistability in a nonlinear fiber Fabry-Perot resonator. The experimental setup is shown in Fig. 3.8, where an injection-seeded and Q-switched YAG laser (Continuum HPO-

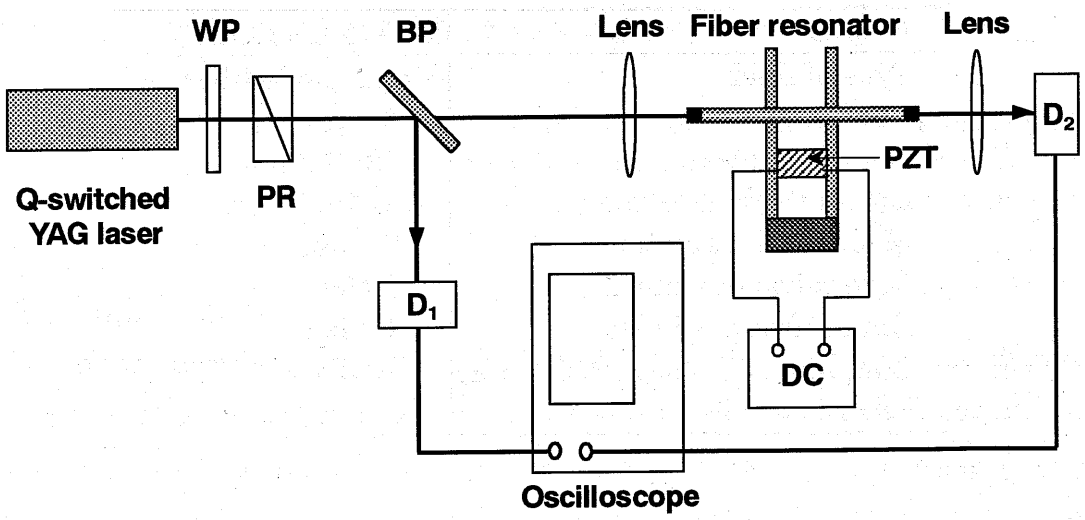

Fig. 3.8. Experimental setup for a fiber Fabry-Perot resonator.

1000) operating at 1.06 μm is used as the pump source. A half-wave plate (WP) and a polarizer (PR) are used as an attenuator to adjust the input power. The pump light is coupled into the fiber by a 10× microscope objective. A single-mode nonpolarization-maintaining fiber with a length of 5 cm is used to form the resonator, which is mounted on a brass block. All parameters about the fiber are listed in Table 3.2. The fiber ends are carefully polished normally to the fiber axis and multilayer dielectric mirrors are deposited on the fiber endfaces by evaporation. The reflectivity of the mirrors are larger than 0.9. One piezoelectric transducer (PZT) is used to control the cavity phase detuning. The PZT can be driven by a stabilizing DC source. D_1 and D_2 are pin photodiodes with a response time of 0.5 ns, which are used to measure the temporal intensity profiles of input and transmitted pulses, respectively. Figure 3.9 shows the input-output characteristics of the fiber resonator when an input pulse with 30-ns pulse duration and 1.5-kW peak power is incident in the resonator. However, contrary to the theoretical results shown in above section, we cannot observe any hysteresis whenever the initial detuning is changed. Under the detail measurement, we found that there exist a stimulated Brillouin scattering in the fiber resonator, which will decrease the resonator finesse considerably. We will describe and discuss it in Chaps. 5 and 6.

Table 3.2. Parameters for a typical single-mode fiber.

NAME	F-SY(NEWPORT)
Type of fiber	Single-mode fiber
Core diameter	6 μm
Clad diameter	125±2 μm
Clad outside diameter	245±15 μm
Mode field diameter	7.7 μm
Core refractive index	1.4541
Clad refractive index	1.4496
Coupling efficiency (Exp. data)	10 dB
Fiber loss	1.6 dB/km

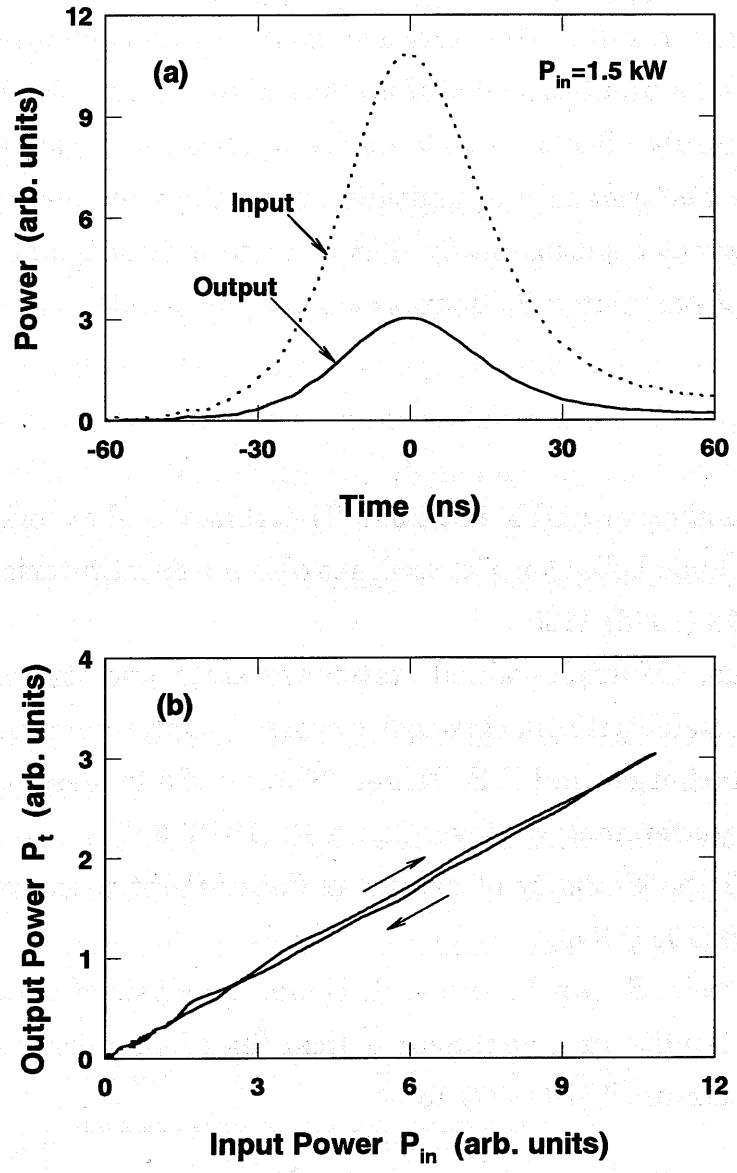

Fig. 3.9. (a) Experimental results for the temporal incident and output pulses in a fiber Fabry-Perot resonator with L = 5 cm, R = 0.9, and τ_P = 30 ns, (b) input-output characteristics of the resonator.

3.4 Conclusion

We have described two iterative methods for calculating the dynamic properties of the plane Fabry-Perot resonator filled with a nonlinear medium which has an instantaneous response time when an optical pulse with an arbitrary temporal profile is incident on it. Further, we performed a linear stability analysis to examine whether Ikeda instability affects bistable device application or not. Comparison with the multiple-beam method showed

that the iterative method based on the trapezoid rule is much simpler and gives accurate results. The iterative method based on the midpoint rule however is not suitable because of numerical instability. We found that Ikeda instability hardly affects bistable device application because the instability threshold is two orders of magnitude larger than the switching power. Finally, we cannot experimentally demonstrate optical bistability due to the occurrence of stimulated Brillouin scattering in the fiber resonator.

References

[1] T. Bischofberger and Y. R. Shen, "Theoretical and experimental study of the dynamic behavior of a nonlinear Fabry-Perot interferometer," Phys. Rev. A 19 (1978) 1169.

[2] K. Ikeda, "Multiple-valued stationary state and its instability of the transmitted light by a ring cavity system," Opt. Commun. 30 (1979) 257.

[3] J. H. Marburger and F. S. Felber, "Theory of a lossless nonlinear Fabry-Perot interferometer," Phys. Rev. A 17 (1978) 335.

[4] W. J. Firth, "Stability of nonlinear Fabry-Perot resonators," Opt. Commun. 39 (1981) 343.

[5] A. L. Steele, S. Lynch, and J. E. Hoad, "Analysis of optical instabilities and bistability in a nonlinear optical fiber loop mirror with feedback," Opt. Commun. 137 (1997) 136.

Chapter 4. Optical Bistability in a Nonlinear Fiber Ring Resonator

4.1 Introduction

In this chapter, a fiber ring resonator with a double fiber coupler is considered, where two outputs are available. We develop a transient analysis for this kind of resonator using an iterative method and examine the instability. The numerical results for both transmission bistability and reflective bistability will be presented. Although a linear stability analysis requires a simple and exact equation describing the dynamics of the resonator and a steady-state analysis, such analyses have not yet carried out. The great interest here is whether Ikeda instability affects bistable device application or not.

4.2 Analysis of Transient Optical Bistability and Stability

A. Transient Analysis

Figure 4.1 shows a schematic diagram of a nonlinear fiber ring resonator, which consists of a fiber ring of length L and two identical fiber couplers. In this case, there are two output ports, i.e., transmission and reflection ports

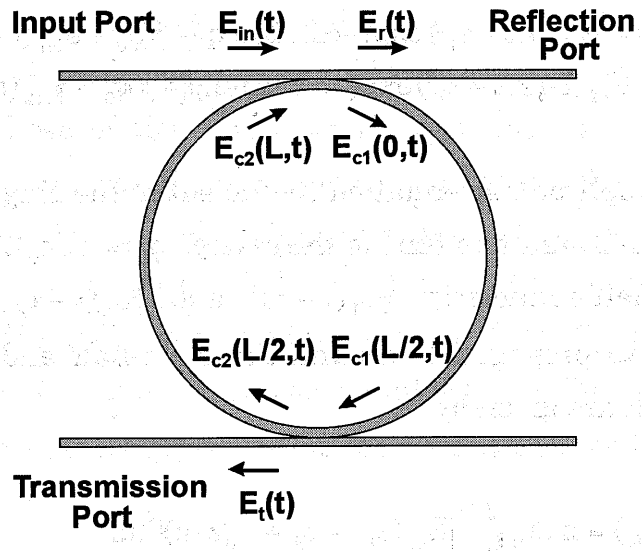

Fig. 4.1. Schematic of a double-coupler nonlinear fiber ring resonator and the definition of each electric field for analysis.

on the analogy of a nonlinear Fabry-Perot resonator.

For the purpose of analysis, the slowly-varying complex electric field at each position are defined as shown in Fig. 4.1. $E_{in}(t)$ is the complex electric field of an incident wave. $E_t(t)$ and $E_r(t)$ are transmitted fields at the transmission and reflection ports, respectively. $E_{c1}(z,t)$ is the field inside the right-half cavity and $E_{c2}(z,t)$ is the left-half cavity field. For the two couplers at the input (or reflection) and transmission ports, the complex field amplitudes are described as follows:

$$E_r(t) = \sqrt{1-\gamma}\left(\sqrt{1-\kappa}E_{in}(t) - j\sqrt{\kappa}E_{c2}(L,t)\right), \tag{4.1}$$

$$E_{c1}(0,t) = \sqrt{1-\gamma}\left(-j\sqrt{\kappa}E_{in}(t) + \sqrt{1-\kappa}E_{c2}(L,t)\right), \tag{4.2}$$

$$E_t(t) = -j\sqrt{1-\gamma}\sqrt{\kappa}E_{c1}(L/2,t), \tag{4.3}$$

$$E_{c2}(L/2,t) = \sqrt{1-\gamma}\sqrt{1-\kappa}E_{c1}(L/2,t), \tag{4.4}$$

where γ and κ are the fractional intensity loss and intensity coupling coefficient of the coupler, respectively. From Eqs. (4.3) and (4.4), the cavity fields $E_{c1}(L/2,t)$ and $E_{c2}(L/2,t)$ can be related to the output field $E_t(t)$ at the transmission port. In the limit of instantaneous relaxation of the nonlinearity, the two cavity fields at both ends of each half ring can be expressed as follows:

$$E_{c1}(L/2,t) = E_{c1}(0,t-\tau_R)\exp(-\alpha L/2)\exp[-j(\phi_0 + \phi_{N1}(t-\tau_R)], \tag{4.5}$$

$$E_{c2}(L,t) = E_{c2}(L/2,t-\tau_R)\exp(-\alpha L/2)\exp[-j(\phi_0 + \phi_{N2}(t-\tau_R)], \tag{4.6}$$

where α is the amplitude attenuation coefficient of the ring fiber and $\tau_R (= n_0 L/2c)$ is the half round-trip time of the cavity. $\phi_0 (= n_0 k_0 L/2)$ is the linear phase shift per half round-trip. $\phi_{N1}(t-\tau_R)$ and $\phi_{N2}(t-\tau_R)$ are nonlinear phase shifts due to propagation around the right-half and left-half rings, respectively, which are given by

$$\begin{aligned}\phi_{N1}(t-\tau_R) &= n_2 k_0 \int_0^{L/2} |E_{c1}(z, t-\tau_R + n_0 z/c)|^2 dz \\ &= n_2 k_0 L_{e1} |E_{c1}(L/2,t)|^2 = n_2 k_0 \frac{L_{e1}}{(1-\gamma)\kappa}|E_t(t)|^2,\end{aligned} \tag{4.7}$$

$$\begin{aligned}\phi_{N2}(t-\tau_R) &= n_2 k_0 \int_0^{L/2} \left|E_{c2}(L/2+z, t-\tau_R + n_0 z/c)\right|^2 dz \\ &= n_2 k_0 L_{e2} \left|E_{c2}(L/2, t-\tau_R)\right|^2 = n_2 k_0 \frac{(1-\kappa)L_{e2}}{\kappa} \left|E_t(t-\tau_R)\right|^2,\end{aligned} \tag{4.8}$$

where L_{e1} and L_{e2} are the effective half cavity length given by

$$L_{e1} = \frac{\exp(\alpha L)-1}{2\alpha}, \qquad L_{e2} = \frac{1-\exp(-\alpha L)}{2\alpha}. \tag{4.9}$$

If the fiber is lossless ($\alpha = 0$), we have $L_{e1} = L_{e2} = L/2$. Using Eqs. (4.2) to (4.6), we obtain the expression for the output field at the transmission port as

$$\begin{aligned}E_t(t) = {} & T \cdot E_{in}(t-\tau_R)\exp\left[-j(\phi_0 + \phi_{N1}(t-\tau_R))\right] \\ & + R \cdot E_t(t-2\tau_R)\exp\left[-j(2\phi_0 + \phi_{N1}(t-\tau_R) + \phi_{N2}(t-2\tau_R))\right],\end{aligned} \tag{4.10}$$

with

$$T = -(1-\gamma)\kappa \exp(-\alpha L/2), \tag{4.11}$$

$$R = (1-\gamma)(1-\kappa)\exp(-\alpha L), \tag{4.12}$$

where T and R just correspond to the mirror transmissivity and reflectivity of the Fabry-Perot resonator, respectively. Equation (4.10) is formally the same as that for the nonlinear Fabry-Perot resonator [1]. However it should be noted that the nonlinear phase shifts $\phi_{N1}(t-\tau_R)$ and $\phi_{N2}(t-\tau_R)$ are different from those of the nonlinear Fabry-Perot resonator, i.e., the two resonators are not equal in response, because there exist counter-propagating fields in the Fabry-Perot resonator. Equation (4.10) is an implicit expression for the output field $E_t(t)$, i.e., $E_t(t)$ to be determined is a function of itself in addition to the former input field $E_{in}(t-\tau_R)$ and output field $E_t(t-2\tau_R)$. Therefore a self-consistent solution for $E_t(t)$ is needed. To the same as above, the expression for the output field at the reflection port can be obtained as

$$\begin{aligned}E_r(t) = {} & \sqrt{1-\gamma}\sqrt{1-\kappa}\{E_{in}(t) + \\ & \exp(-\alpha L/2)E_t(t-\tau_R)\exp\left[-j(\phi_0 + \phi_{N2}(t-\tau_R)\right]\}\ .\end{aligned} \tag{4.13}$$

Since this equation is an explicit expression for the output field $E_r(t)$, one can easily calculate $E_r(t)$ using the known values of $E_{in}(t)$ and $E_t(t-\tau_R)$.

B. Steady-State Analysis

Once the difference equation for describing the dynamics of the ring resonator is given, one can easily derive the steady-state solution by fixing the time-varying input and output fields. Letting $E_{in}(t-\tau_R) = E_{in}$, $E_t(t) = E_t(t-2\tau_R) = E_t$, and substituting these in Eq. (4.10), we have

$$T \cdot E_{in} \exp[-j(\phi_0 + \phi_{N1})] = E_t \{1 - R \cdot \exp[-j(2\phi_0 + \phi_{N1} + \phi_{N2})]\}. \tag{4.14}$$

From the above equation, the following transmissivity of the nonlinear ring resonator is obtained:

$$\frac{|E_t|^2}{|E_{in}|^2} = \frac{T^2}{(1-R)^2 + 4R\sin^2\left(\phi_0 + \frac{\phi_{N1} + \phi_{N2}}{2}\right)}, \tag{4.15}$$

where

$$\frac{\phi_{N1} + \phi_{N2}}{2} = \frac{n_0 n_2 k_0}{4\eta_0}\left[\frac{L_{e1}}{(1-\gamma)\kappa} + \frac{(1-\kappa)L_{e2}}{\kappa}\right]|E_t|^2. \tag{4.16}$$

Since the right-hand side of Eq. (4.15) is a function of $|E_t|^2$, the output intensity $|E_t|^2$ may become a multiple-valued function with respect to the input intensity $|E_{in}|^2$. Therefore, the input-output characteristics can be determined by computing the input intensity $|E_{in}|^2$ for a given output intensity $|E_t|^2$. The transmissivity (4.15) is the same form as that for the linear Fabry-Perot resonator. In the linear case, $(\phi_{N1} + \phi_{N2})/2 = 0$ and resonance takes place when $\phi_0 = n_0 k_0 L/2 = M\pi$ (where M is an integer). We hereafter define the initial detuning as $\Delta\phi_0 = 2\phi_0 - 2M\pi$.

Inserting $E_{in}(t) = E_{in}$, $E_t(t-\tau_R) = E_t$, and $E_r(t) = E_r$ in Eq. (4.13) and further substituting Eq. (4.14) in Eq. (4.13), we obtain the following reflectivity of the nonlinear ring resonator:

$$\frac{|E_r|^2}{|E_{in}|^2} = (1-\gamma)(1-\kappa)\frac{(1-A)^2 + 4A\sin^2\left(\phi_0 + \dfrac{\phi_{N1}+\phi_{N2}}{2}\right)}{(1-R)^2 + 4R\sin^2\left(\phi_0 + \dfrac{\phi_{N1}+\phi_{N2}}{2}\right)}, \tag{4.17}$$

where $A = R - T\exp(-\alpha L/2)$. We can directly determine the output characteristics at the reflection port by substituting the intensities $|E_{in}|^2$ and $|E_t|^2$ in Eq. (4.17).

C. Analysis of Optical Instability

A linear stability analysis of the nonlinear ring resonator is presented on the basis of the above steady-state analysis. Similar to the approach taken in Chap. 3, we add a small disturbance to the steady-state solution over one round-trip time to find a sufficient condition that the output field is unstable. We now consider the following perturbed output field $E_t(t)$:

$$E_t(t) = E_t + \varepsilon(t), \qquad |\varepsilon(t)| << E_t, \tag{4.18}$$

where E_t is the steady-state one and the perturbation is given by

$$\varepsilon(t) = \delta\exp(j\sigma t) + \mu\exp(-j\sigma t). \tag{4.19}$$

From Eq. (4.10), the perturbed output field $E_t(t+2\tau_R)$ after one round-trip is given by the following equation:

$$\begin{aligned} E_t(t+2\tau_R) = {} & T\cdot E_{in}\exp\left[-j(\phi_0 + \phi_{N1}(t+2\tau_R))\right] \\ & + R\cdot E_t(t)\exp\left[-j(2\phi_0 + \phi_{N1}(t+2\tau_R) + \phi_{N2}(t))\right], \end{aligned} \tag{4.20}$$

where

$$\phi_{N1}(t+2\tau_R) = n_2 k_0\left[\frac{L_{e1}}{(1-\gamma)\kappa}\right]|E_t(t+2\tau_R)|^2 \equiv A_1|E_t(t+2\tau_R)|^2, \tag{4.21}$$

$$\phi_{N2}(t) = n_2 k_0\left[\frac{(1-\kappa)L_{e2}}{\kappa}\right]|E_t(t)|^2 \equiv A_2|E_t(t)|^2. \tag{4.22}$$

with $$A_1 = n_2 k_0\left[\frac{L_{e1}}{(1-\gamma)\kappa}\right]^2, \quad A_2 = n_2 k_0\left[\frac{(1-\kappa)L_{e2}}{\kappa}\right]^2. \tag{4.23}$$

Substituting Eq. (4.18) in Eq. (4.20) and further linearizing Eq. (4.20) around the steady-state solution, i.e., neglecting powers of $\varepsilon(t)$ greater than unity, we have the following difference equation for the perturbation:

$$\varepsilon(t+2\tau_R) = -jUA_1\left(E_t\varepsilon^*(t+2\tau_R) + E_t^*\varepsilon(t+2\tau_R)\right)$$
$$-jVE_t\left(A_1\left(E_t\varepsilon^*(t+2\tau_R) + E_t^*\varepsilon(t+2\tau_R)\right) + A_2\left(E_t\varepsilon^*(t) + E_t^*\varepsilon(t)\right)\right) + V\varepsilon(t), \quad (4.24)$$

where

$$U = T\cdot E_{in}\exp\left(-j\left(\phi_0 + A_1|E_t|^2\right)\right), \quad (4.25)$$

$$V = R\cdot\exp\left(-j\left(2\phi_0 + (A_1+A_2)|E_t|^2\right)\right). \quad (4.26)$$

On the other hand, the perturbation $\varepsilon(t+2\tau_R)$ is given by

$$\varepsilon(t+2\tau_R) = \delta\exp(j\sigma t)\exp(j2\sigma\tau_R) + \mu\exp(-j\sigma t)\exp(-j2\sigma\tau_R). \quad (4.27)$$

Substituting Eq. (4.27) in Eq. (4.24) and further expressing Eq. (4.24) in matrix form, we have the following eigenvalue problem:

$$\begin{bmatrix} B_1\exp(j2\sigma\tau_R) + B_2 - \lambda & C_1\exp(j2\sigma\tau_R) + C_2 \\ C_1^*\exp(j2\sigma\tau_R) + C_2^* & B_1^*\exp(j2\sigma\tau_R) + B_2^* - \lambda \end{bmatrix}\begin{bmatrix} \delta \\ \mu^* \end{bmatrix} = 0, \quad (4.28)$$

with

$$B_1 = -jA_1\left(UE_t^* + V|E_t|^2\right), \quad (4.29)$$

$$B_2 = -jA_2V|E_t|^2 + V, \quad (4.30)$$

$$C_1 = -jA_1\left(UE_t + VE_t^{\,2}\right), \quad (4.31)$$

$$C_2 = -jA_2VE_t^{\,2}, \quad (4.32)$$

where $\lambda = \exp(j2\sigma\tau_R)$ is an eigenvalue to be determined. Note that Eq. (4.28) is a pseudo-eigenvalue problem since the elements of the matrix contain the

eigenvalue λ. Setting the determinant of the coefficient matrix equal to zero, we have the following characteristic equation:

$$\lambda^2\left(|B_1-1|^2-|C_1|^2\right)+2\lambda\,\mathrm{Re}\left[(B_1-1)B_2^*-C_1C_2^*\right]+\left(|B_2|^2-|C_2|^2\right)=0. \qquad (4.33)$$

The steady-state solution E_t is stable only when the absolute value of the eigenvalue λ is less than unity.

4.3 Numerical Results and Discussions

We investigate numerically the dynamic properties of optical bistability and instability in the double-coupler nonlinear fiber ring resonator with a mind to a subsequent experimental study. If we use commercially available fiber couplers, the attainable minimum length of the ring is 10~20 cm at the most. Parameters in Table 3.1 and the form of temporal incident pulse, Eq. (3.43) are also used in the following calculation. Switch-on and switch-off powers P_{SH} and P_{SL} for optical bistability and threshold powers P^i_{UL} and P^i_{UH} (where $i = A, B$) for Ikeda instability have been defined in Fig. 3.3.

Figure 4.2 shows the dependence of the switching powers P_{SH} and P_{SL} and the threshold powers P^i_{UL} and P^i_{UH} on the initial detuning $\Delta\phi_0$ for two values of the coupler loss $\gamma = 0$ and 0.1. Since our interest is whether Ikeda instability interrupts bistable device application or not, the ratio of minimum power for Ikeda instability to minimum power for bistability, P^B_{UL}/P_{SH}, is also shown. Figure 4.3 shows the dependence of these four critical powers P_{SH}, P_{SL}, P^i_{UL}, and P^i_{UH} on the initial detuning $\Delta\phi_0$ for two values of the coupling coefficient $\kappa = 0.1$ and 0.2. The results in Figs. 4.2 and 4.3 also are useful for other lengths of the fiber ring since these threshold and switching powers are inversely proportional to the ring length. The threshold power P^B_{UL} to induce Ikeda instability in the high-transmission state (marked by B) decreases with increasing initial detuning $|\Delta\phi_0|$. The instability threshold power P^B_{UL} also becomes less than P^A_{UL} in the low-transmission state (marked by A) for $\Delta\phi_0 < -\pi$. However it should be noted that, since $P^A_{UH} < P_{SH}$ in such a region, the output is unstable in the low-transmission state before it is switched to

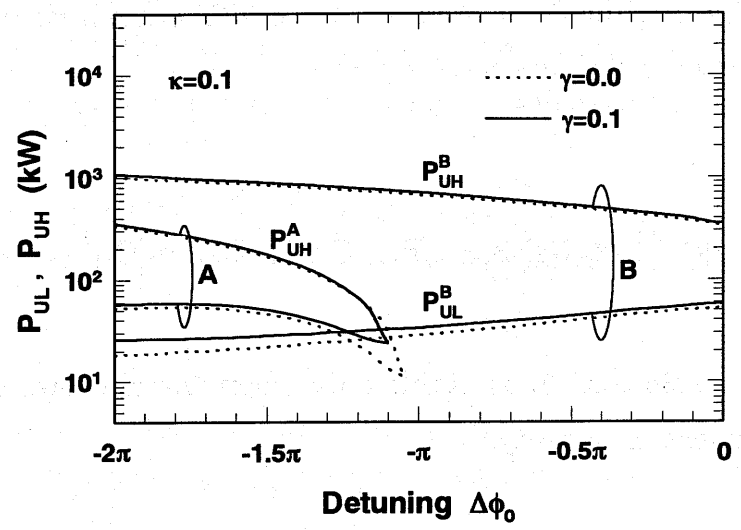

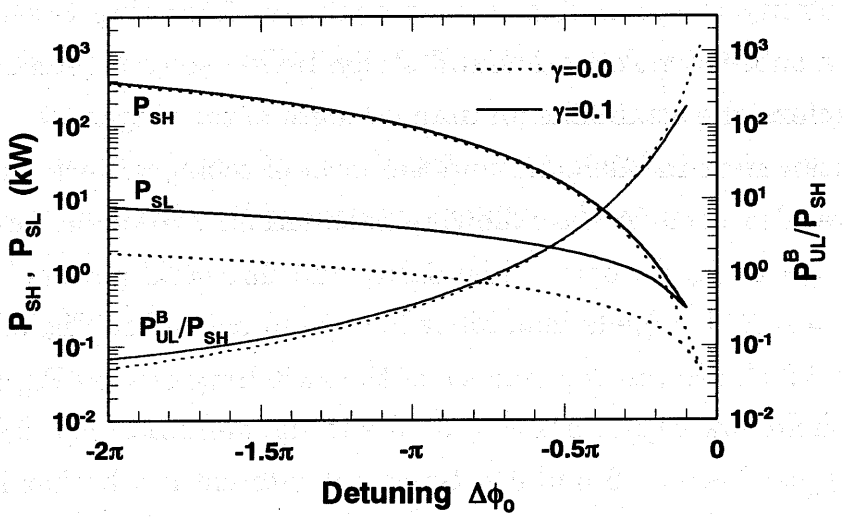

Fig. 4.2. (a) Instability threshold powers P_{UL} and P_{UH} and (b) bistability switching powers P_{SH} and P_{SL} as a function of the initial detuning $\Delta\phi_0$ for two values of coupler loss γ. Labels A and B represent the unstable regions in Fig. 3.3.

the high-transmission state. The width of the hysteresis loop, $P_{SH}-P_{SL}$, decreases with decreasing initial detuning $|\Delta\phi_0|$ and vanishes at a critical point near resonance where we can obtain differential gain. On the other hand, the ratio, P^B_{UL}/P_{SH}, increases with decreasing initial detuning and reaches about 100, almost independently of the values of γ and κ. We therefore conclude that Ikeda instability hardly interrupt bistable application

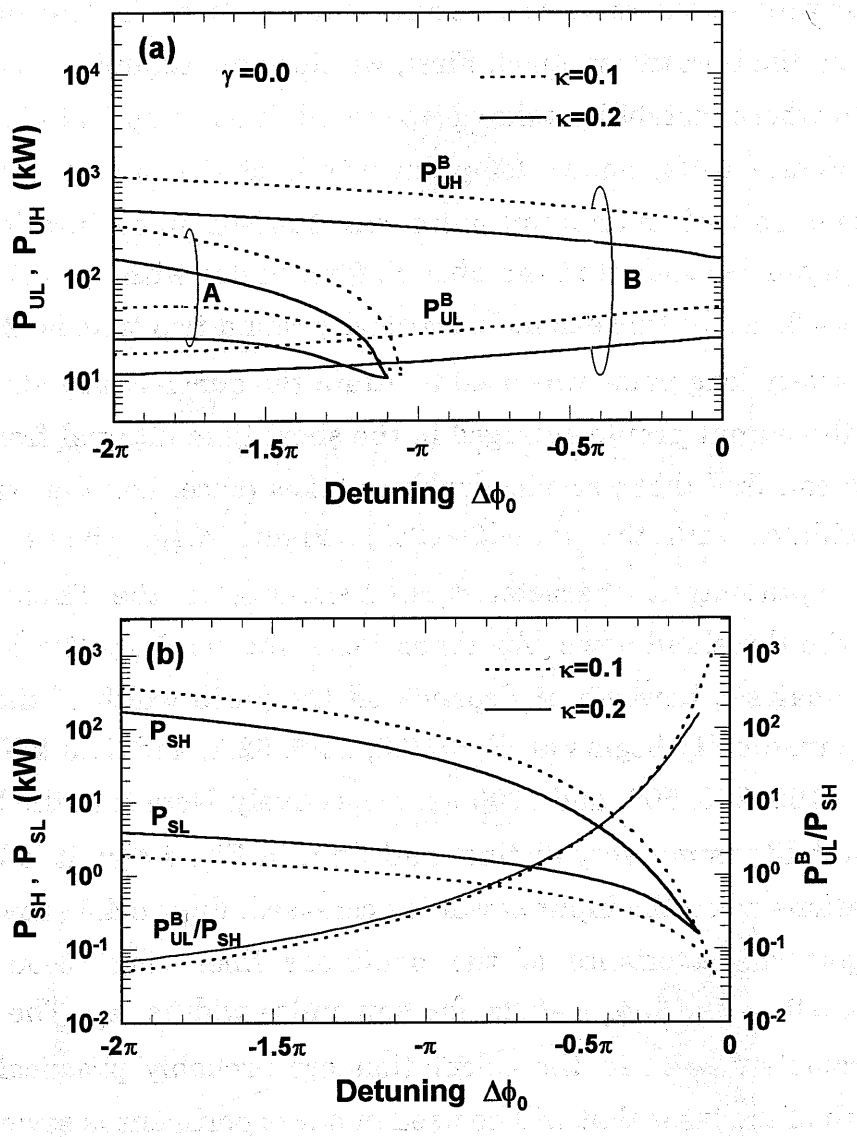

Fig. 4.3. (a) Instability threshold powers P_{UL} and P_{UH} and (b) bistability switching powers P_{SH} and P_{SL} as a function of the initial detuning $\Delta\phi_0$ for two values of coupling coefficient κ.

since the device operation is usually done near resonance. It is also interesting to compare the dependence of the unstable regions on the initial detuning with that of other nonlinear resonators. From a resemblance of the structures, we found that the general dependence of the two-coupler ring resonator is similar to that of the Fabry-Perot resonator [1]. Although the instabil-

ity threshold of a special Fabry-Perot resonator of zero transmission has been calculated in terms of the intracavity intensity by Firth [2] the results are not always useful for experimentalists.

Next, we present the numerical results obtained from the transient analysis based on the iterative method. First, we show an example of the numerical results where instability takes place in addition to optical bistability in Fig. 4.4. Figure 4.4(a) shows temporal profile of the output pulse at the transmission port when an input pulse with 1000-ns pulse duration and 60-kW peak power is incident in the fiber ring resonator with $\gamma = 0.1$, $\kappa = 0.1$, and $\Delta\phi_0 = -0.3\pi$. In this example, the cavity round-trip time is $2\tau_R = 0.483$ ns and the very long pulse was used to attain the quasi-steady state. Figure 4.4 (b) is the output profile enlarged in the short time interval from -5 ns to +5 ns. We can find that periodic doubling takes place, i.e., the transmitted power oscillates with the period $2 \times (2\tau_R)$. Figure 4.4(c) shows the corresponding input-output characteristics. According to the linear stability analysis, the threshold power for Ikeda instability is P^B_{UL}=49.2 kW. In the transient analysis, however, it depends on the pulse width of the incident pulse. The instability begins at P_{in} =57.3, 54.5, 52.1, and 51.0 kW for pulse width τ_P = 100, 200, 500, and 1000 ns, respectively. Note that the beginning of the instability is not very distinct and that, in Fig. 4.4(c), it is hidden by the oscillations when the input power is decreased. Figure 4.5 shows the two input-output characteristics of the nonlinear fiber ring resonator with $\gamma = 0.1$, $\kappa = 0.1$, and $\Delta\phi_0 = -0.2\pi$ for four pulse widths τ_P. The values of these parameters used in the calculation are probably practical and the pulse width of the laser that will be used in our experiment is several tens of nanoseconds. We obtain a counterclockwise hysteresis loop in transition and a clockwise hysteresis loop in reflection. An overshoot and undershoot always take place in the on-off switching. As the pulse width increases, the width of the hysteres is loop decreases and approaches the steady-state solution. The response for a pulse width $\tau_P = 2000$ ns almost agrees the steady-state solution except for the overshoot and undershoot. The switching speed of the device is governed by the cavity build-up time $\tau_c = 2\tau_R/(1-R^2)$, where R is the effective mirror reflectivity given by Eq. (4.12). In this example, τ_c = 1.41ns. We can have the quasi-steady state for $\tau_P > 500\tau_c \sim 1000\tau_c$.

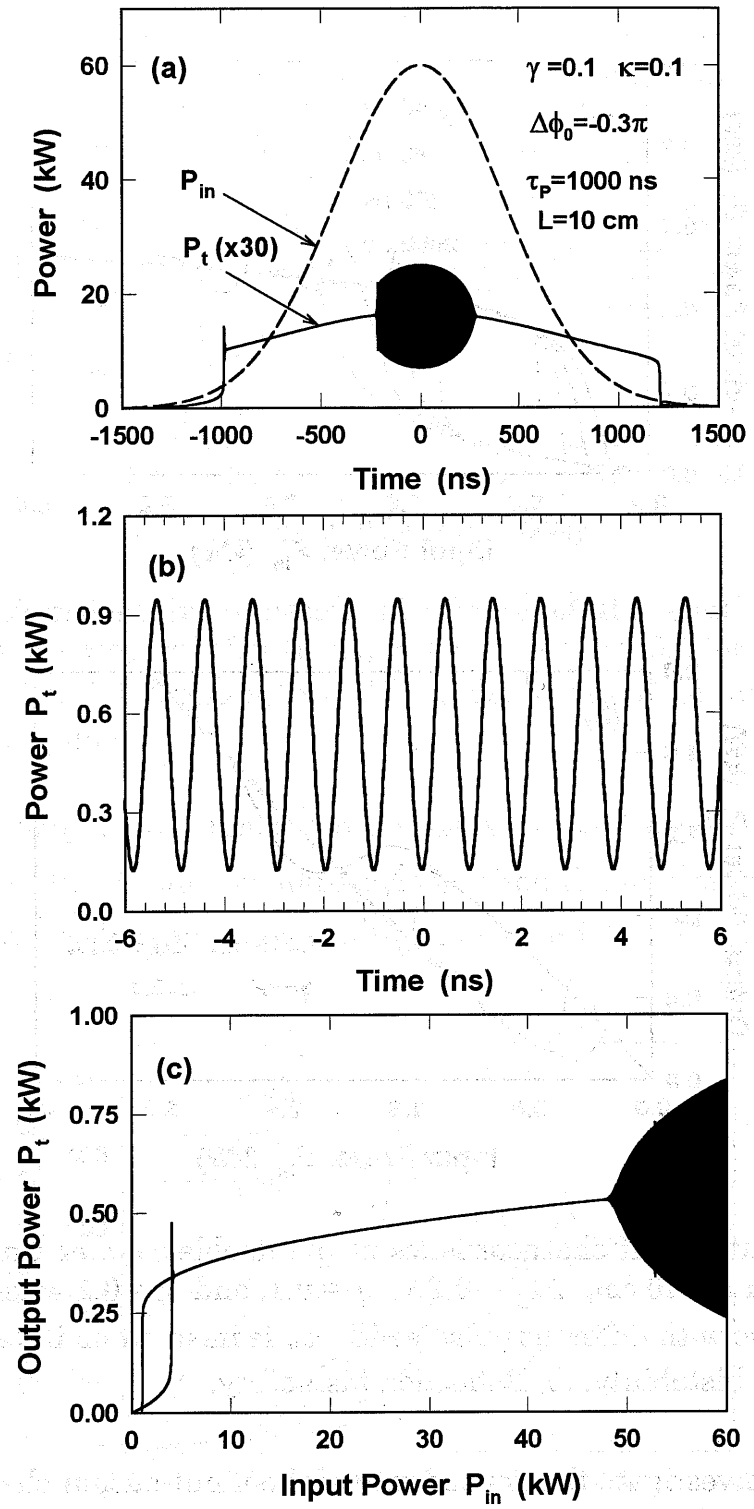

Fig. 4.4. Nonlinear pulse response of the double-coupler ring resonator with $L = 10$ cm, $\Delta\phi_0 = -0.3\,\pi$, $\gamma = 0.1$, and $\kappa = 0.1$ when an optical pulse with $\tau_P = 1000$ ns is incident on it. (a) Temporal profile of the incident and transmitted pulses. (b) Enlarged profile of the transmitted pulse around $t = 0$. (c) Input-output characteristics corresponding to (a).

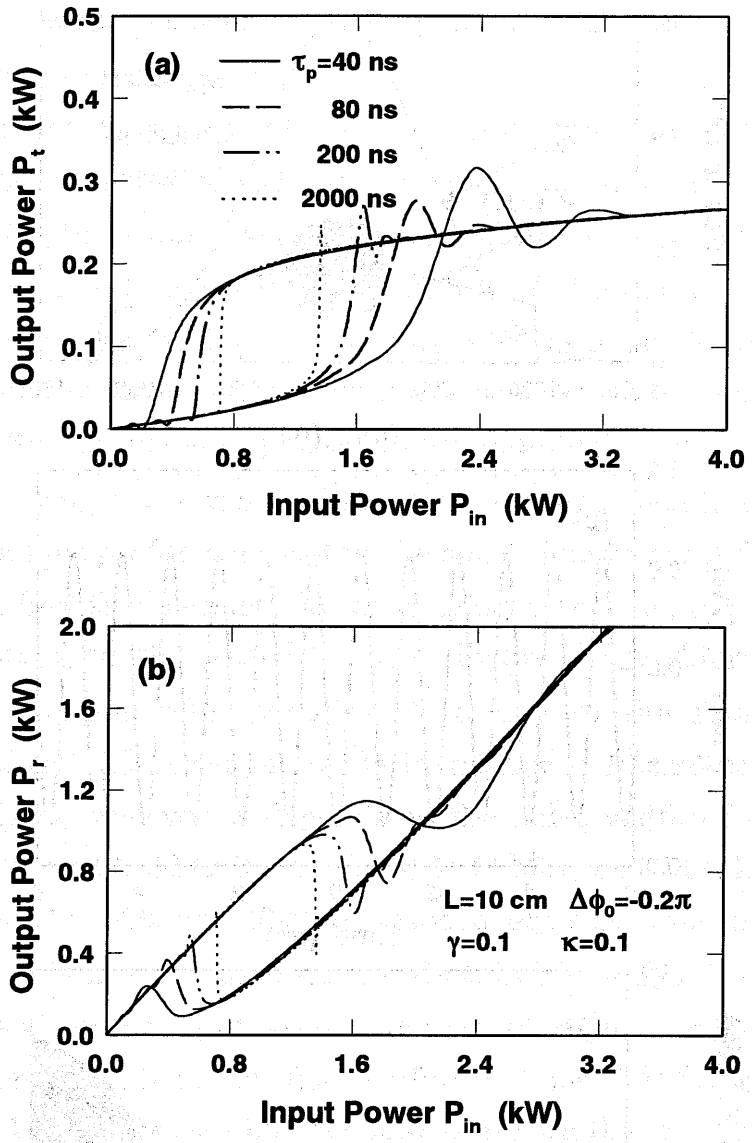

Fig. 4.5. Input-output characteristics of the double-coupler ring resonator with L= 10 cm, $\Delta\phi_0 = -0.2\pi$, $\gamma = 0.1$, and $\kappa = 0.1$ when an optical pulse with different pulse width τ_P is incident on it. (a) Transmission bistability. (b) Reflection bistability.

We moreover investigate the dependence of the input-output characteristics on the detuning, the fractional intensity loss and intensity coupling coefficient of the coupler by using an input pulse with 40-ns pulse duration and 4-kW peak power. Figure 4.6 shows the input-output characteristics for the different values of the initial detuning. The width of the hysteresis loop increases with the initial detuning as predicted by the steady-state analysis.

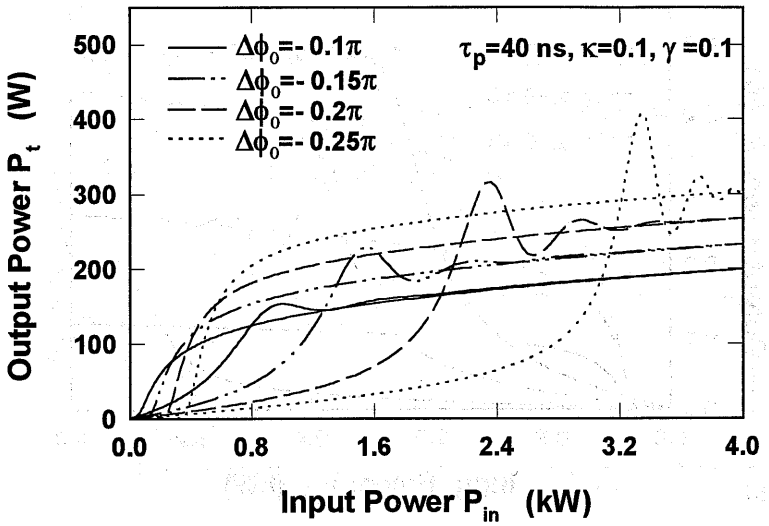

Fig. 4.6. Transient transmission bistability of the double-coupler ring resonator with L = 10 cm, $\gamma = 0.1$, and $\kappa = 0.1$ for several values of initial detuning $\Delta\phi_0$. The pulse width of an incident pulse is $\tau_P = 40$ ns.

Since a ring length L = 10 cm is too transient for a pulsewidth $\tau_P = 40$ ns, we cannot obtain the distinct hysteresis loop when the detuning is small. Figures 4.7 and 4.8 show the input-output characteristics when the fractional

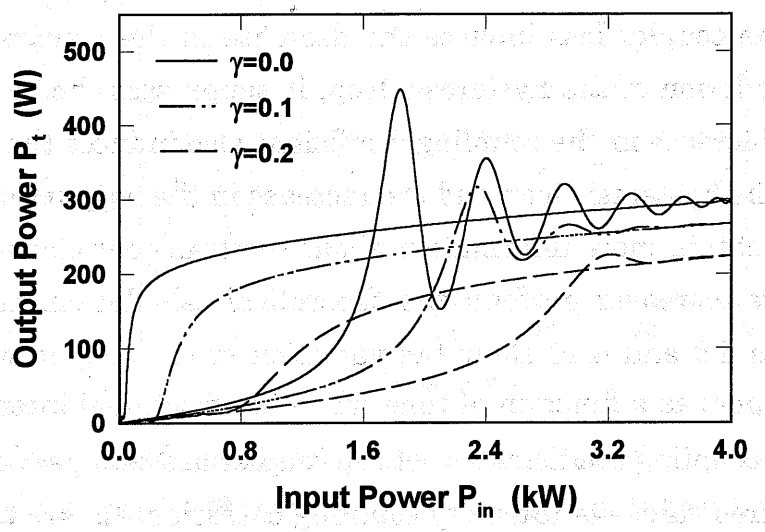

Fig. 4.7. Transient transmission bistability of the double-couple ring resonator with L = 10 cm, $\Delta\phi_0 = -0.2\pi$, and $\kappa = 0.1$ for several values of coupler loss γ. The input pulse is the same as that in Fig. 4.6.

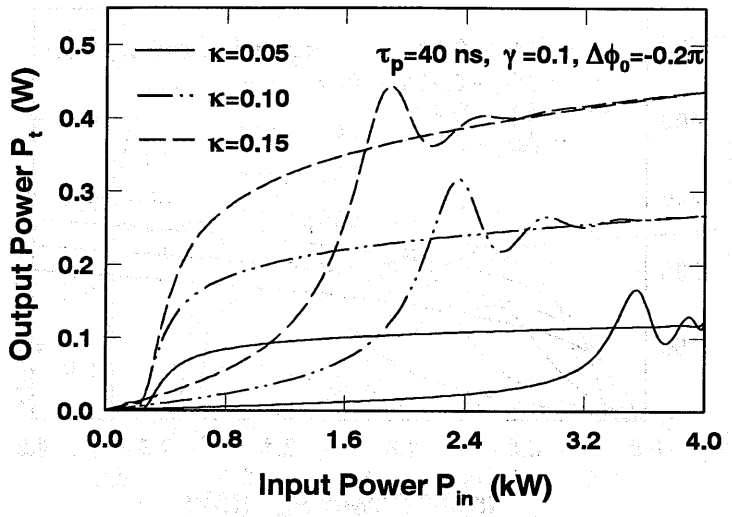

Fig. 4.8. Transient transmission bistability of the double-coupler ring resonator with L = 10 cm, $\Delta\phi_0 = -0.2\pi$, and $\gamma = 0.1$ for several values of coupling coefficient κ. The input pulse is the same as that in Fig. 4.6.

intensity loss γ and intensity coupling coefficient κ of the coupler are changed, respectively. From Eqs. (4.11) and (4.12), we can understand that the coupler loss affects the mirror transmissivity and reflectivity of the equivalent Fabry-Perot resonator equally and the increase in the coupling coefficient leads to the decrease in the mirror reflectivity. Although the increase in the coupler loss induces the decrease in the transmitted power and the degradation of the hysteresis loop, it suppresses the overshoot and ringing. The increase in the coupling coefficient also induces the decrease in the width of the hysteresis loop and the increase in the output power.

In order to obtain more information about the transient characteristics of the device, we moreover perform the theoretical calculations using a step input. Figures 4.9 and 4.10 show the variation of the output signal at the transmission port as a function of time when the fractional intensity loss γ and intensity coupling coefficient κ of the coupler are changed, respectively. In Fig. 4.9, three values of intensity coupling coefficient κ are used when a step input with 40-kW peak power is incident in the fiber ring resonator with L = 10 cm, $\kappa = 0.1$, and $\Delta\phi_0 = -0.2\pi$. In Fig. 4.10, three values of coupler loss γ are used while other parameters are kept constant. From both of these figures, it is found that there exists a relaxation oscillation in the output

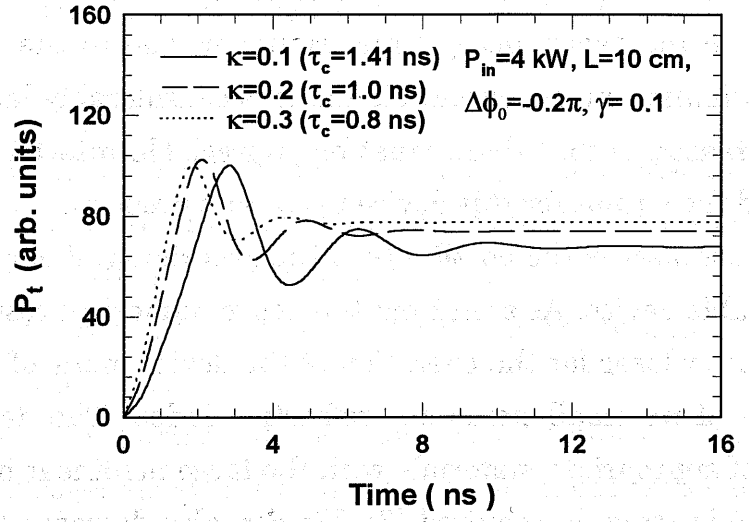

Fig. 4.9. Variation of the output power as function of time for three values of the intensity coupling coefficient κ in a double-coupler ring resonator with L = 10 cm, $\Delta\phi_0 = -0.2\pi$, P_{in} = 4 kW, and $\gamma = 0.1$.

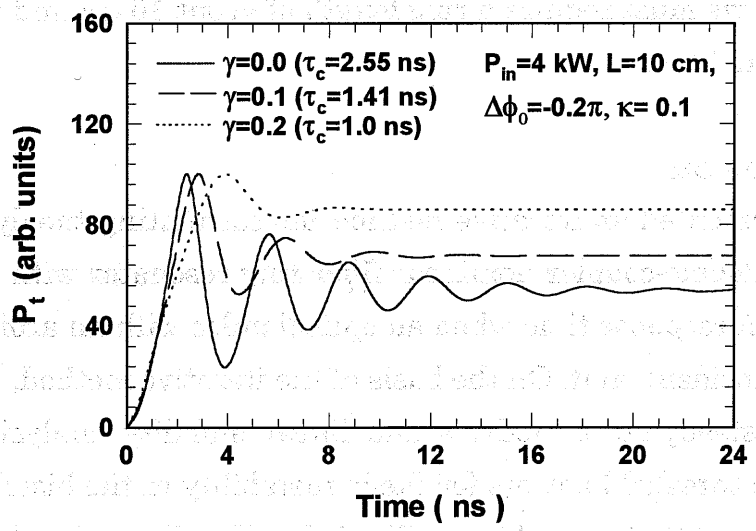

Fig. 4.10. Variation of the output power as function of time for three values of the fractional intensity loss γ in a double-coupler ring resonator with L = 10 cm, $\Delta\phi_0 = -0.2\pi$, P_{in} = 4 kW, and $\kappa = 0.1$.

signal and the duration of this oscillation decreases with increasing the values of γ or κ. Moreover, it is found that the relaxation duration is ap-

proximately the order of 8~10 times the cavity decay time τ_c ($=2\tau_R/(1-R^2)$). It is general considered that the response time of the fiber ring device is nearly equal to the cavity decay time. However, due to the occurrence of relaxation oscillation in the output signal, it is considerably larger than the time τ_c. The reason is that there must be appreciable interference between the input and the output for this device to operate properly.

Here we must discuss the possibility of the experimental demonstration of the fiber bistable device. As seen from the above numerical results, we must use a high power laser for the operation of the device made of a fused silica fiber because of its small nonlinear refractive index. The development of fibers made of appropriate materials with the large nonlinear index and fast response time is strongly required [3]. We can also decrease the switching power by increasing the length of the fiber ring. However the increase in the ring length brings about the decrease in the switching speed and requires the long coherence time of the exciting source corresponding to its cavity decay time. Therefore we will aim to develop a high-speed device at the cost of an increase in the switching power. To gain the response time of a few nanoseconds, we must require a ring length of about 10 cm and an operating power of about 1 kW.

4.4 Conclusion

We have presented an iterative method for calculating the dynamic properties of the double-coupler nonlinear fiber ring resonator with an instantaneous medium response time when an optical pulse with an arbitrary temporal profile is incident on it. On the basis of the iterative method, we have also presented a steady-state analysis and linear stability analysis, and have examined the threshold powers for Ikeda instability in the bistable device in detail. It is found that optical bistability is hardly affected by Ikeda instability since the instability threshold is much higher than the bistability switching power for the initial detuning where the bistable device is operated. It is also found that the general features of the instability in the bistable device is similar to that of the nonlinear Fabry-Perot resonator. The transient optical bistability and instability have been calculated by using the iterative method. Although we are planning to demonstrate optical bistabil-

ity and instability in the present device, we could obtain sufficient information about the instability and a good guide to the design of the device.

References

[1] K. Ogusu, H. Li, and T. Kamizono, "Analysis of transient optical bistability and stability in a nonlinear fiber Fabry-Perot resonator based on an iterative method," Opt. Rev. 5 (1998) 185.

[2] W. J. Firth, "Stability of nonlinear Fabry-Perot resonators," Opt. Commun. 39 (1981) 343.

[3] M. Asobe, T. Kanamori, and K. Kubodera, "Applications of highly nonlinear chalcogenide glass fibers in ultrafast all-optical switches," IEEE J. Quantum Electron. 29 (1993) 2325.

Chapter 5. Stimulated Brillouin Scattering in a Single-Mode Optical Fiber

5.1 Introduction

As described in chapter 1, there has been a considerable interest in a fiber resonator in recent years because of its potential applications to optical bistable devices and other fiber-based devices. However, most of the applications using the nonlinearities of the fiber have not been exploited because the circulating power in such a resonator is limited by stimulated Brillouin scattering (SBS) [1]. In this chapter, we discuss the dynamic behavior of SBS in a time region which is nearly the same order of magnitude as the phonon lifetime. We investigate experimentally the transient SBS in a short fused fiber of length 50 cm with 14-ns pulse from a single-mode YAG laser. The experimental results are also compared with the theory based on the couple-amplitude equations. It is general considered that SBS can not occur when the pulse width of the pump pulses is in the range of several nanoseconds [2], but contrary to this, we theoretically and experimentally show that SBS can occur even in the nanosecond region and pulse narrowing for the transmitted pulse also takes place as a result of the transient process. Moreover we investigate theoretically the instability of SBS when a pump pulse is incident into a short fiber.

5.2 Transient Stimulated Brillouin Scattering in a Single-Mode Optical Fiber

A. Theory

SBS is a three-wave parametric mixing process which couples two radiation fields (i.e., the incident pump field E_p and the created Stokes field E_s) with an acoustic matter-density field $\Delta\rho$ in the active medium. For a single-mode optical fiber, these fields can be approximately expressed as plane waves propagating along the z axis by

$$E_p(z,t) = \tfrac{1}{2}\varepsilon_p(z,t)\exp\left(j(\omega_p t - k_p z)\right) + \text{c.c.}, \tag{5.1}$$

$$E_s(z,t) = \tfrac{1}{2}\varepsilon_s(z,t)\exp\left(j(\omega_s t + k_s z)\right) + \text{c.c.}, \tag{5.2}$$

$$\Delta\rho(z,t) = \tfrac{1}{2}\rho(z,t)\exp\left(j(\omega_A t - k_A z)\right) + \text{c.c.}, \tag{5.3}$$

where $\omega_A = \omega_p - \omega_s$ and $k_A = k_p + k_s \approx 2k_p$. $\omega_p(k_p)$, $\omega_s(k_s)$, and $\omega_A(k_A)$ are the angular frequencies (wave numbers) of pump, backward-propagating Stokes, and acoustic waves, respectively. The coupled equations are derived from the following wave equation (in SI units) and the Navier-Stokes equation [3]

$$\nabla^2 E - \frac{n_0^2}{c^2}\frac{\partial^2 E}{\partial t^2} - \frac{n_0 \alpha}{c}\frac{\partial E}{\partial t} = \mu_0 \frac{\partial^2 P^{NL}}{\partial t^2}, \tag{5.4}$$

$$\left[\frac{\partial^2}{\partial t^2} + 2\Gamma_A \frac{\partial}{\partial t} - v_A^2 \nabla^2\right]\Delta\rho = -\frac{1}{2}\rho_0 \varepsilon_0 \frac{\partial n^2}{\partial \rho}\nabla^2 (E \cdot E), \tag{5.5}$$

where P^{NL} is the nonlinear polarization, α is the fiber loss coefficient, c is the velocity of the light in the vacuum, v_A is the velocity of the acoustic wave, n_0 and ρ_0 are the linear refractive indexes and the average density of the fiber, respectively. $\tau_A = \Gamma_A^{-1}$ is the phonon damping time. ε_0 and μ_0 are the electric and magnetic permittivity of vacuum. E is the total optical field, i.e., $E = E_p + E_s$. The nonlinear polarization is expressed as

$$P^{NL} = \varepsilon_0 \left(\Delta\rho \frac{\partial n^2}{\partial \rho} + 2 n_0 n_2 |E|^2\right) E. \tag{5.6}$$

In Eq.(5.6), the first term of the right-hand side is the electrostriction effect, which is related to the Brillouin gain. The second term is the optical Kerr effect. Substituting Eqs. (5.1)-(5.3) and (5.6) into Eqs. (5.4) and (5.5), and using a slowly varying amplitude approximation, we obtain the following coupled-amplitude equations:

$$\begin{aligned}\frac{\partial \varepsilon_p(z,t)}{\partial t} + \frac{c}{n_0}\frac{\partial \varepsilon_p(z,t)}{\partial z} = &-\frac{\alpha c}{2n_0}\varepsilon_p(z,t) - j g_1 \cdot \varepsilon_s(z,t) \cdot \rho(z,t) \\ &- j\frac{n_2 \omega_p}{n_0}\left(|\varepsilon_p(z,t)|^2 + 2|\varepsilon_s(z,t)|^2\right)\cdot \varepsilon_p(z,t),\end{aligned} \tag{5.7}$$

$$\frac{\partial \varepsilon_s(z,t)}{\partial t} - \frac{c}{n_0}\frac{\partial \varepsilon_s(z,t)}{\partial z} = -\frac{\alpha c}{2n_0}\varepsilon_s(z,t) - jg_1 \cdot \varepsilon_p(z,t)\cdot \rho^*(z,t) - j\frac{n_2\omega_s}{n_0}\left(2\left|\varepsilon_p(z,t)\right|^2 + \left|\varepsilon_s(z,t)\right|^2\right)\cdot \varepsilon_s(z,t), \tag{5.8}$$

$$\frac{\partial \rho(z,t)}{\partial t} + v_A\frac{\partial \rho(z,t)}{\partial z} = -\Gamma_A \rho(z,t) - jg_2\varepsilon_p(z,t)\cdot \varepsilon_s^*(z,t) + f(z,t), \tag{5.9}$$

with

$$g_1 = \frac{\omega_p^2}{4k_p c^2}\cdot\frac{c}{n_0}\cdot\frac{\partial n^2}{\partial \rho} = \frac{\pi n_0^2 p_{12} c}{2\lambda \rho_0}, \tag{5.10}$$

$$g_2 = \frac{k_A}{4v_A}\rho_0\varepsilon_0\frac{\partial n^2}{\partial \rho} = \frac{\pi n_0^5 p_{12}\varepsilon_0}{\lambda v_A}, \tag{5.11}$$

where $\omega_p = \omega_s = \omega$ and $k_p = k_s = n_0 k_0 (=2\pi n_0/\lambda)$ are assumed and g_1 and g_2 are the photon-phonon coupling coefficients. P_{12} is the photoelastic constant of the fiber. λ is the optical wavelength in the free-space. The term $v_A\partial\rho(z,t)/\partial z$ in Eq. (5.9) is neglected since the velocity of the acoustic wave is much less than that of the light. The term f(z,t) in Eq. (5.9) is the Langevin noise source which describes the thermal fluctuation in the density of the fiber that leads to spontaneous Brillouin scattering [4]. The Brillouin gain coefficient g_{B0} is related to g_1 and g_2 by [2]

$$g_{B0} = \frac{2\pi^2 n_0^7 p_{12}^2}{c\lambda^2 \rho_0 v_A \Gamma_A} = \frac{4g_1 g_2}{\Gamma_A}\cdot\mu_0 . \tag{5.12}$$

It should be noted that the pump and Stokes waves are assumed to be polarization matched in the above formulation (i.e., the fiber used is assumed to be a polarization-maintaining fiber). For the case of nonpolarization maintaining fiber, due to the polarization scrambling effect, the Brillouin gain coefficient is reduced to $g_{B0}/2$ for 45□ polarization scrambling [2].

B. Numerical analysis

We transform Eqs.(5.7)-(5.9) along the characteristics by substituting

$$H_p(z,t) = \varepsilon_p(z + v \cdot t, t), \tag{5.13}$$

$$H_s(z,t) = \varepsilon_s(z - v \cdot t, t), \tag{5.14}$$

$$A(z,t) = \rho(z + v_A \cdot t, t), \tag{5.15}$$

then Eqs.(5.7)-(5.9) become

$$\begin{aligned}\frac{\partial H_p(z,t)}{\partial t} = {} & \frac{\alpha c}{2n_0} H_p(z,t) - jg_1 \cdot H_s(z + 2v \cdot t, t) \cdot A(z + (v - v_A) \cdot t, t) \\ & - j\frac{n_2 \omega_p}{n_0}\left(|H_p(z,t)|^2 + 2|H_s(z + 2vt, t)|^2\right) \cdot H_p(z,t),\end{aligned} \tag{5.16}$$

$$\begin{aligned}\frac{\partial H_s(z,t)}{\partial t} = {} & -\frac{\alpha c}{2n_0} H_s(z,t) - jg_1 \cdot H_p(z - 2v \cdot t, t) \cdot A^*(z - (v + v_A) \cdot t, t) \\ & - j\frac{n_2 \omega_s}{n_0}\left(2|H_p(z - 2vt, t)|^2 + |H_s(z,t)|^2\right) \cdot H_s(z,t),\end{aligned} \tag{5.17}$$

$$\frac{\partial A(z,t)}{\partial t} = -\Gamma_A A(z,t) - jg_2 H_p(z - vt, t) \cdot H_s^*(z + vt, t) + f(z,t). \tag{5.18}$$

The above equations will no longer have partial derivatives with respect to z. We can then use a fifth-order Runge-Kutta algorithm to integrate the above equation from one time step to the next. We numerically solve the Eqs. (5.16)-(5.18) by using the method of characteristics [5] and examine the transient effect of SBS in a single-mode fiber. We also assume that the pump source is a Q-switched YAG laser and the value of τ_p = 14 ns is used in our simulation as a comparison with our experimental results. Other parameters used in the following calculation are listed in Table 5.1.

First, we investigate the dependence of the transient SBS on different parameters, such as the input peak power, the pulse width of the incident pulse, and the fiber length. Figure 5.1 shows the temporal intensity profiles of transmitted and Stokes pulses for the fiber length L = 0.5 m and the incident pulse width τ_p = 14 ns. This pulse width is nearly equal to the phonon damping time τ_A. In Fig. 5.1, the incident, transmitted, and Stokes pulses are represented by P_{in}, P_t, and P_s, respectively. The pump wave is hardly depleted when the input peak power is lower than 150 W, as shown in Fig. 5.1(a). This

Table 5.1. The related parameters used in the theoretical calculation.

Medium	Single-mode fiber
Linear refractive index n_0	1.454
Nonlinear refractive index n_2	1×10^{-22} m^2/V^2
Effective mode area S_{eff}	50 μm^2
Fiber loss α	0
Wavelength λ.	1.06 μm
Phonon damping time τ_A	1.0×10^{-9} s
Average density of the medium ρ_0	2210 kg/m^3
Velocity of the acoustic wave v_A	5960 m/s
Photo-elastic constant of the fiber p_{12}	0.286
Maximum Brillouin gain coefficient g_{B0}	5.0×10^{-11} m/W

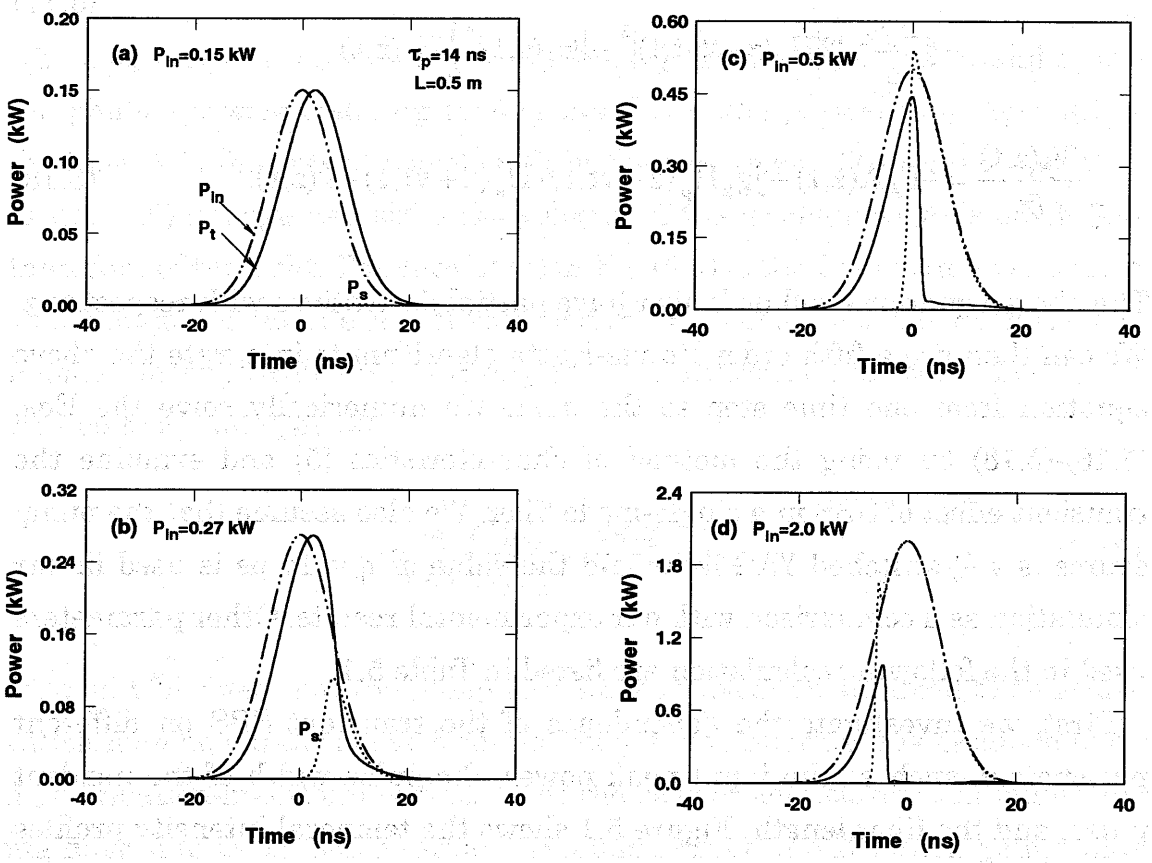

Fig. 5.1. Temporal intensity profiles of incident, transmitted and Stokes pulses for L = 0.5 m, $n_2 = 1\times10^{-22}$ m^2/V^2, and τ_p = 14 ns at different input peak powers: (a) 0.15 kW, (b) 0.27 kW, (c) 0.5 kW, and (d) 2.0 kW.

value is larger than the cw threshold $P_{th} = 21\times A_{eff}/g_B L$ = 42 W [6]. However,

when the input peak power is several times larger than the threshold, the pump wave is significantly depleted as a result of the occurrence of SBS. A large change in the temporal intensity profile of the transmitted pulse is observed. SBS occurs even if the incident pulse has a pulse width of 14 ns, as long as the incident power is higher than the SBS threshold. It is found that the pulse width of the transmitted pulse is compressed compared with that of the incident pulse. The compression ratio increases with increasing incident power. This pulse compression is attributed to the transient effect of SBS.

Figure 5.2 shows the temporal intensity profiles of transmitted and Stokes pulses for P_p =500 W, L=0.5 m, and τ_p = 2 and 50 ns. SBS does not occur for τ_p =2 ns even if the incident power is nearly 12-fold higher than the cw threshold, as shown in Fig. 5.2(a). As the pulse width is increased to 50 ns, the pump wave is significantly depleted and pulse compression for the transmitted signal becomes poor as shown in Fig. 5.2(b). Compared with Fig. 5.1, it is also found that the SBS threshold depends on the pulse width of the incident pulse and increases with decreasing pulse width.

Figure 5.3 shows the temporal intensity profiles of the three pulses for P_{in}= 270 W, τ_p = 14 ns, and L = 2 and 4 m. It is found that the pump wave is significantly depleted in both of these cases, as shown in Figs. 5.3(a) and (b). However, the transmitted signal and the created Stokes signal change negligibly as the fiber length is changed from 2 to 4 m. Compared with Fig. 5.1(b), it is found that there exists a strong saturation for the power of SBS when the fiber is longer than 2 m. This phenomenon has also been observed in a long fiber under a cw pump [2], [7].

To obtain more information about the transient SBS, we investigate the dependence of SBS on the pulse width as it is much larger than the phonon damping time. Figure 5.4 shows the temporal intensity profiles of incident, transmitted, and Stokes pulses for three values of τ_p. In this figure, the fiber length is assumed to be 100 m, the input peak power is fixed at 1 W, and the other parameters remain the same. We can see that the pulse compression described above does not occur. It is also found that there exists a relaxation oscillation in the transmitted and Stokes signals in Figs. 5.4(a) and (b), and the period duration of the oscillation is almost equal to the round-trip time t_r (= $2n_0L/c$) within the fiber. The physical origin of such a relaxation oscillation

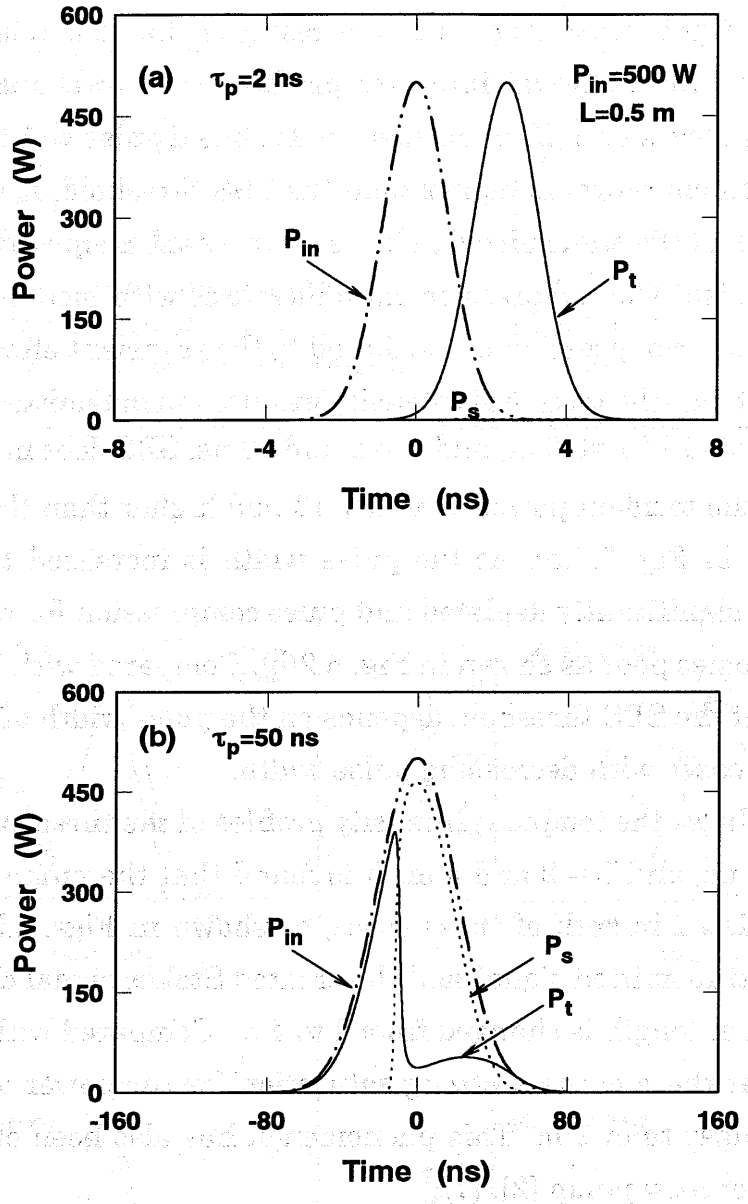

Fig. 5.2. Temporal intensity profiles of incident, transmitted and Stokes pulses for L=0.5 m, $n_2 = 1\times10^{-22}$ m^2/V^2, and P_{in} = 500 W. Pulse widths are (a) 2 ns and (b) 50 ns.

has been described in Refs. [8] and [9]. However, it should be noted that this oscillation does not appear in Fig. 5.1, where the fiber used is very short. The reason may be explained as follows. For a short fiber, the round-trip time is less than the phonon response time and thus, the transmitted and Stokes pulses cannot follow the round-trip time oscillation. The oscillation can be observed only if the condition $t_r \gg \tau_A$ is satisfied. Furthermore, the pulse

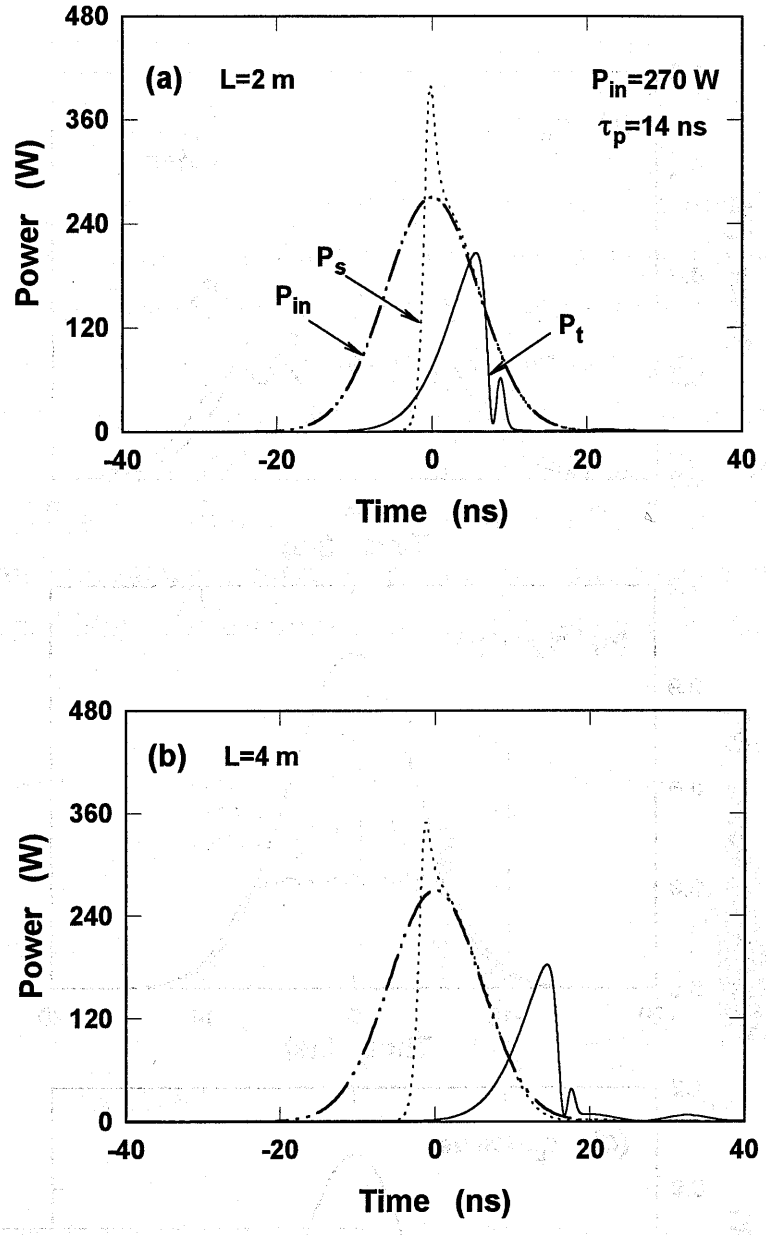

Fig. 5.3. Dependence of transmitted and Stokes signals on the fiber length for τ_p = 14 ns, $n_2 = 1\times10^{-22}$ m^2/V^2, and P_{in} = 270 W. Fiber lengths are (a) 2 m and (b) 4 m.

widths of the incident pulse in Figs. 5.4(a), (b), and (c) are approximately equal to $5t_r$, $10t_r$ and $100t_r$, respectively. As the pulse width increases, the amplitude of the oscillation decreases and finally disappears. For $\tau_p = 100t_r$, we obtain the steady-state solution of SBS.

Finally, we investigate the instability of SBS under a pulsed pump. It is generally considered that SBS may become unstable if the pump power is high enough, even if there is no external feedback [10], [11]. In our numerical

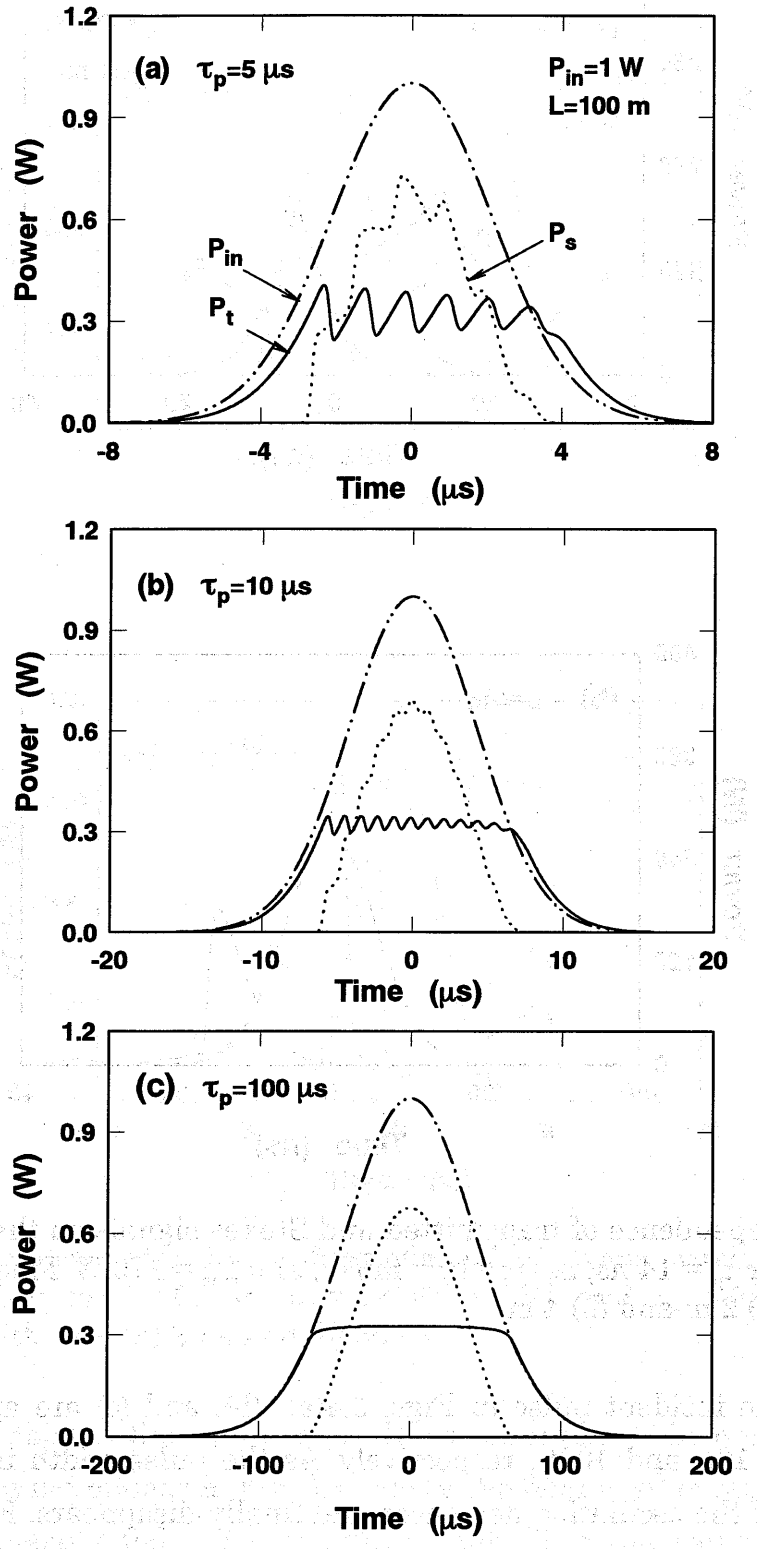

Fig. 5.4. Dependence of transmitted and Stokes signals on the pulse width of the pump pulse for L = 100 m, $n_2 = 1\times10^{-22}$ m^2/V^2, and P_{in} = 1 W. Pulse widths are (a) 5 μs, (b) 10 μs, and (c) 100 μs.

simulation shown in Fig. 5.1, we do not observe the instabilities, even if the input peak power is increased to 200 kW. However, we find that when the nonlinear refractive index n_2 is 1×10^{-21} m^2/V^2, which is an order of magnitude larger than that of a conventional fused-silica fiber, SBS instability appears. It should be noted that such instability only occurs when the self- and cross-phase modulations are included in the coupled-amplitude equations.

Figure 5.5 shows the temporal variation of the transmitted pulses for four values of the input peak power when an input pulse is incident to an optical fiber with $n_2 = 1\times10^{-21}$ m^2/V^2, L = 0.5 m, and τ_p = 30 ns. We obtain a smooth transmitted pulse for an input peak power of 400 W. As the input power is increased, an oscillatory structure in the transmitted signal appears, as shown in Fig. 5.5(b). The oscillation is rapidly relaxed. As the input peak

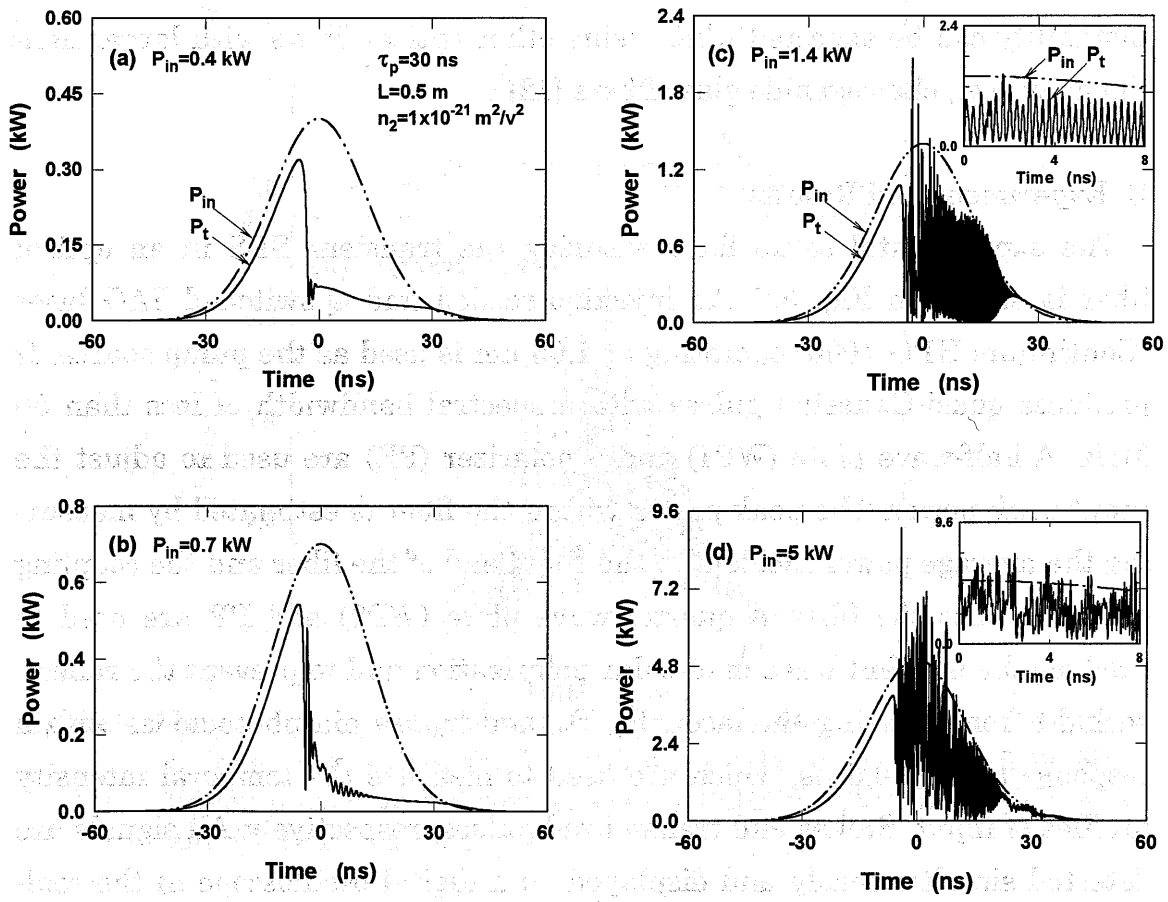

Fig. 5.5. Dependence of transmitted signals on the pump power for $n_2 = 1\times10^{-21}$ m^2/V^2, L = 0.5 m, and τ_p = 30 ns. Input peak powers are (a) 0.4 kW, (b) 0.7 kW, (c) 1.4 kW, and (d) 5.0 kW. The insets are enlarged profiles.

power is further increased, the period becomes smaller and the oscillation becomes quasi-periodic, as shown in the inset of Fig. 5.5(c). We also note that both the amplitude and the oscillatory range of the oscillation become larger. As the input power is increased to 5 kW, the oscillation becomes complex and random (see Fig. 5.5(d)). In order to examine the effect of the nonlinear refractive index n_2 on SBS, we investigate the instability by changing the magnitude of n_2. Figure 5.6 shows a numerical example where the fiber length is assumed to be 100 m and the input power is fixed at 5 W. We see a relaxation oscillation in the transmitted signal for $n_2 = 1\times10^{-22}$ and 1×10^{-21} m^2/V^2. For larger values of n_2, the oscillation becomes complex and eventually irregular, as shown in Fig. 5.6(c). We conclude that the instability of SBS depends strongly on the magnitude of the nonlinear refractive index of the fiber. It is difficult to observe the SBS instability in an experiment using a conventional short silica fiber. However, experimental observation of the SBS instability can be expected when using other optical fibers with larger nonlinearity, e.g., chalcogenide glass fibers [12].

C. Experiment and Results

The experimental setup for measuring the transient SBS in an optical fiber is shown in Fig. 5.7. An injection-seeded and Q-switched YAG laser (Continuum HPO-1000) operating at 1.06 μm is used as the pump source. It produces quasi-Gaussian pulses with a spectral bandwidth of less than 80 MHz. A half-wave plate (WP1) and a polarizer (PR) are used to adjust the input peak power. The peak power within the fiber is estimated by measuring the average power incident to the frond end of the fiber and the coupling efficiency into the fiber. A quarter-wave plate (WP2) and PR are used to produce the incident wave in circular polarization and to prevent the reflected light from entering the laser. D_1, D_2, and D_3 are pin photodiodes with a response time of 0.5 ns, which are used to measure the temporal intensity profiles of input, Stokes and transmitted pulses, respectively. All signals are detected simultaneously and displayed on a digital oscilloscope in the real-time mode. In this experiment, there is zero electronic delay among these pulses. All other parameters used in the experiment are listed in Table 5.2. Figure 5.8 shows the measured temporal profiles of incident, transmitted

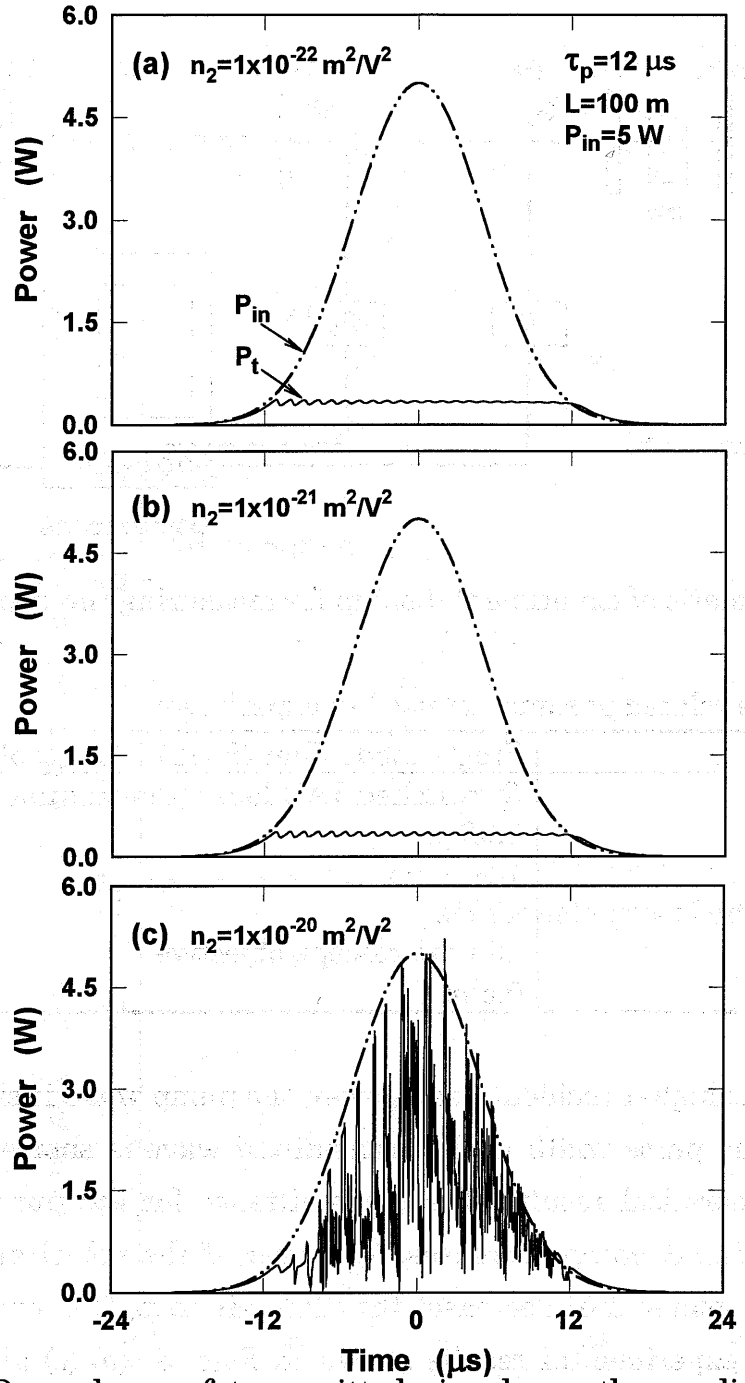

Fig. 5.6. Dependence of transmitted signals on the nonlinear refractive indexes of the fiber for L = 100 m, τ_p = 12 μs, and P_{in} = 5 W. Nonlinear refractive indexes n_2 are (a) 1×10^{-22} m^2/V^2, (b) 1×10^{-21} m^2/V^2 and (c) 1×10^{-20} m^2/V^2.

and Stokes pulses for τ_p=14 ns and the incident peak power P_{in} = 0.5, 1.0, and 4.0 kW. It is found that SBS occurs when the incident peak power is higher than 0.5 kW, which is several times higher than the numerical results shown

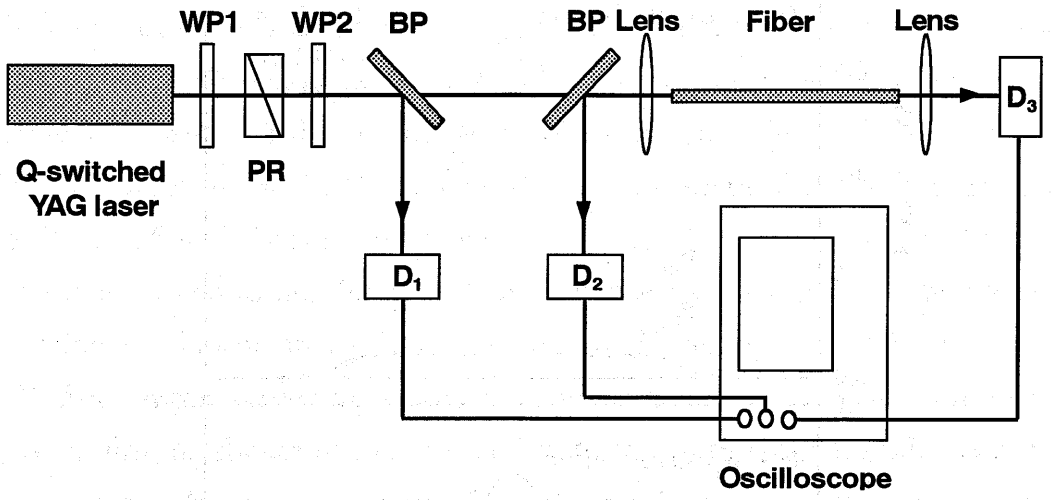

Fig. 5.7. Schematic of experimental setup for measuring the transient SBS.

Table 5.2. The related parameters used in experiment.

Type of fiber	Single-mode fiber (F-SY) (see table 3.2)
Light source	Q-switched YAG laser (Continuum HPO-1000)
Wavelength λ.	1.06 μm
Pulse width	14~50 ns
Frequency of the laser pulse	10 Hz
Focal lens	10×microscope objective
Fiber length L	0.5 m

in Fig. 5.1(a). At higher incident peak power, the pump wave is significantly depleted and the pulse width of the transmitted wave is shortened, as expected from theoretical results. The transmittance for the pump light decreases as the input power increases. Moreover, if the polarization scrambling effect is considered (it decreases the SBS gain to $g_{B0}/2$ in our case), it is found that the experimental results shown in Figs. 5.8(a)-(c) almost agree with the numerical results shown in Figs. 5.1(b)-(d). Figure 5.9 shows the temporal profiles of incident, transmitted and Stokes pulses for τ_p = 50 ns and the incident peak power P_{in}=200 and 360 W. Pulse compression for the transmitted signal becomes poor, as shown in Fig. 5.9(b). Compared with Fig. 5.8, it is found that the gain obtained in the produced Stokes signal becomes larger, as expected from the numerical results. Here, it should be noted that

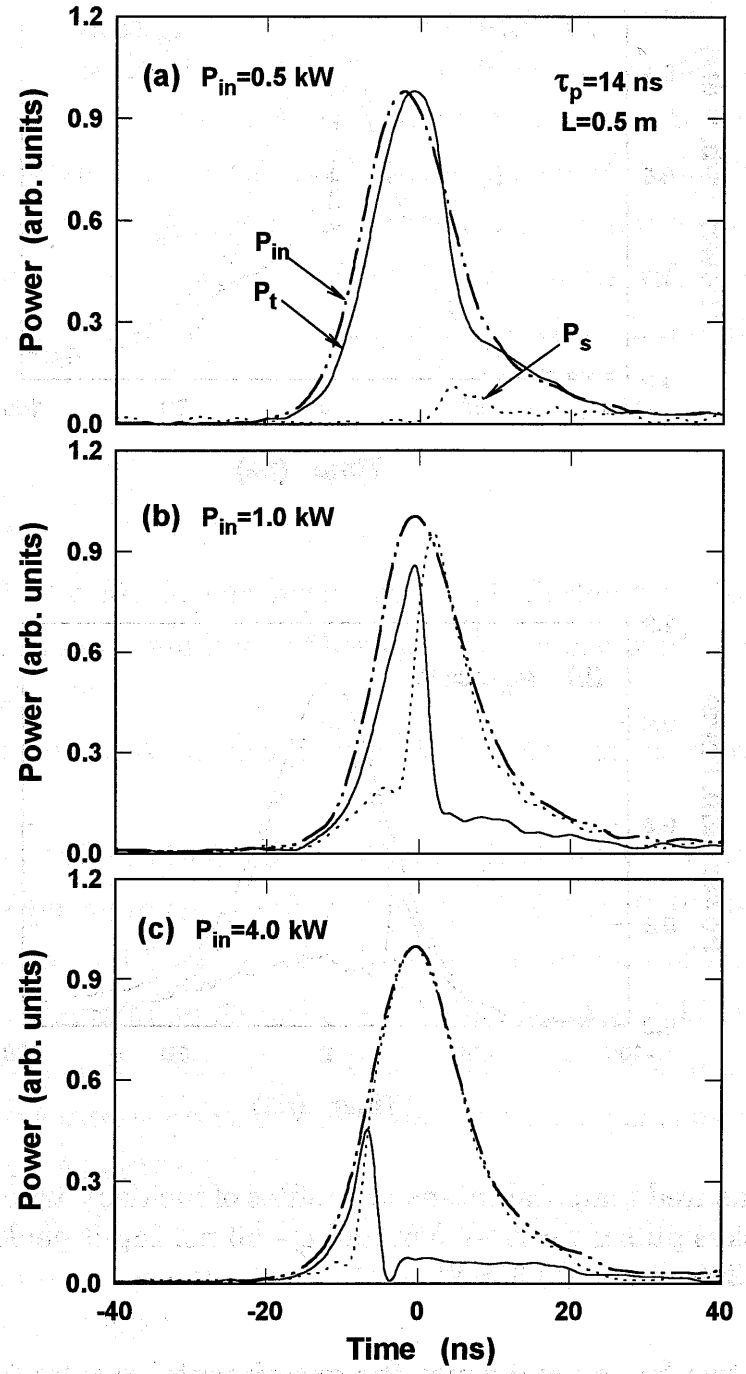

Fig. 5.8. Measured temporal intensity profiles of incident, transmitted and Stokes pulses for L = 0.5 m and τ_p = 14 ns. Input peak powers are (a) 0.5 k W, (b) 1.0 kW, and (c) 4.0 kW.

the optical elements WP2 and PR used in our experiment cannot avoid the feedback of the Stokes waves from the laser-cavity mirror back into the fiber. Moreover, optical reflection at the fiber ends was neglected in our numerical

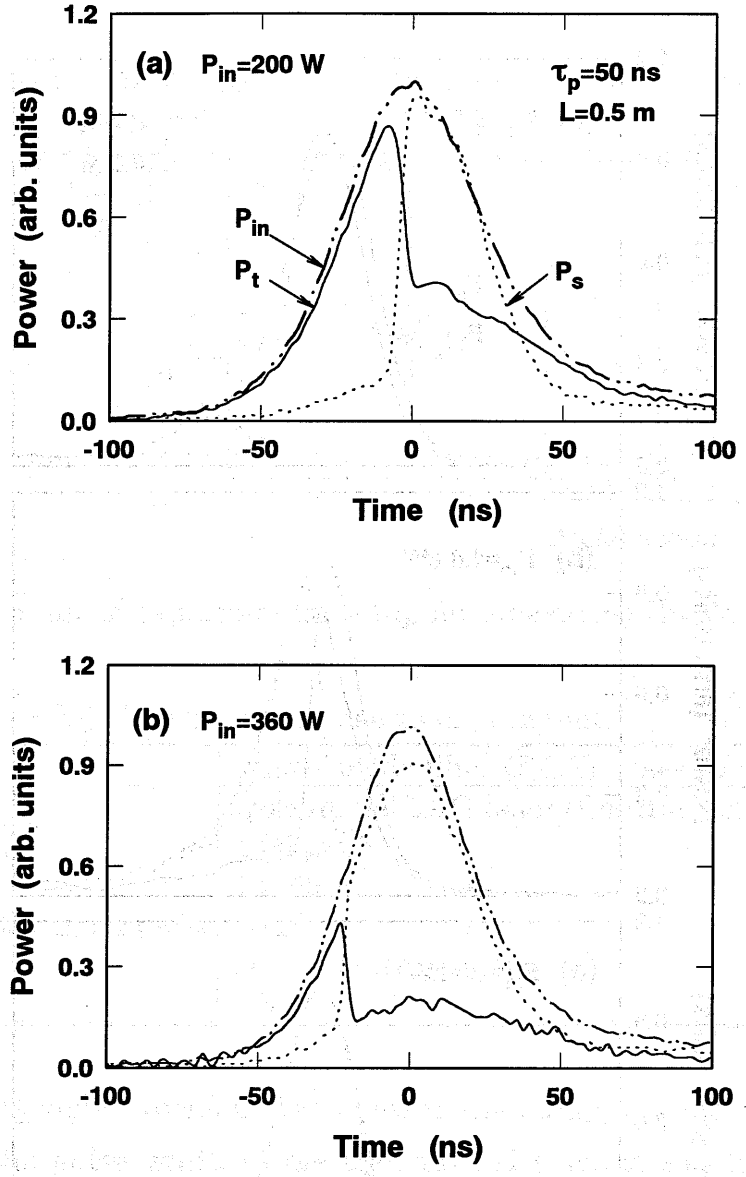

Fig. 5.9. Measured temporal intensity profiles of incident, transmitted and Stokes pulses for L =0.5 m and τ_p =50 ns. Input peak powers are (a) 200 W and (b) 360 W.

model. These two factors will cause the experimental results to be different from the numerical ones, particularly when the pulse width of the incident pulse is greater than 50 ns.

5.4 Conclusions

The transient SBS in a single-mode fiber was theoretically and experimentally investigated under Gaussian pulse irradiation. Theoretical and experi-

mental results revealed that SBS can occur even in the nanosecond region. It was determined that the steady state of SBS can be obtained when the pulse width of the incident light is greater than 100-fold that of the round-trip time within the fiber. Following the process of the transient SBS, pulse narrowing for the transmitted pulse is observed. Moreover, we numerically demonstrated that the instability of SBS is closely connected with the magnitude of the nonlinear refractive index. SBS instability can occur when the nonlinear refractive index is one order of magnitude larger than that of the fused-silica fiber.

References

[1] R. M. Shelby, M. D. Levenson, and S. H. Perlmutter, "Bistability and other effects in a nonlinear fiber-optic ring resonator," J. Opt. Soc. Am. B 5 (1988) 347.

[2] G. P. Agrawal, *Nonlinear Fiber Optics* (Academic, New York, 1995) Chap. 9.

[3] G. Grosso and A. Höök, "Generation of short pulses by stimulated Brillouin scattering in optical fibers," J. Opt. Soc. Am. B 10 (1993) 946.

[4] A. L. Gaeta and R. W. Boyd, "Stochastic dynamics of stimulated Brillouin scattering in an optical fiber," Phys. Rev. A 44 (1991) 3205.

[5] D. J. Kaup, A. Reiman, and A. Bers, "Space-time evolution of nonlinear three-wave interactions. I. Interaction in a homogeneous medium," Rev. Mod. Phys. 51 (1979) 275.

[6] R. G. Smith, "Optical power handling capacity of low loss optical fibers as determined by stimulated Raman and Brillouin scattering," Appl. Opt. 11 (1972) 2489.

[7] L. Chen and X. Bao, "Analytical and numerical solutions for steady state stimulated Brillouin scattering in a single-mode fiber," Opt. Commun. 152 (1998) 65.

[8] E. P. Ippen and R. H. Stolen, "Stimulated Brillouin scattering in optical fibers," Appl. Phys. Lett. 21 (1972) 539.

[9] I. Bar-Joseph, A. A. Friesem, E. Lichtman, and R. G. Waarts, "Steady and relaxation oscillations of stimulated Brillouin scattering in single-

mode optical fibers," J. Opt. Soc. Am. B 2 (1985) 1606.

[10] W. Lu, A. Johnstone, and R. G. Harrison, "Deterministic dynamics of stimulated scattering phenomena with external feedback," Phys. Rev. A 46 (1992) 4114.

[11] Y. Imai and H. Aso, "Chaos in fiber-optic stimulated Brillouin scattering dependent on pump power, nonlinear refractive index, feedback power, and fiber length," Opt. Rev. 4 (1997) 636.

[12] M. Asobe, T. Kanamori, and K. Kubodera, "Applications of highly nonlinear Chalcogenide glass fibers in ultrafast all-optical switches," IEEE J. Quantum Electron. 29 (1993) 2325.

Chapter 6. Stimulated Brillouin Scattering in a Fiber Ring Resonator

6.1 Introduction

In this chapter, our first aim is to investigate the transient SBS in a short fiber resonator with high finesse and determine the factors which may give rise to an instability in the output Stokes. Although the instability of SBS in a long fiber with or without a weak external feedback has been widely studied so far, the instability of SBS, especially the self-pulsing phenomenon in a short fiber ring resonator has not been comprehensively studied to date. We investigate the instability of SBS by solving the time-dependent coupled-amplitude equations numerically. Second, we discuss the dynamic behavior of SBS in a time region which is nearly the same order of magnitude as the phonon lifetime. We theoretically and experimentally investigate the transient SBS in a fiber ring resonator with 14 ns pulses from a single-mode YAG laser. Finally, in order to determine whether the optical bistability could be experimental observed in a fiber ring resonator, we moreover investigate the transient interplay of the Kerr effect with the SBS gain effect. Both the Kerr effect and the linear phase detuning of the fiber cavity have been considered in our theoretical model. This information is necessary for us to develop optical bistable devices in a high-finesse fiber ring resonator [1-3].

6.2 Theory

Figure 6.1 shows a schematic diagram of a fiber ring resonator, which con-

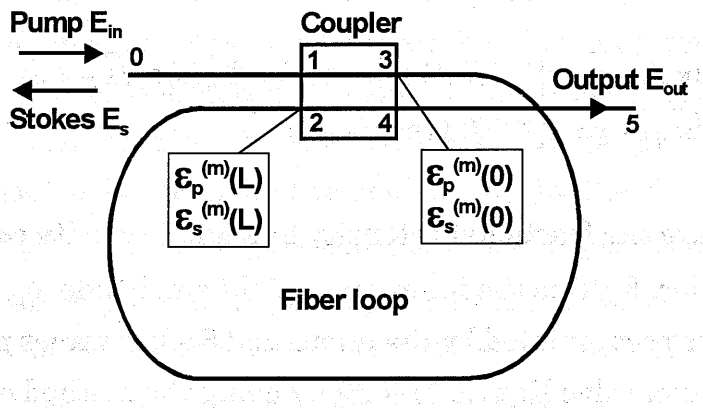

Fig. 6.1. Schematic of a fiber ring resonator with a directional coupler.

sists of a fiber ring of length L and a fiber directional coupler. The coupled-amplitude equations for the slowly-varying complex amplitudes of the pump, Stokes and acoustic waves is described as follows [4]:

$$\frac{\partial \varepsilon_p^{(m)}(z,t)}{\partial t}+\frac{c}{n_0}\frac{\partial \varepsilon_p^{(m)}(z,t)}{\partial z}=-\frac{\alpha c}{2n_0}\varepsilon_p^{(m)}(z,t)-jg_1\cdot\varepsilon_s^{(m)}(z,t)\cdot\rho^{(m)}(z,t) \\ -j\frac{n_2\omega_p}{n_0}\left[\left|\varepsilon_p^{(m)}(z,t)\right|^2+2\left|\varepsilon_s^{(m)}(z,t)\right|^2\right]\varepsilon_p^{(m)}(z,t), \tag{6.1}$$

$$\frac{\partial \varepsilon_s^{(m)}(z,t)}{\partial t}-\frac{c}{n_0}\frac{\partial \varepsilon_s^{(m)}(z,t)}{\partial z}=-\frac{\alpha c}{2n_0}\varepsilon_s^{(m)}(z,t)-jg_1\cdot\varepsilon_p^{(m)}(z,t)\cdot\rho^{(m)*}(z,t) \\ -j\frac{n_2\omega_s}{n_0}\left[2\left|\varepsilon_p^{(m)}(z,t)\right|^2+\left|\varepsilon_s^{(m)}(z,t)\right|^2\right]\varepsilon_s^{(m)}(z,t), \tag{6.2}$$

$$\frac{\partial \rho^{(m)}(z,t)}{\partial t}+v_A\frac{\partial \rho^{(m)}(z,t)}{\partial z}=-\Gamma_A\rho^{(m)}(z,t)-jg_2\varepsilon_p^{(m)}(z,t)\cdot\varepsilon_s^{(m)*}(z,t)+f(z,t), \tag{6.3}$$

where ε_p, ε_s, and ρ are the complex amplitudes of the incident pump field, the backward-propagating Stokes field, and the acoustic field, respectively. ω_p and ω_s are the angular frequencies of pump and Stokes waves, respectively. The superscript (m) refers to the number of pump and Stokes circulation around the fiber loop. Other parameters remain the same as the ones of chapter 5. As shown in Fig. 6.1, the pump wave propagates from z= 0 to z = L and the Stokes wave travels in the opposite direction (from z= L to z = 0). The boundary conditions for the pump wave and Stokes wave are given as follows:

$$\varepsilon_p^{(m)}(0,t)=-j\sqrt{\kappa}\sqrt{1-\gamma}\times\varepsilon_p^{(m-1)}(L,t)\exp(-j\phi_p)+E_{in}(t)\times\sqrt{1-\kappa}\sqrt{1-\gamma}, \tag{6.4}$$

$$\varepsilon_s^{(m)}(L,t)=-j\sqrt{\kappa}\sqrt{1-\gamma}\times\varepsilon_s^{(m-1)}(0,t)\exp(-j\phi_s), \tag{6.5}$$

where γ and κ are the fractional intensity loss and intensity coupling coefficient of the coupler. $E_{in}(t)$ is the input pump field amplitude. ϕ_p and ϕ_s are the total linear phase accumulated by the pump and Stokes waves per round trip, respectively. We can solve Eqs. (6.1)-(6.3) by using the method of characteristics under the following initial condition:

$$\varepsilon_p^{(1)}(0,t) = \sqrt{1-\kappa}\sqrt{1-\gamma} \times E_{in}(t) \qquad 0 \le t \le t_R, \tag{6.6}$$

$$\varepsilon_s^{(1)}(L,t) = 0 \qquad 0 \le t \le t_R, \tag{6.7}$$

where $t_R (= n_0 L/c)$ is the round-trip time through the fiber loop. Once the values of $\varepsilon^{(1)}{}_p(L,t_R)$ and $\varepsilon^{(1)}{}_s(0,t_R)$ are given, using Eqs. (6.6) and (6.7), we can obtain the magnitudes of $\varepsilon^{(2)}{}_p(0,t_R)$ and $\varepsilon^{(2)}{}_s(L,t_R)$, which are used as the initial condition of the second circulation (i.e., $t_R \le t \le 2t_R$). Repeating the above steps for certain times (in our case, we investigate SBS in a time range of 0-$1000t_R$), we can obtain the outputs of pump field E_{out} and Stokes field E_s, which are expressed as:

$$E_{out}(t) = -j\sqrt{\kappa}\sqrt{1-\gamma} \times E_{in}(t) + \varepsilon_p(L,t)\exp(-j\phi_p) \times \sqrt{1-\kappa}\sqrt{1-\gamma}, \tag{6.8}$$

$$E_s(t) = \varepsilon_s(0,t)\exp(-j\phi_s) \times \sqrt{1-\kappa}\sqrt{1-\gamma}. \tag{6.9}$$

Among the most previous papers, the linear phases ϕ_p and ϕ_s are taken as $\phi_p=\phi_s=\phi_0 = k_0 n_0 L = 2M\pi$ (M is an integer). It should be noted that this assumption is not correct, especially when the cavity finesse is high enough. The difference between ϕ_p and ϕ_s is given by

$$\phi_p - \phi_s = \frac{\omega_p - \omega_s}{c} n_0 L = \frac{2\pi\nu_A}{c} n_0 L, \tag{6.10}$$

where ν_A is the frequency of acoustic wave, it is about 16 GHz at a wavelength of 1.06 μm for a silica fiber [5]. One can easily see that the phase difference between ϕ_p and ϕ_s is much larger than the magnitude 2π even if the length of fiber loop is several centimeters. In the absence of fiber nonlinearity, the resonance condition of the ring (see Fig. 6.1) is given by $\phi_0 = k_0 n_0 L = 2M\pi - \pi/2$ and it is convenient to replace ϕ_p by the detuning from resonance $\Delta\phi_p = k_0 n_0 L - 2M\pi$. Figure 6.2 shows the dependence of the ratio of the circulating pump power to the input power P_{ring}/P_{in} on the initial phase detuning $\Delta\phi_p$ for four values of κ, where the generation of SBS is neglected. Since the circulating pump power depends strongly on the phase detuning $\Delta\phi_p$ as shown in Fig. 6.2, the effect of the initial phase detuning on SBS must

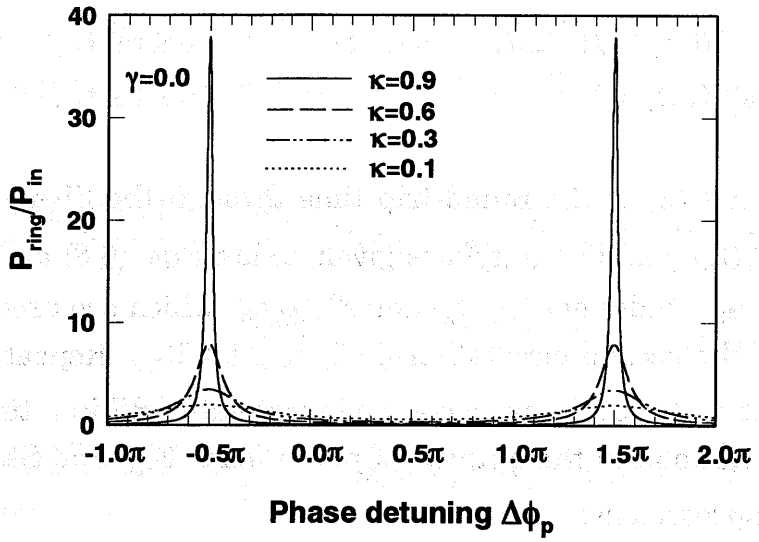

Fig. 6.2. Steady-state power ratio P_{ring}/P_{in} of the linear ring resonator with $\gamma = 0$ as a function of the initial phase detuning $\Delta\phi_p$ for four values of the coupling coefficient κ.

be considered.

6.3 Instability of Stimulated Brillouin Scattering in a Fiber Ring Resonator

In this section, we investigate SBS instability in a fiber ring resonator. The incident signal is assumed to be a step pulse. Other parameters used here are shown in Table 5.1. For simplicity, the fractional coupler intensity loss is assumed to be zero and the ring length ring is assumed to be 2 m.

First, we investigate the dependence of SBS instability on the incident peak power. Figure 6.3 shows the variation of the output Stokes power as a function of time for three values of input peak power, where the initial phase detuning is assumed to be zero (i.e. $\Delta\phi_p = 0$), the coupling coefficient of the coupler κ is fixed at 0.5, and the output Stokes power is represented by P_s. At a low pump power, such as 20 W shown in Fig. 6.3(a), it is found that the output Stokes signal is relaxed to its steady state after the time of $\sim 20t_R$ and the period of the relaxation oscillation is approximately equal to t_R. When the input peak power is increased to 100 W, the Stokes signal is also relaxed to its steady state, but the relaxation oscillation becomes irregular (Fig. 6.3(b)). As the input peak power is further increased to 600 W (Fig. 6.3(c)), it is found

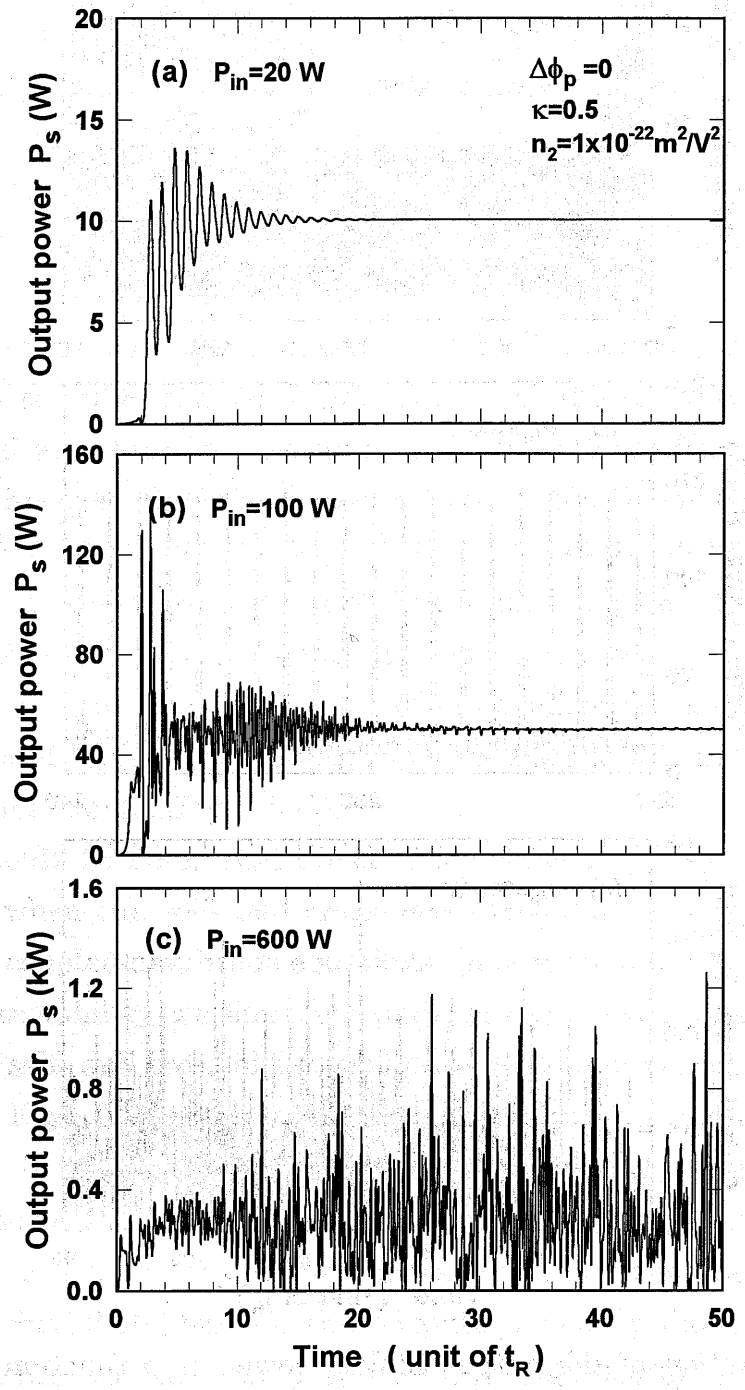

Fig. 6.3. Variation of the output Stokes power as a function of time for $\Delta\phi_p = 0$, L = 2 m, and $\kappa = 0.5$ at different input peak powers P_{in}: (a) 20 W, (b) 100 W, and (c) 600 W.

that the steady state of SBS cannot be obtained, the Stokes signal becomes complex and eventually chaotic. Moreover, as the initial phase detuning $\Delta\phi_p$

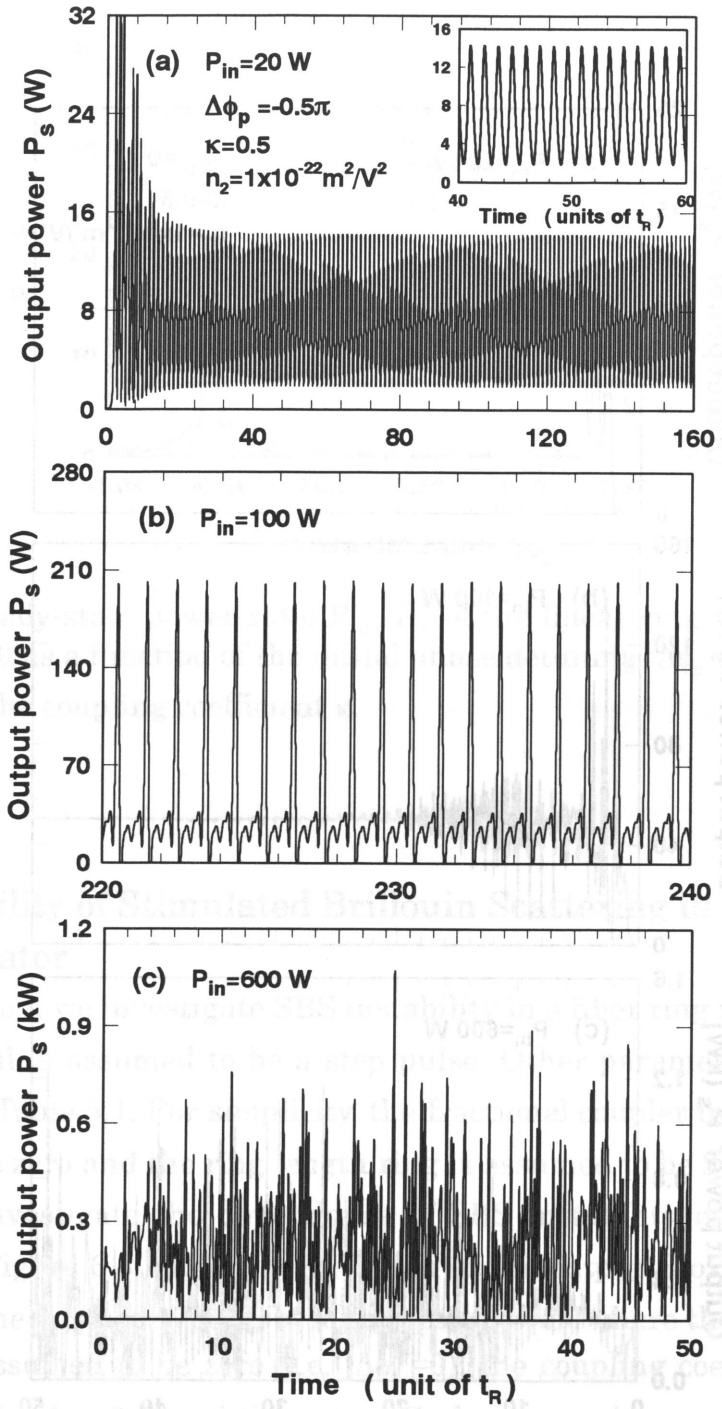

Fig. 6.4. Variation of the output Stokes power as a function of time for $\Delta\phi_p = -0.5\pi$, L = 2 m, and $\kappa = 0.5$ at different input peak powers P_{in}: (a) 20 W, (b) 100 W, and (c) 600 W.

becomes -0.5π (i.e., the circulating pump wave is resonant in the fiber ring), the variation of the output Stokes power as a function of time is considerably changed, as shown in Fig. 6.4. It is found that the Stokes signal is not stable

for all the three values of the input powers. At a pump power of 20 W (Fig. 6.4(a)), the output Stokes signal is first relaxed in a short-time range of $0\sim40t_R$ and then becomes periodic oscillation. The period of the oscillation is approximately equal to t_R as shown in the inset of Fig. 6.4(a). When the input peak power is increased to 100 W, the oscillation becomes a sustained pulsation consisting of a steady train of short pulses (Fig. 6.4(b)). As the input peak power is further increased to 600 W, The output Stokes signal becomes complex and eventually chaotic (Fig. 6.4(c)).

Next, we investigate the dependence of SBS instability on the coupling coefficient of the fiber coupler. Figure 6.5 shows the variation of the output Stokes signal as a function of time for the coupling coefficients κ=0.3, 0.5, and 0.7. In this case, the input power is fixed at 160 W and the initial phase detuning $\Delta\phi_p$ is assumed to be -0.5π. It is found that the output Stokes signal is relaxed to its steady state for κ=0.3 in a time range of $\sim20t_R$ as shown in Fig. 6.5(a). As the coupling coefficient is increased, we obtain a stationary oscillation consisting of a steady train of short pulses for κ=0.5 (Fig. 6.5(b)). When the coupling coefficient is further increased to 0.7, the output Stokes signal becomes chaotic (Fig. 6.5(c)).

Here it should be noted that the chaotic behavior of SBS described above takes place when the self- and cross-phase modulations are taken into account in the coupled-amplitude equations. In order to make sure of the origin of the SBS instability, we moreover perform our calculations by neglecting the effect of self- and cross-phase modulations. The numerical results corresponding to Figs. 6.4(a), (b), and (c) are shown in Figs. 6.6(a), (b), and (c), respectively. It is found that the instability including periodic and chaotic behaviors shown in Figs. 6.4(b) and (c) does not appear. There only exists a relaxation oscillation in the output Stokes signal in a time range of $20\sim50t_R$ as shown in Figs. 6.6(b) and (c). These results obviously show that the physical origin of the SBS instability appeared in Figs. 6.4(b) and (c) is mainly attributed to the nonlinear refraction. Contrary to the above results, the periodic behavior shown in Fig. 6.4(a) also occurs even if the Kerr effect has been neglected, as shown in Fig. 6.6(a).

To gain more information about the SBS instability, we also evaluate the dynamics of the output Stokes signal in the pump power and the coupling

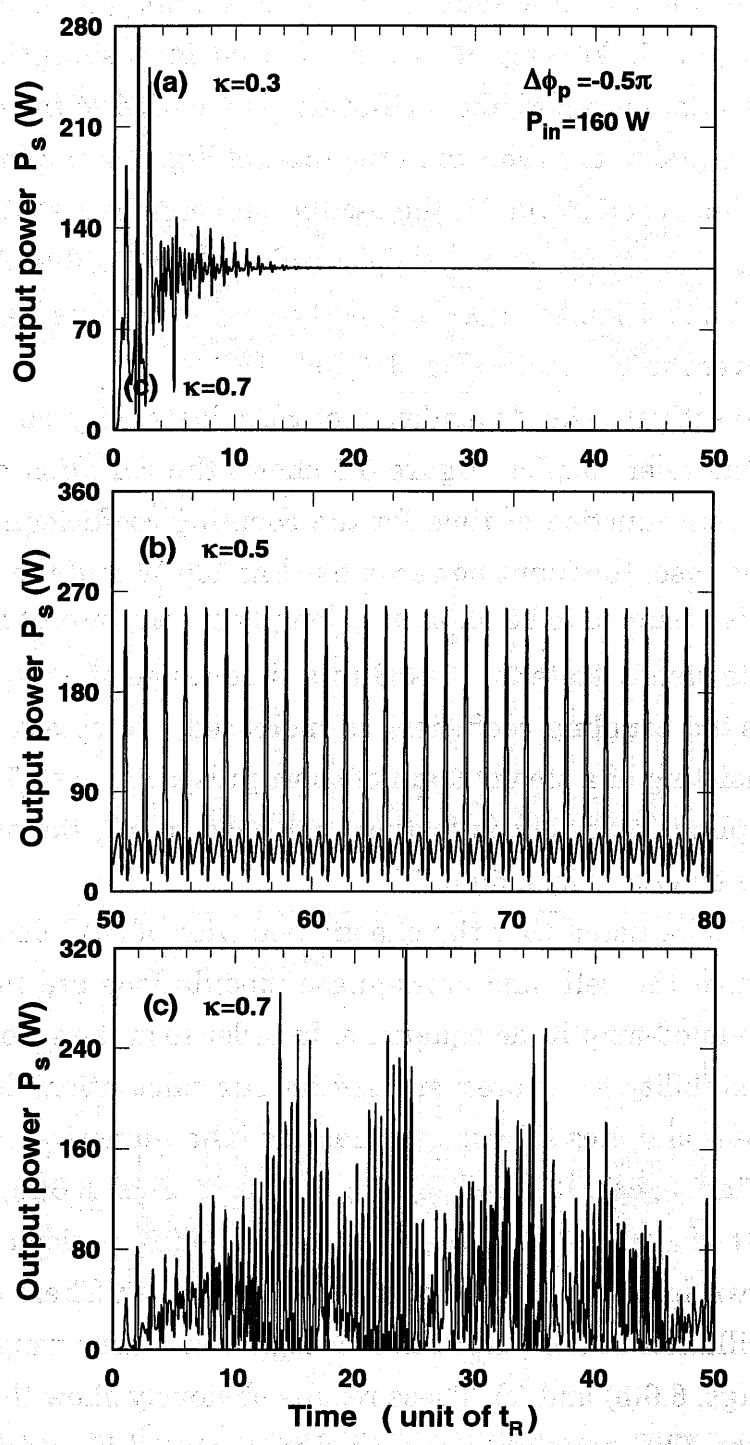

Fig. 6.5. Variation of the output Stokes power as a function of time for $\Delta\phi_p$ = -0.5π, L=2 m, and the input peak power P_{in} =160 W at different coupling coefficients κ: (a) 0.3, (b) 0.5, and (c) 0.7.

coefficient domain as shown in Fig. 6.7. Figures 6.7(a), (b), and (c) correspond to the three values of phase detuning 0.5π, 0, and -0.5π, respectively. In these

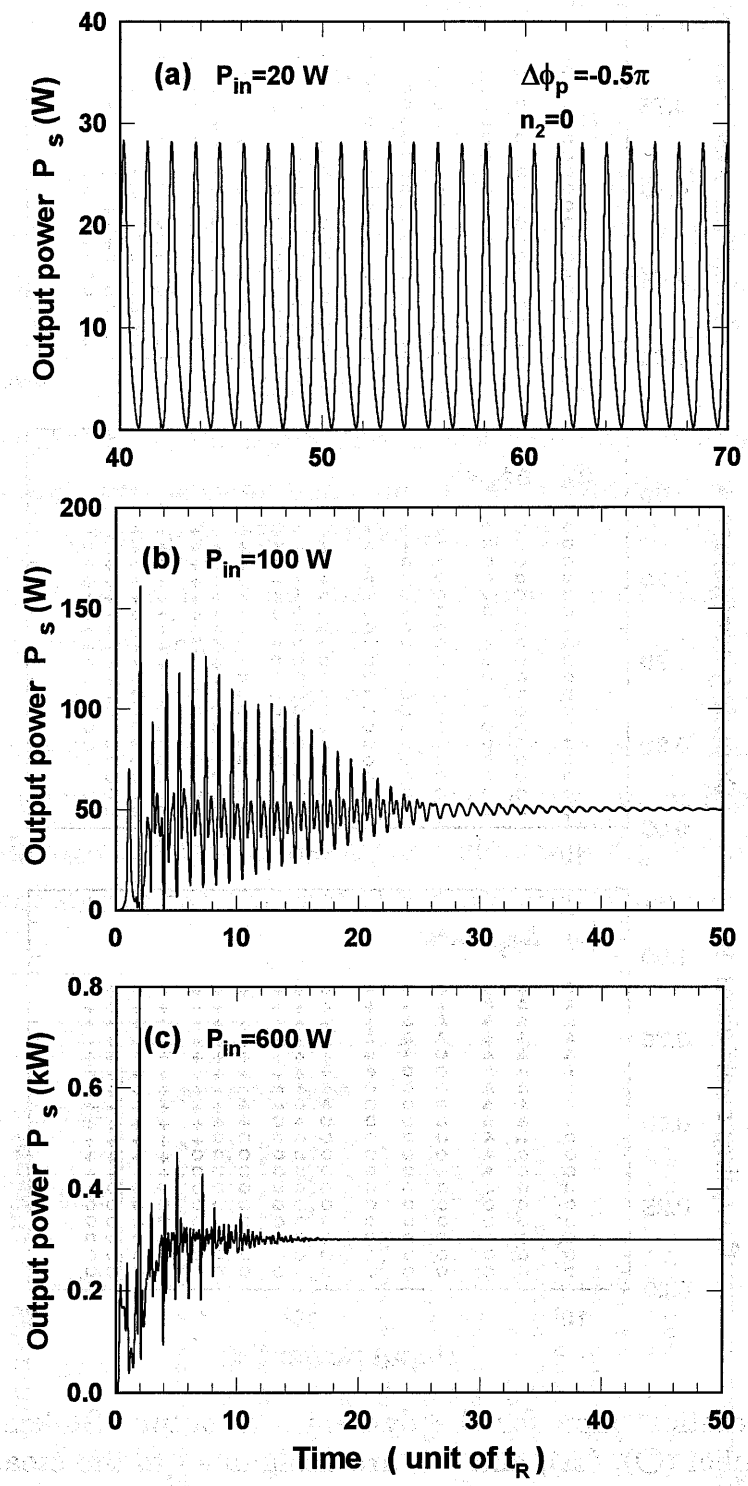

Fig. 6.6. Variation of the output Stokes power as a function of time for $\Delta\phi_p = -0.5\pi$, L = 2 m, $\kappa = 0.5$, and $n_2 = 0$. The input powers are (a) 20 W, (b) 100 W and (c) 600 W.

maps, the input peak power is changed in the range of 10-600 W and the

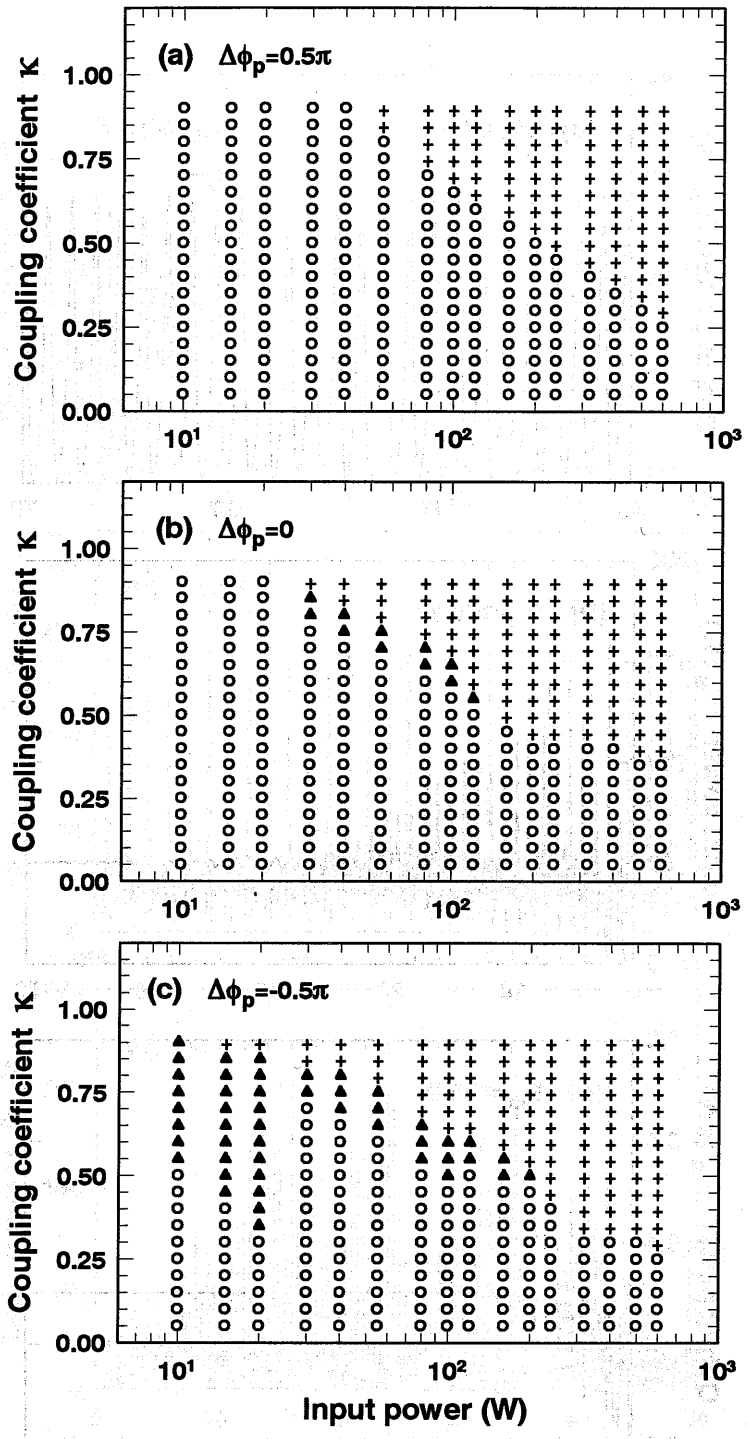

Fig.6.7. Theoretical map for the dynamics of output Stokes signal The symbol (○), (▲), and (+), are designated to the steady, periodic, and chaotic behaviors, respectively. (a) $\Delta\phi_p$ =0.0, (b) $\Delta\phi_p$ =0.5π, and (c) $\Delta\phi_p$ = -0.5π.

coupling coefficient κ is changed in the range of 0.05-0.9. The steady, periodic, and chaotic behaviors of the output Stokes signal are designated by the

symbol (○), (▲), and (+), respectively. For $\Delta\phi_p=0.5\pi$, as shown in Fig. 6.7(a), it is found that a stable Brillouin emission can be obtained at any input pump power when the coupling coefficient κ is smaller than 0.3. This result agrees with that obtained for a low-finesse resonator [6], [7] because a low value of κ in our case corresponds to a low finesse of fiber resonator. It is also found that the chaotic behavior of SBS appears only when the input power is high and the value of the coupling coefficient is large, and that the periodic behavior of SBS has not been observed in these cases. For $\Delta\phi_p=0$, as shown in Fig. 6.7(b), it is found that either the chaotic or the periodic behavior of the output Stokes signal occurs when the value of the coupling coefficient κ is large enough. However, the periodic behavior of the output Stokes signal appears only in a small region of P_{in}=30~120 W and κ=0.5~0.85. For $\Delta\phi_p=-0.5\pi$, as shown in Fig. 6.7(c), it is found that the region where the SBS instability, especially the periodic behavior of SBS occurs becomes larger than that of Fig. 6.7(b). The periodic behavior of the output Stokes signal generally appears at a low input power and Fig. 6.4(a) is a typical example. When the coupling coefficient is increased, the periodic behavior can occur at high input power but in a small region. A typical example is shown in Fig. 6.5(b). Moreover, in order to make sure of the origin of SBS instability shown in Fig. 6.7(c), we

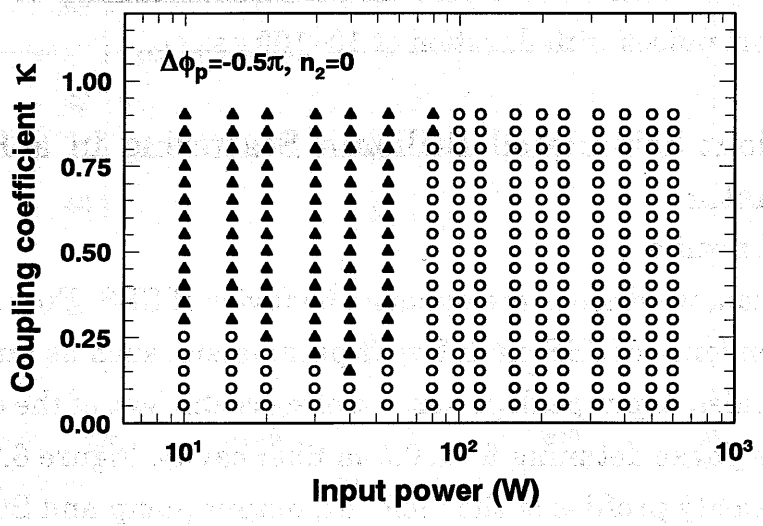

Fig. 6.8. Theoretical map for the dynamics of output Stokes signal, where the Kerr effect is neglected (i.e., $n_2=0$) and the initial phase detuning of the cavity is -0.5π.

also perform the calculations by neglecting the Kerr effect. Figure 6.8 shows the result for $\Delta\phi_p = -0.5\pi$. Compared with Fig. 6.7(c), it is found that the chaotic state disappears for any input power. Moreover, the periodic behaviors at high input power region disappear. These results mean that the enhancement in the high-finesse resonator would make the Kerr effect larger than the Brillouin gain effect and the origin of this SBS instability is mainly attributed to the Kerr effect when the input power is high. From Fig. 6.8, it is found that the periodic behaviors occurs in Fig. 6.7(c) also appears when the input power is less than 55 W and the region where the periodic behavior occurs becomes large. The results make us believe that at a low level of the input power, the Kerr effect becomes comparable with the SBS gain effect and the SBS instability at low input power is attributed to the interplay between these two effects.

In conclusion, we have investigated theoretically transient SBS in a high-finesse fiber ring resonator with a short length. It is found that a Stokes wave in the ring resonator is generally unstable for a high-finesse or high incident power. SBS instability including the self-pulsing and chaotic behaviors depends strongly on the input power, the linear phase detuning of the cavity, and the coupling coefficient of the coupler. Although the instability is very harmful to fiber-based devices such as a Brillouin fiber ring laser and sensors, the self-pulsing phenomenon in the output Stokes signal may be used to form a series of short pulses with duration of 10~100 ps.

6.4 Transient Stimulated Brillouin Scattering in a Fiber Ring Resonator

A. Numerical results

In this section, we discuss the dynamic behavior of SBS. First, we investigate the dependence of SBS on different parameters, such as pulse width of the incident pulse, input peak power, coupling coefficient of the coupler, and the linear the phase detuning for a 0.5-m fiber cavity. Figure 6.9 shows the temporal intensity profiles of the incident, output pump and Stokes pulses for P_{in}=50 W, κ=0.1, γ=0, and the pulse width of incident pulse τ_p = 14, 50, and 200 ns. In this example, the circulating pump wave is assumed to be resonant in the fiber loop (i.e, $\Delta\phi_p$=-0.5π) and the incident, output pump and

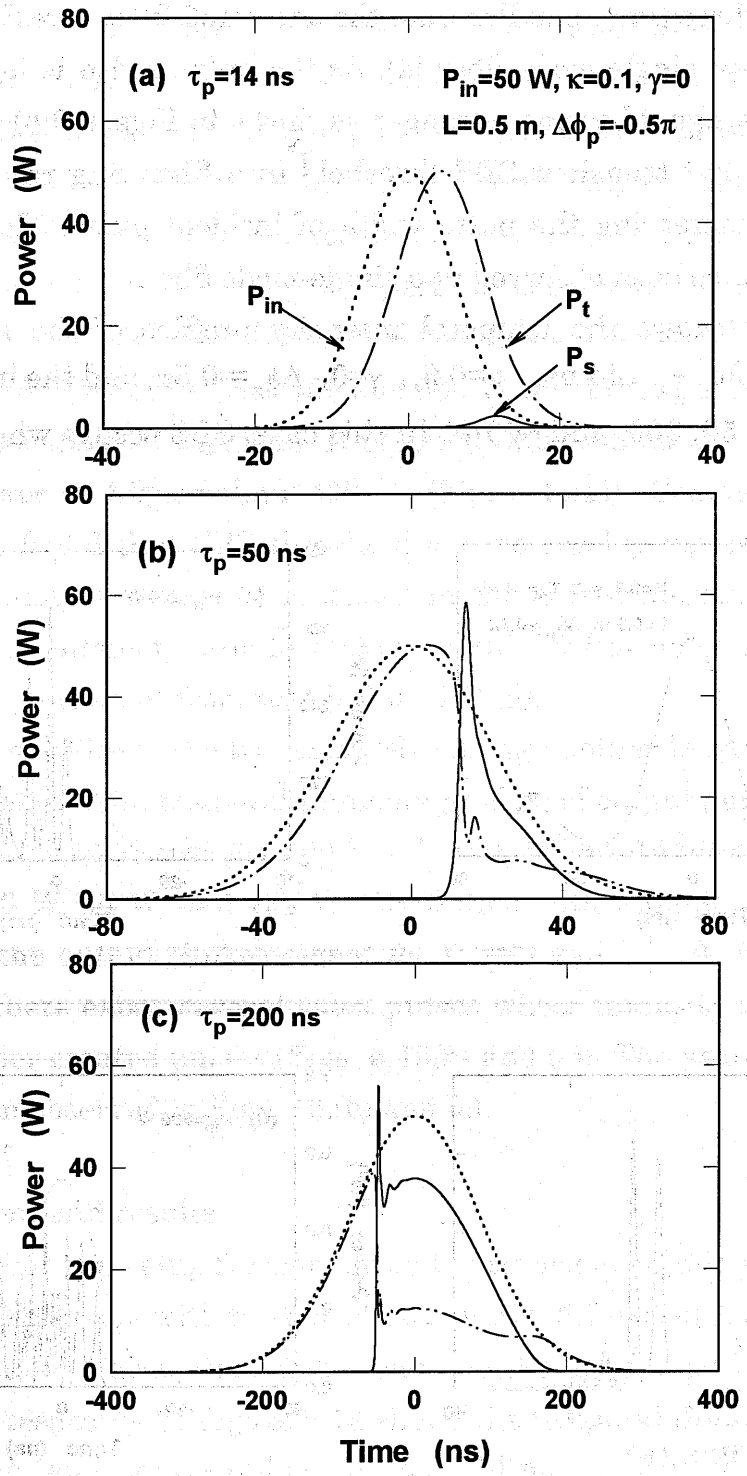

Fig. 6.9. Theoretical results of the temporal intensity profiles of incident, output pump and Stokes pulses for $\Delta\phi_p = -0.5\pi$, L = 0.5 m, $\kappa = 0.1$, $\gamma = 0$, and P_{in}= 50 W. Pulse widths are (a) 14 ns, (b) 50 ns, and (c) 200 ns.

Stokes pulses are represented by P_{in}, P_t, and P_s, respectively. It is found that SBS occurs when the input peak power is larger than 50 W (Fig. 6.9(a)). This value is three times smaller than the one (=150 W) where SBS begins to occur in a 0.5-m single-mode fiber [4]. As the pulse width is increased, the created Stokes signal becomes stronger as shown in Figs. 6.9(b) and (c). This result means that transient SBS threshold in a fiber ring resonator is decreased with increasing the pulse width of incident pulse. The same phenomenon has also been observed in a single-mode fiber.

Figure 6.10 shows the temporal intensity profiles of the incident and Stokes pulses for τ_p = 14 ns, κ=0.6, γ=0, $\Delta\phi_p$=-0.5π, and the incident peak power P_{in}=15, 50, 200, and 800 W. In this case, SBS occurs when the input

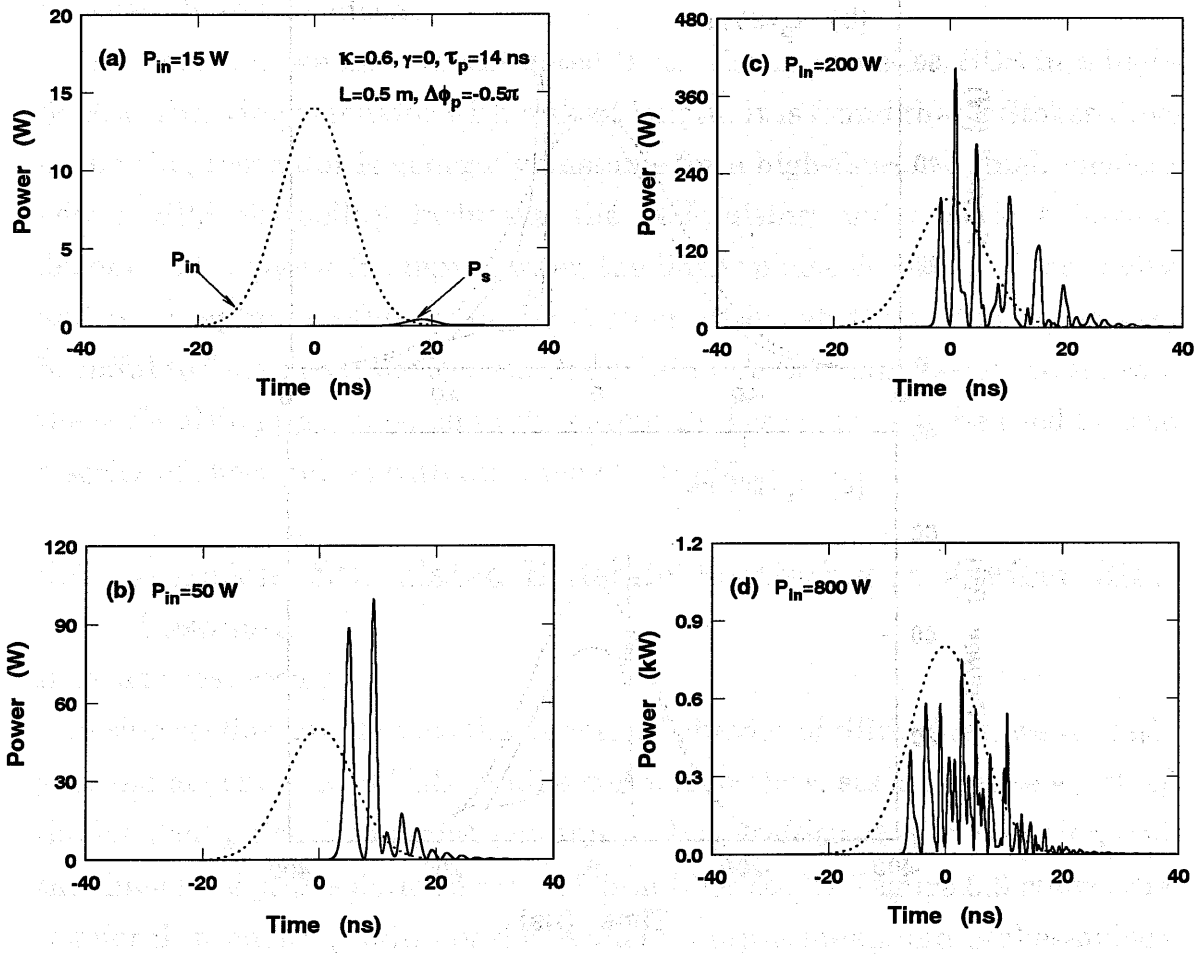

Fig. 6.10. Theoretical results of the temporal intensity profiles of incident and output pump pulses for $\Delta\phi_p$ = -0.5π, L = 0.5 m, κ = 0.6, γ = 0, and τ_P = 14 ns at different input peak powers: (a) 15 W, (b) 50 W, (c) 200, and (d) 800 W.

peak power is larger than 15 W (Fig. 6.10(a)). Compared with Fig. 6.9(a), it is found that SBS threshold decrease with increasing the coupling coefficient κ. As the input peak power is increased, the Stokes signal is converted into a series of short pulses with pulse width much less than that of incident pulse (Figs. 6.10(b) and (c)). The created pulses oscillate strongly and periodically with increasing incident peak power. When the input peak power is increased to 800 W, the created pulses in the Stokes signal become irregular, as shown in Fig. 6.10(d). Here we also perform the same calculations for the initial phase detuning $\Delta\phi_p$=0. A typical example is shown in Fig. 6.11, where the incident peak power P_{in} are 400 and 800 W, and other parameters remain the same with those of Fig. 6.10. It is found that SBS occurs only when the incident power is higher than 400 W (Fig. 6.11(a)). Compared with Fig. 6.10(a), it is found that SBS threshold is considerably increased when the circulating pump wave is not resonant in the cavity. Moreover, it is found that temporal intensity profile of the output Stokes pulse shown in Fig. 6.11(b) is very different from that in Fig. 6.10(d).

Next, we investigate the transient SBS using another length of fiber ring. Figure 6.12 shows the temporal intensity profiles of output pump and Stokes pulses for $L = 2$ m, $\tau_p = 14$ ns, κ=0.1, γ=0, $\Delta\phi_p$=-0.5π, and the incident peak power P_{in}=30 W, 60 W, and 120 W. Oscillation with a burst of short pulses appears in the output Stokes signal for P_{in}=60 and 120 W. Moreover, it is found that there exists several short pulses whose intensity is much larger than the other created pulses (Figs. 6.12(b) and (c)). The same phenomenon has also been observed in Figs. 10.(b) and (c).

B. Experiment and results

The experimental setup for measuring the transient SBS is shown in Fig. 6. 13, which is the same with the one shown in Fig. 5.7 except for the existence of a fiber coupler. Parameters of the fiber and the coupler are listed in Tables 6.1 and 6.2, respectively. Figure 6.14 shows the temporal profiles of incident, output pump, and Stokes pulses for $\tau_P = 14$ ns, $\kappa = 0.1$, and the incident peak power P_{in}=60, 120, and 230 W. It is found that there exists an oscillation in the output Stokes signals for P_{in}=60 W. The period of the relaxation oscillation is nearly equal to the round-trip time through the fiber loop (10

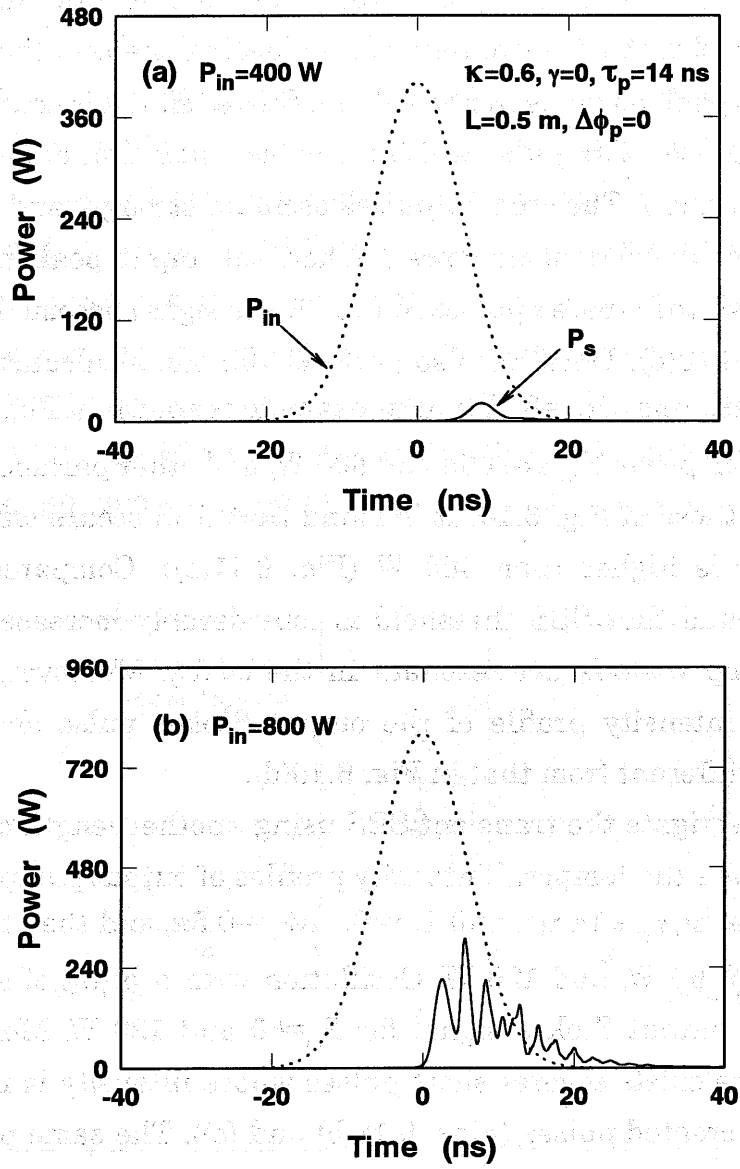

Fig. 6.11. Theoretical results of the temporal intensity profiles of incident and output Stokes pulses for $\Delta\phi_p = 0.0$, $L = 0.5$ m, $\kappa = 0.6$, $\gamma = 0$, and $\tau_P = 14$ ns at different input peak powers: (a) 400 W and (b) 800 W.

ns). As the incident peak power is further increased, the oscillation is divided into a series of pulses (Figs. 6.14(b) and (c)) just as expected from the theoretical predication. Here it is noted that the experimental results for output pump and Stokes pulses shown in Figs. 6.14(a) and (b) are different from the theoretical results shown in Figs. 6.12(b), (c). These inequalities can be attributed to that the coupler and the fiber loss have not be considered in the

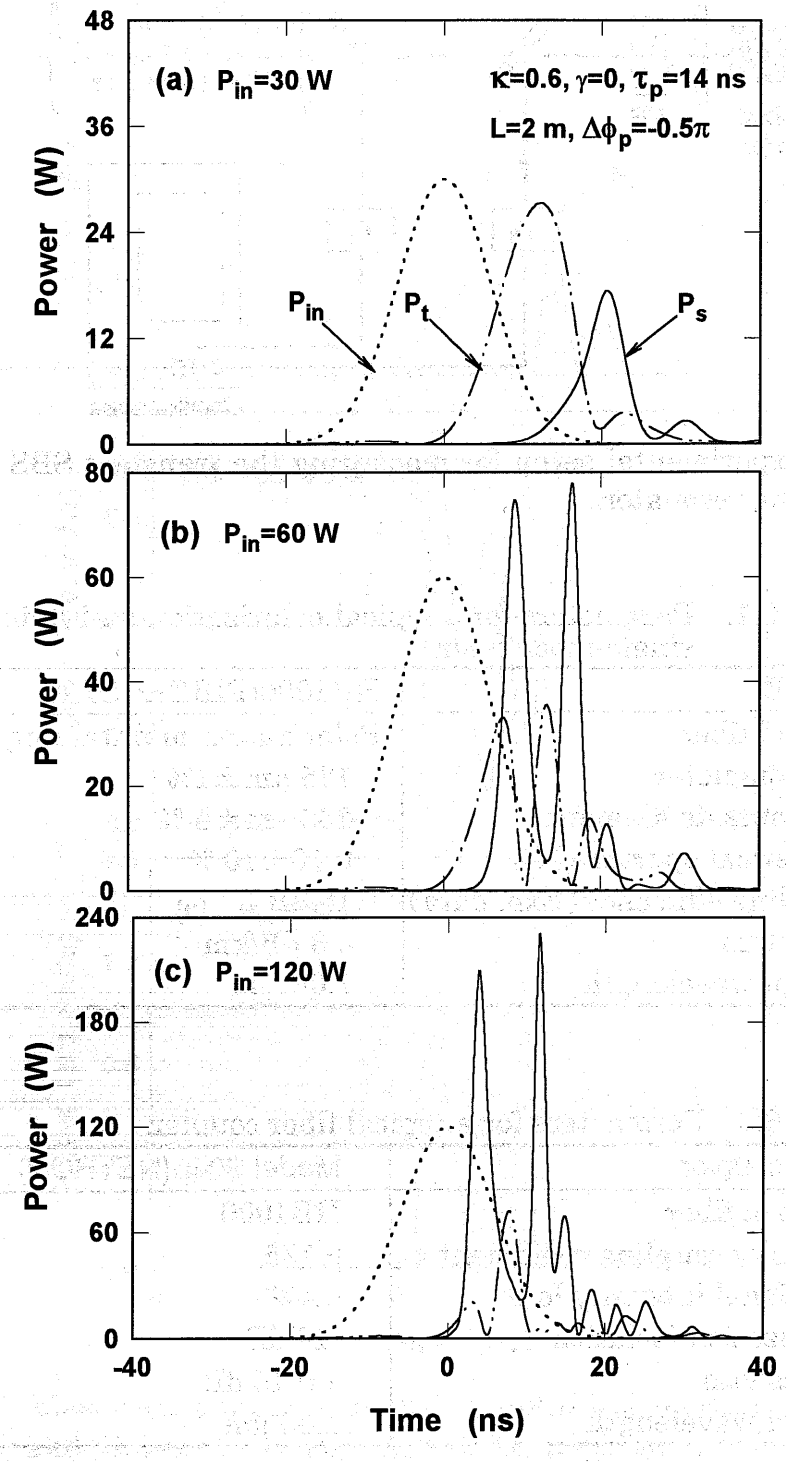

Fig. 6.12. Theoretical results of the temporal intensity profiles of incident, output pump and Stokes pulses for L = 2 m, $\Delta\phi_p$ = -0.5π, κ = 0.1, γ = 0, and τ_P = 14 ns. The input powers are (a) 30 W, (b) 60 W, and (c) 120 W.

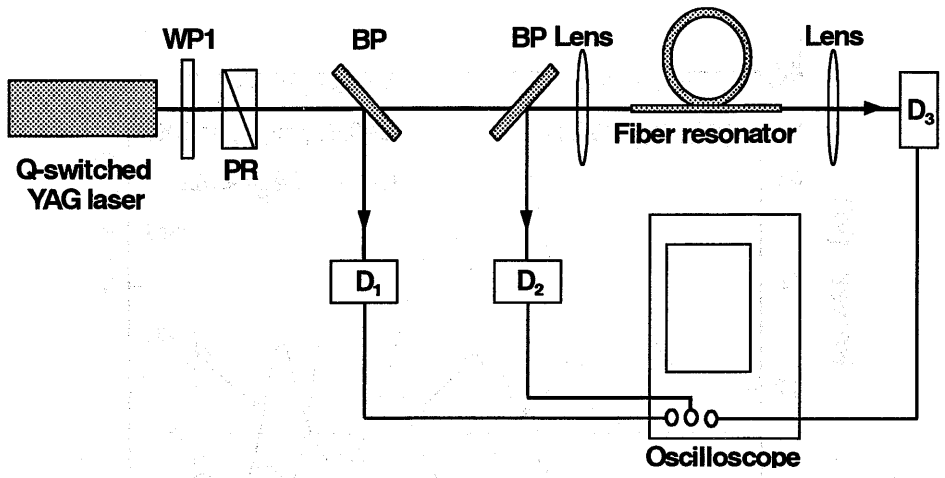

Fig. 6.13. Experimental setup for measuring the transient SBS in a fiber ring resonator.

Table 6.1. Parameters for a typical polarization-maintaining single-mode fiber.

NAME	HB1000(FIBERCORE)
Type of fiber	Polarization-maintaining fiber
Clad diameter	125 μm±1%
Clad outside diameter	245 μm±5 %
Numerical aperture NA	0.16±10 %
Coupling efficiency (Exp. data)	15 dB
Fiber loss	< 3 dB/km
Design wavelength	1.06 □m

Table 6.2 Parameters for a typical fiber coupler.

Fiber coupler	Model 904p(NETRON)
Name of fiber	HB1000
Intensity coupling coefficient κ	0.125
Fractional intensity loss	0.4%
Polarization isolation	-17 dB
Excess loss	< 0.15 dB
Design wavelength	1.06 μm

theoretical model. If the difference between the incident peak power in Figs. 6.12(a)-(c) and the correspondent ones in Figs. 6.14(a)-(c) are not considered, it can be found that the measured temporal profiles of the output pump and Stokes pulses are very similar to the theoretical results. To confirm the above

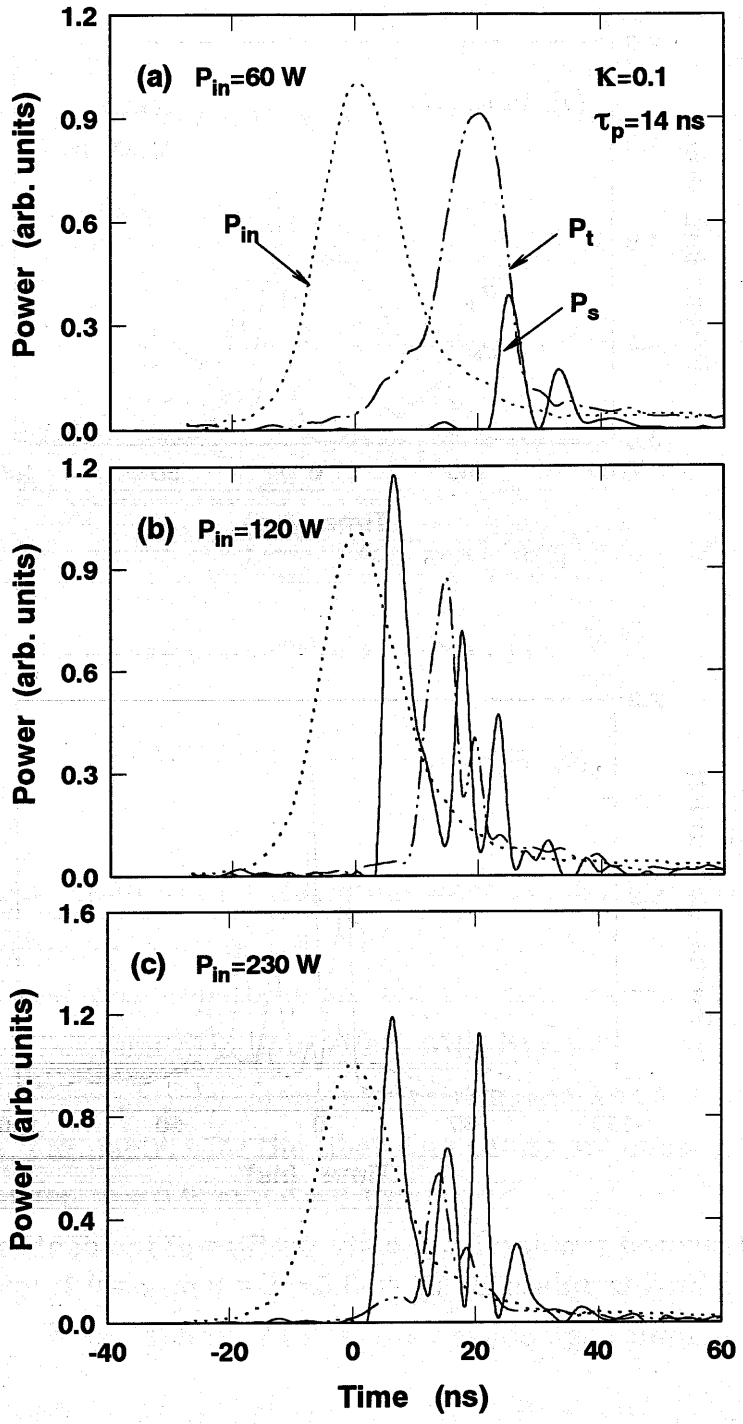

Fig. 6.14. Measured temporal intensity profiles of incident, output pump and Stokes pulses for $\Delta\phi_p = -0.5\pi$, L = 2 m, $\kappa = 0.1$, and $\tau_P = 14$ ns. The input peak powers are (a) 60 W, (b) 120 W, and (c) 230 W.

results, we also investigate the created Stokes signal with increasing pulse with of incident pulse. Figure 6.15 shows the temporal profiles of incident, output pump, and Stokes pulses for $\tau_P = 50$ ns, and incident peak power P_{in}=

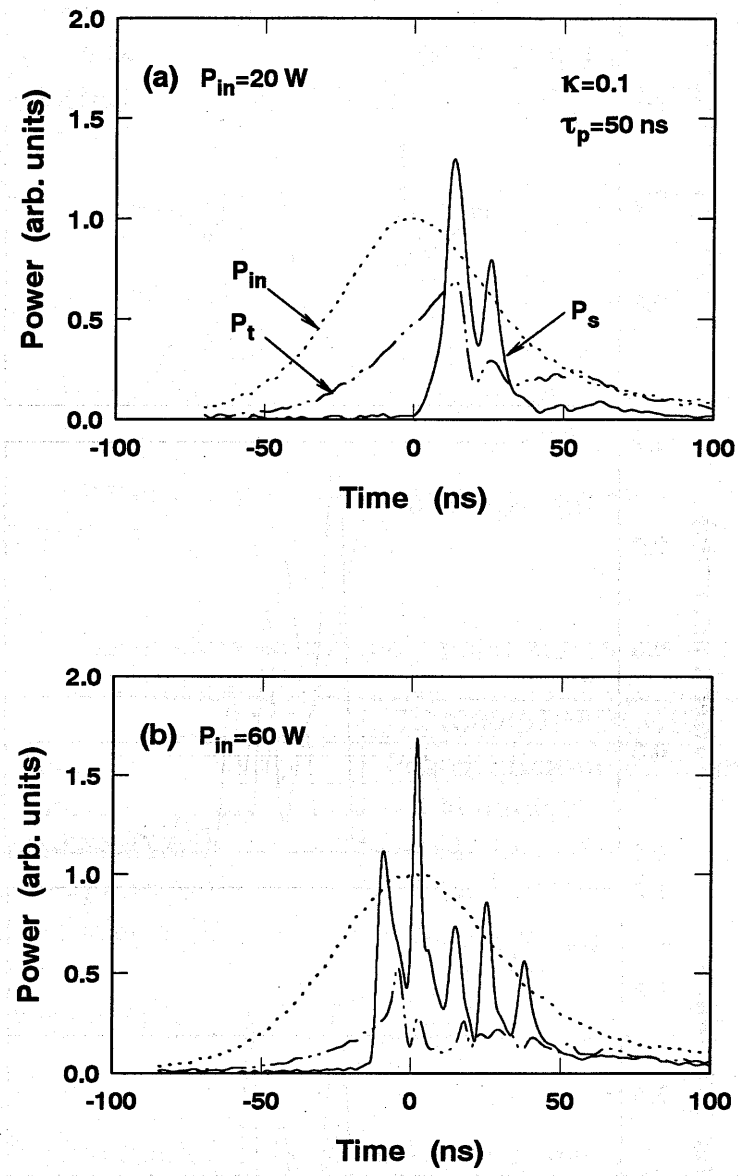

Fig. 6.15. Measured temporal intensity profiles of incident, output pump and Stokes pulses for $\Delta\phi_p = -0.5\pi$, L = 2 m, $\kappa = 0.1$, and $\tau_P = 50$ ns. The input peak powers are (a) 20 W and (b) 60 W.

20 and 60 W. In this case, both the relaxation oscillation and pulsation have also been observed at different level of incident peak power.

In view of the above results, we believe that the theoretical model used here is reasonable.

6.5 Transient Interplay of the Kerr Effect with the SBS Gain Effect in a Fiber Ring Resonator

In this section, we investigate the transient interplay of the Kerr effect with the SBS gain effect in a high-finesse fiber resonator. Using the Brillouin gain coefficients g_{B0} to substitute g_1 and g_2, we rewrite Eqs. (6.1)-(6.3) as

$$\frac{\partial \varepsilon_p^{(m)}(z,t)}{\partial t}+\frac{c}{n_0}\frac{\partial \varepsilon_p^{(m)}(z,t)}{\partial z}=-\frac{\alpha c}{2n_0}\varepsilon_p^{(m)}(z,t)+\frac{g_{B0}}{4\mu_0}\varepsilon_s^{(m)}(z,t)\cdot Q^{(m)}(z,t) -j\frac{n_2\omega_p}{n_0}\left[\left|\varepsilon_p^{(m)}(z,t)\right|^2+2\left|\varepsilon_s^{(m)}(z,t)\right|^2\right]\varepsilon_p^{(m)}(z,t), \tag{6.10}$$

$$\frac{\partial \varepsilon_s^{(m)}(z,t)}{\partial t}-\frac{c}{n_0}\frac{\partial \varepsilon_s^{(m)}(z,t)}{\partial z}=-\frac{\alpha c}{2n_0}\varepsilon_s^{(m)}(z,t)+\frac{g_{B0}}{4\mu_0}\varepsilon_p^{(m)}(z,t)\cdot Q^{(m)*}(z,t) -j\frac{n_2\omega_s}{n_0}\left[2\left|\varepsilon_p^{(m)}(z,t)\right|^2+\left|\varepsilon_s^{(m)}(z,t)\right|^2\right]\varepsilon_s^{(m)}(z,t), \tag{6.11}$$

$$\frac{1}{\Gamma_A}\frac{\partial Q^{(m)}(z,t)}{\partial t}+Q^{(m)}(z,t)=-\varepsilon_p^{(m)}(z,t)\cdot\varepsilon_s^{(m)*}(z,t)+\frac{f(z,t)}{jg_2}, \tag{6.12}$$

with
$$Q^{(m)}(z,t)=\frac{\rho^{(m)}(z,t)}{jg_2}\Gamma_A. \tag{6.13}$$

The boundary conditions for the pump wave and Stokes wave are given in Eqs. (6. 4) and (6.5). In Eqs. (6.11) and (6.12), the Brillouin gain coefficient g_{B0} and the nonlinear refractive index n_2 are the only two factors which decide the interaction between SBS gain effect with Kerr effect. We quantitatively investigate the interplay by changing the magnitudes of these two factors. For simplicity, parameters for the fiber ring cavity are chosen as follows: L = 0.15 m, $\Delta\phi_0$= -0.6π, κ = 0.9, and γ = 0.15.

First, we investigate the effect of Brillouin gain on the temporal output pump signal. Figure 6.16 shows a numerical example for τ_p = 40 ns and the input power P_{in}= 400 W. Temporal profiles of the output pump signal for three magnitudes of g_{B0} are shown in Fig. 6.16(a) and their input-output characteristics are shown in Fig. 6.16(b). It is found that the input-output characteristics depends on the Brillouin gain coefficient. For $g_{B0} = 5.0\times10^{-12}$ m/W, which is one order of magnitude smaller than that of a conventional fused-silica fiber, there exists a bistable hysteresis in the curve of input-output and this hysteresis is identical to the one obtained by neglecting the effect of Brillouin gain (i.e., g_{B0}=0). Optical bistability has been obtained here

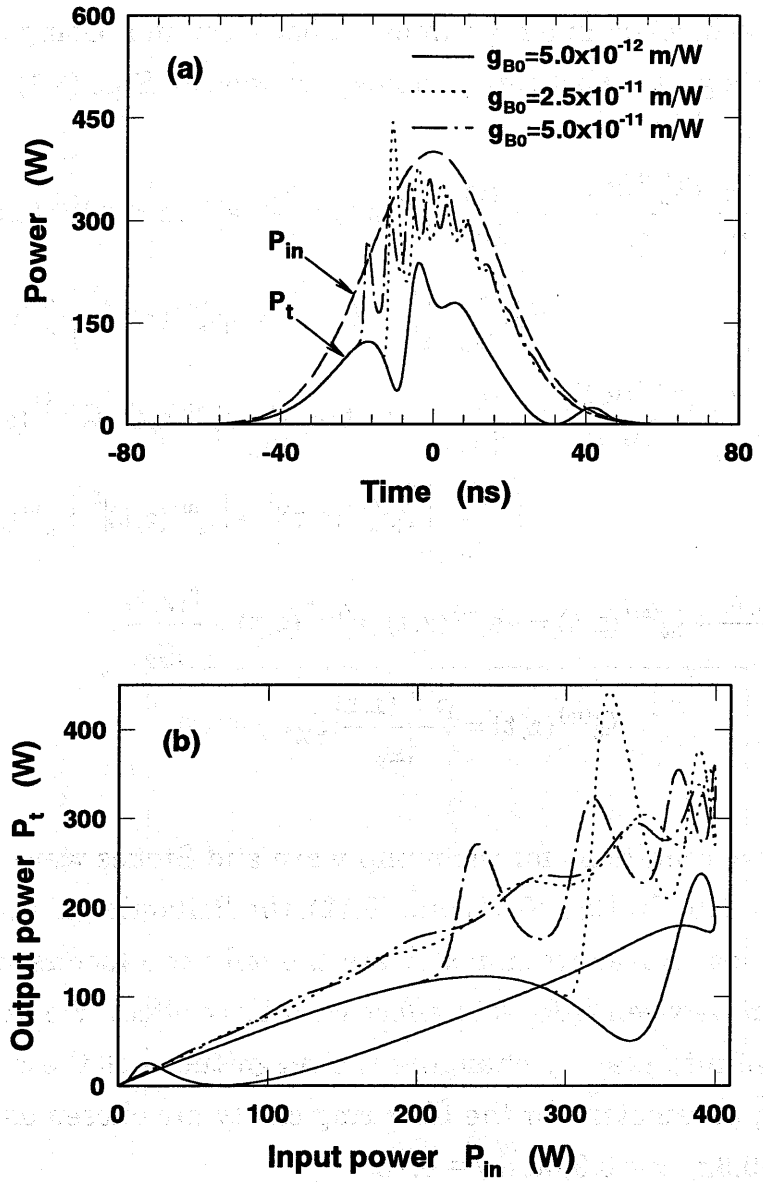

Fig. 6.16. (a) Temporal profiles of the incident and output pump signals for three magnitudes of g_{B0}, where L = 0.15 m, P_{in}= 400 W, $\Delta\phi_p$=-0.6π, τ_P = 40 ns, κ = 0.9, and γ = 0.15. (b) Input-output characteristics of the fiber ring resonator.

as expected from the previous paper [1]. As the Brillouin gain coefficient is increased, the hysteresis begins to disappear due to the occurrence of SBS and a relaxation oscillation appears in the output pump signals. When g_{B0} is increased to 5.0×10^{-11} m/W, which is just the value of SBS gain coefficient for a conventional fused-silica fiber, the hysteresis completely disappears. This result means that the stimulated Brillouin scattering is the most dominant

nonlinear effect in the ring resonator made of fused-silica fiber. Moreover, we perform the same calculation as Fig. 6.16 by increasing the pulse width of incident pulse. Typical example for τ_p =80 ns is shown in Fig. 6.17. It is found that a fine hysteresis loop is obtained for $g_{B0} = 5.0\times10^{-13}$ m/W, which is two order of magnitude smaller than that of a conventional fused-silica fiber.

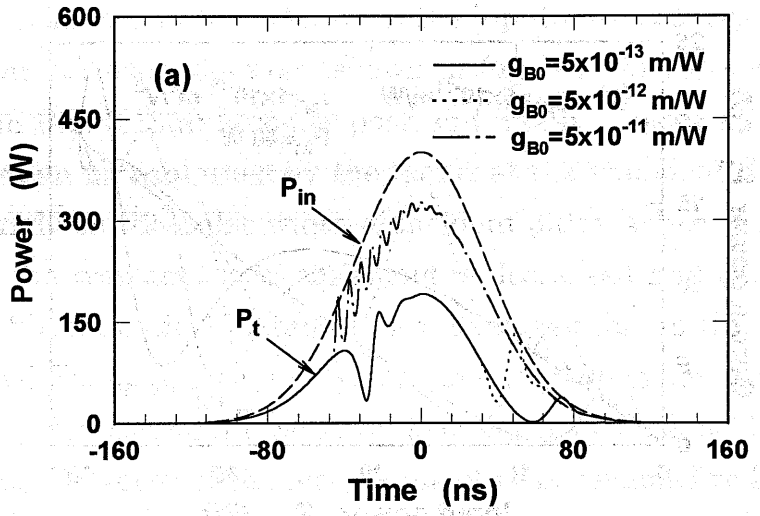

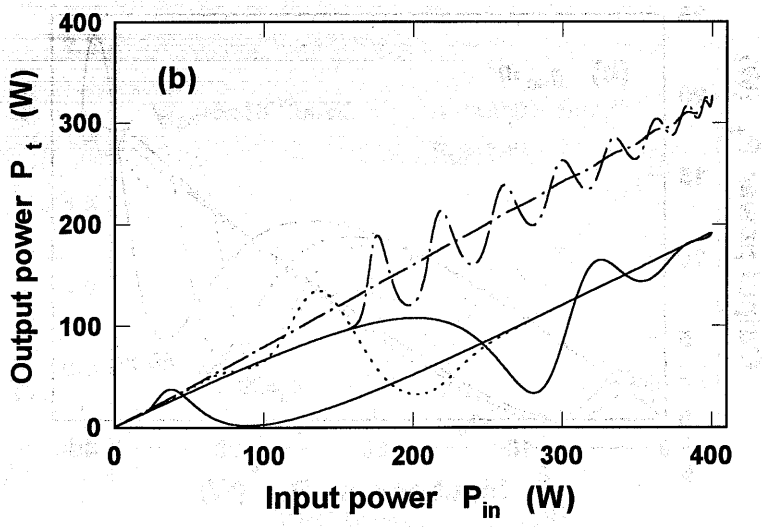

Fig. 6.17. (a) Temporal profiles of the incident and output pump signals for three magnitudes of $g_{B0,}$ where L = 0.15 m, P_{in}= 400 W, $\Delta\phi_p$= -0.6π, τ_P = 80 ns, κ = 0.9, and γ = 0.15. (b) Input-output characteristics of the fiber ring resonator.

However, one cannot obtain a hysteresis like one (shown in Fig. 6.16) for g_{B0} = 5.0×10^{-12} m/W. This phenomenon means that the transient Brillouin gain effect depends on the pulse width of the incident pulse.

Next, we investigate the Kerr effect on the transient input-output characteristics for several values of input pulse duration. A Numerical example is shown in Fig. 6.18(a), where the input peak power P_{in} is 40 W and n_2 is

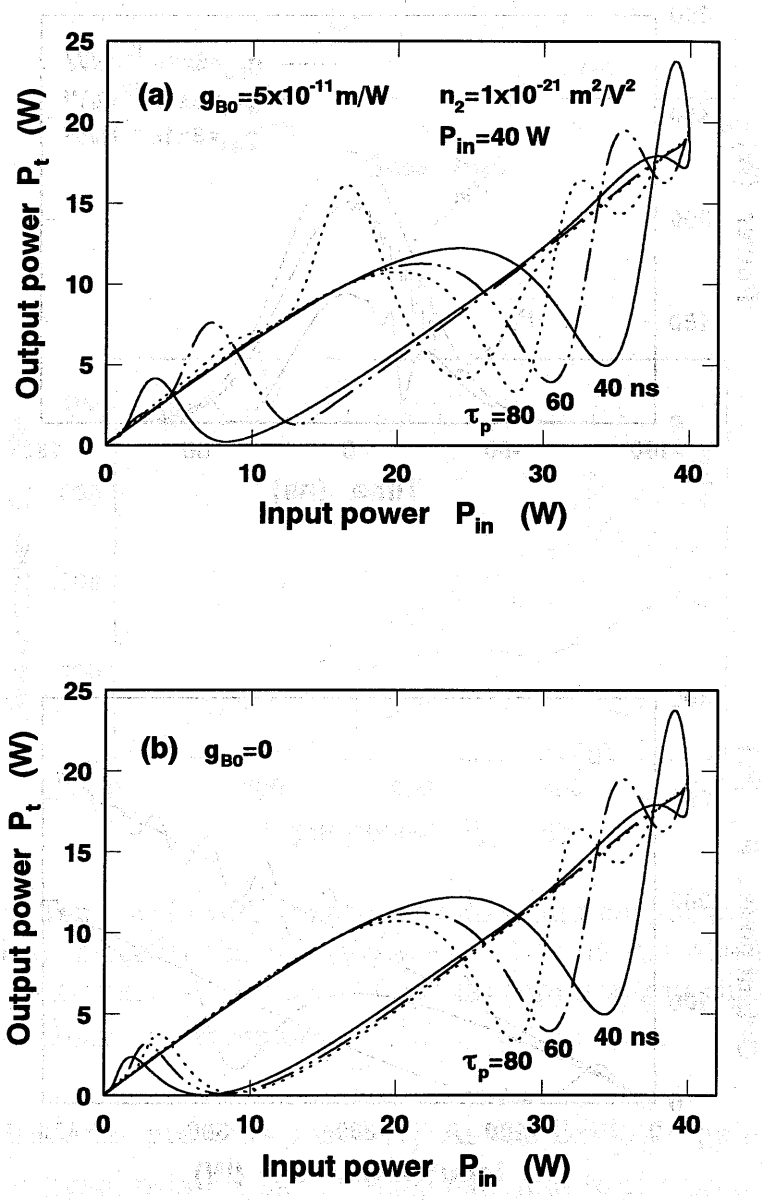

Fig. 6.18. Dependence of input-output characteristics of the fiber ring resonator on the input pulse duration for L = 0.15 m, $\Delta\phi_p = -0.6\pi$, $\kappa = 0.9$, $\gamma = 0.15$, P_{in}= 40 W, and $n_2 = 1\times10^{-21}$ m²/V². The Brillouin gain coefficients are (a) 5×10^{-11} m/W and (b) 0.

assumed to be 1×10^{-21} m^2/V^2, which is one order of magnitude larger than that of a conventional fused-silica fiber. Figure 6.18(b) shows the numerical results only by neglecting the Brillouin gain effect (g_{B0}=0). It is found that there exists a hysteresis loop in the input-output curve for τ_p=40 ns. Compared with the correspondent result shown in Fig. 6.18(b), it is found that the hysteresis loop rarely changes even if the Brillouin gain effect is neglected. This result means that the Kerr effect is dominant for τ_p=40 ns. As the pulse width τ_p is increased, difference between the input-output curve shown in Fig. 6.18(a) and the correspondent one shown in Fig. 6.18(b) appears. The hysteresis shown in Fig. 6.18(a) becomes poor and finally disappears for τ_p=80 ns. These results can be explained by the fact that the transient SBS threshold depends strongly on the pulse width of incident pulse. When the pulse width is increased, the transient SBS threshold is decreased and thus, the cavity conditions to obtain optical bistability are damaged due to the occurrence of SBS. This is why we can obtain a hysteresis for τ_p=40 ns but cannot obtain it for τ_p=80 ns by decreasing the magnitude of g_{B0} or increasing the magnitude of n_2 one order. However, if the magnitude of n_2 is assumed to be two orders magnitude larger than that of a conventional fused-silica fiber, optical bistability can been obtained even if the pulse width is larger than 200 ns. The numerical example is shown in Fig. 6.19, where the input peak power is 4 W,

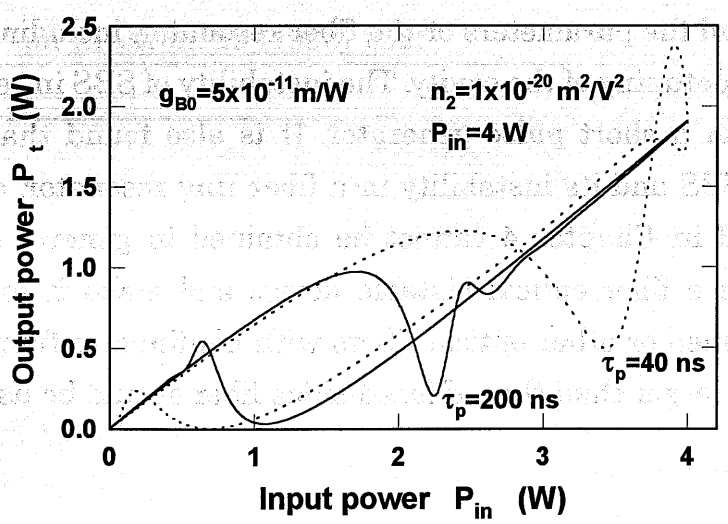

Fig. 6.19. Dependence of input-output characteristics of the fiber ring resonator on the input pulse duration for L = 0.15 m, $\Delta\phi_p$= -0.6π, κ = 0.9, γ = 0.15, P_p= 4 W, and n_2 =1×10^{-20} m^2/V^2.

$n_2 = 1\times10^{-20}$ m^2/V^2, and τ_p=40 and 200 ns. It is found that there exists a hysteresis in the input-output curve for both of these pulse widths and the hysteresis loop decreases with increasing the pulse width of incident pulse. Since these results completely agree with those obtained by neglecting the Brillouin gain effect [1], it is believed that Kerr effect become the most dominant effect for $n_2 = 1\times10^{-20}$ m^2/V^2.

In conclusion, it is found that due to the occurrence of SBS, optical bistability is hardly observed in a fiber ring resonator made of fused-silica fiber. However, if other optical fibers with nonlinear refractive index at least one order larger than that of fused-silica fiber is used, transient optical bistability may be obtained at low power. As matter of fact, large nonlinearity with two order larger than that of silica fiber has already been found in chalcogenide glass fibers [8], which make the exploitation of fiber optical bistable device probable.

6.6 Conclusion

We have investigated theoretically transient SBS in a fiber ring resonator. It is found that owing to the interaction of the nonlinear refraction with the SBS gain effect, a Stokes wave in the ring resonator is generally unstable for a high incident power. It is also found that the instability of SBS including the periodic (self-pulsing) and chaotic behaviors depend strongly on the pump power and the parameters of the fiber resonator, including the finesse and the initial detuning of the cavity. The instability of SBS in resonator may be used to form a short pulse generator. It is also found that due to the occurrence of SBS and its instability in a fiber ring resonator, optical bistability described in Chapter 4 cannot be obtained in general situation. In order to design a fiber optical bistable device and make it practical, SBS must be restrained or other optical fibers with nonlinear refractive index at least one order larger than that of fused-silica fiber should be used.

References

[1] K. Ogusu, "Dynamic behavior of reflection optical bistability in a nonlinear fiber ring resonator," IEEE J. Quantum Electron. 32 (1996) 1537.

[2] K. Ogusu, H. Li, and T. Kamizono, "Analysis of transient optical bistability and stability in a nonlinear fiber Fabry-Perot resonator based on an iterative method," Opt. Rev. 5 (1998) 185.

[3] H. Li and K. Ogusu, "Analysis of optical instability in a double-coupler nonlinerar fiber ring resonator," Opt. Commun. 157 (1998) 27.

[4] H. Li and K. Ogusu, "Dynamic behavior of stimulated Brillouin scattering in a single-mode optical fiber," Jpn. J. Appl. Phys. Part I, 38, (1999) 6309.

[5] G. P. Agrawal, *Nonlinear Fiber Optics* (Academic, New York, 1995) Chap. 9.

[6] C. Montes, D. Bahloul, I. Bongrand, J. Botineau, G. Cheval, A. Mamhoud, E. Picholle, and A. Picozzi, "Self-pulsng and dynamic bistability in cw-pumped Brillouin fiber ring lasers," J. Opt. Soc. Am. B 16 (1999) 932.

[7] S. Randoux, V. Lecoeuche, B. Segard, and J. Zemmouri, "Dynamical analysis of Brillouin fiber lasers: An experimental approach," Phys. Rev. A 51 (1995) 4345.

[8] M. Asobe, T. Kanamori, and K. Kubodera, "Applications of highly nonlinear Chalcogenide glass fibers in ultrafast all-optical switches," IEEE J. Quantum Electron. 29 (1993) 2325.

Chapter 7. Conclusions

In this study, transient properties and instability of the fiber Fabry-Perot resonator and double-coupler fiber ring resonator have be studied in details. The transient effect of stimulated Brillouin scattering and the interplay between Kerr effect and Brillouin gain effect in a fiber and one-coupler fiber ring resonator have also been investigated in details to give a guidance to the design of optical bistable devices. All our results obtained are summarized as follows:

1. A nonlinear transmission experiment and z-scan experiment are preformed to clarify the origin of the nonlinearities of a BDN-nitrobenzene solution in the nanosecond regime. It is found that the main origin of the nonlinear refractive index change is not the population redistribution of the dye molecules but the thermal effect. In particular, the nonlinear refraction in the nanosecond regime is attributed to density change due to propagation of an acoustic wave excited by the laser pulses. We think that the dye is not suitable as a nonlinear material to develop a novel bistable optical device with a response time less than a few nanoseconds.

2. An iterative method have been described for calculating the dynamic properties of fiber Fabry-Perot resonator when an optical pulse with an arbitrary temporal profile is incident on it. Further, a linear stability analysis was performed to examine whether Ikeda instability affects bistable device application or not. It is found that Ikeda instability hardly affect bistable device application because the instability threshold is two orders of magnitude larger than the switching power.

3. The iterative method has been presented for calculating the dynamic properties of the double-coupler nonlinear fiber ring when an optical pulse with an arbitrary temporal profile is incident on it. On the basis of the iterative method, a steady-state analysis and linear stability analysis have also been presented. It is found that optical bistability is hardly affected by Ikeda instability since the instability threshold is much higher than the bistability switching power for the initial detuning where the

bistable device is operated. It is also found that the general features of the instability in the bistable device are similar to that of the nonlinear Fabry-Perot resonator.

4. Dynamics of SBS in a single-mode fiber has been theoretically and experimentally investigated under Gaussian pulse irradiation. Theoretical and experimental results revealed that SBS could occur even in the nanosecond region. It was determined that the steady state of SBS can be obtained when the pulse width of the incident light is greater than 100-fold that of the round-trip time within the fiber. Following the process of the transient SBS, pulse narrowing for the transmitted pulse is observed. Moreover, it was numerically demonstrated that the instability of SBS is closely connected with the magnitude of the nonlinear refractive index. SBS instability can occur when the nonlinear refractive index is one order of magnitude larger than that of the fused-silica fiber.

5. Transient SBS and the transient interplay between Kerr effect and Brillouin gain effect in a fiber ring resonator have been theoretically and experimentally investigated. It is found that owing to the interaction of the nonlinear refraction with the SBS gain effect, cw Stokes wave is generally unstable for a high incident power. These instability including the periodic (self-pulsing) and chaotic behaviors depend strongly on the pump power and the parameters of the fiber resonator, including the finesse and the initial phase detuning of the cavity. It is also found that due to the occurrence of SBS in a fiber ring resonator, optical bistability cannot be obtained in a fused-silica fiber resonator. In order to design a fiber optical bistable device and make it practical, SBS must be restrained or other optical fibers with nonlinear refractive index at least one order larger than that of fused-silica fiber should be used. Since such large nonlinearities have been found in other kind of fiber, such as chalcogenide glass fibers, we believe that experimental demonstration of optical bistability in this device is possible. Moreover, further study for the restraint of SBS in a fiber ring resonator is needed.

博 士 論 文 目 録

静岡大学大学院
理工学研究科博士後期課程

専攻： システム科学専攻　　氏名：李 洪譜 (Hongpu Li)

既発表論文				
題名	著者名	発表学会誌名	公表年月	関連する章
(A) 論文				
1. Analysis of transient optical bistability and stability in a nonlinear fiber Fabry-Perot resonator based on an iterative method	K. Ogusu, H. Li, T. Kamizono	Opt. Rev., Vol. 5, No. 3, pp. 185-190	1998. 6	Chap. 3
2. Optical nonlinearities of Bis(4-dimethylaminodithiobenzil)-nickel solution in the nanosecond regime	H. Li, K. Ogusu	Jpn. J. Appl. Phys. Part I, Vol. 37, No. 10, pp. 5572-5577	1998. 10	Chap. 2
3. Analysis of optical instability in a double-coupler nonlinerar fiber ring resonator	H. Li, K. Ogusu	Opt. Commun., Vol. 157, No. 1-6, pp. 27-32	1998. 12	Chap. 4
4. Dynamic behavior of stimulated Brillouin scattering in a single-mode optical fiber	H. Li, K. Ogusu	Jpn. J. Appl. Phys. Part I, Vol. 38, No. 11, pp. 6309-6315	1999. 11	Chap. 5
(B) その他の論文 [投稿中のもの]				
5. Instability of stimulated Brillouin scattering in a fiber ring resonator	H. Li, K. Ogusu	Submitted		Chap. 6
6. Transient stimulated Brillouin scattering in a fiber ring resonator and its effect on optical bistability	H. Li, K. Ogusu	Submitted		Chap. 6
[学位論文に関係ない論文]				
7. Experimental study of optical parallel cache memory arrays (in Chinese)	M. Cao, Y. Li, X. Liu, H. Li	Acta Optica Sinica, Vol. 11, No. 9, pp. 790-793	1991. 1	
8. Optical perfect shuffle-exchange interconnect network using liquid crystal spatial light switch	M. Cao, F. Luo, H. Li, S. Wang	Appl. Opt., Vol. 31, No. 32, pp. 6817-6819	1992. 11	
9. Optical implement of perfect shuffle/ exchange omega interconnection network (in Chinese)	M. Cao, H. Li, F. Luo, L. Lian	Acta Optica Sinica, Vol. 12, No. 12, pp. 1129-1134	1992. 12	
10. The research of Titanium-doped sapphire laser pumped by Ar^{+3} Laser (in Chinese)	H. Li, M. Cao, F. Luo, J. Ai, J. Xu	Appl. Laser, Vol. 13, No .6, pp. 262-263	1993. 12	

11. The research of high power Q-switched and mode-locked cw Nd:YAG laser (in Chinese)	H. Li, S. Dong, X. Lan	Appl. Laser, Vol. 13, No. 3, pp. 139-141	1993. 6	
12. The optimum design of thermal-insensitive resonator in active mode-locked Nd:YAG laser (in Chinese)	H. Li, X. Lan, S. Dong, Y. Liu	Laser & Infrared, Vol. 23, No. 3, pp. 31-34	1993. 6	
13. The experimental study of the active semiconductor bistable amplifier of InGaAsP/InP (in Chinese)	H. Li, M. Cao, F. Luo, Y. Li	Chinese Journal of Quantum Electronics, Vol. 10, No. 4, pp. 325-327	1993. 8	
14. Parallel processing for polynomial evaluation with a novel optical interconnection: the inverse perfect shuffle	H. Li, M. Cao, F. Luo, J. Ai, J. Xu	Opt. Commun., Vol. 103, No. 5-6, pp. 350-354	1993. 12	
15. Fabrication and research of large array two-dimensional Dammann grating (in Chinese)	F. Luo, M. Cao, H. Li, Z. Li	Semi. Optoelectronics, Vol. 15, No. 1, pp. 55-58	1994. 2	
16. The instantaneous pulse evolution formation of optical pulses for active mode-locked laser (in Chinese)	H. Li, X. Lan, Y. Liu	Chinese Laser & Technolory, Vol. 18, No. 1, pp. 12-16	1994. 1	
17. A general algorithm to the topological equivalence of optical interconnection networks	J. Ai, M. Cao, H. Li, F. Luo, Z. Li	Opt. Commun., Vol. 105, No. 1-2, pp. 39-46	1994. 2	
18. A novel superlarge spots arrays beam splitting (in Chinese)	F. Luo, M. Cao, Y. Li, H. Li, Z. Li	J. High Technology, Vol. 7, No. 4, pp. 26-28	1994. 4	
19. Implement of the optical banyan nonblocking four ports switching network (in Chinese).	H. Li, M. Cao, F. Luo,J. Xu, Z. Li	Acta Optica Sinica, Vol. 14, No. 4, pp. 416-420	1994. 4	
20. Free-space regular optical interconnections: a mathematical analysis	M. Cao, H. Li, F. Luo, D. Liu	Appl. Opt., Vol. 33, No. 14, pp. 2960-2967	1994. 5	
21. Dammann grating beam splitter with 65×65 spot arrays (in Chinese)	F. Luo, M. Cao, H. Li, Z. Li	J. High Technology, Vol. 7, No. 6, pp. 1-4	1994. 6	
22. Analysis on the stability of active semiconductor bistable amplifier (in Chinese)	H. Li, M. Cao, Y. Li, F. Luo	Acta Photonica Sinica, Vol. 23, No. 3, pp. 278-282	1994. 6	
23. Computer generated holographic Fresnel lens and its application in the micro-optic interconnection (in Chinese)	H. Li, M. Cao, F. Luo, Y. Li, Z. Li	Optronics & Lasers, Vol. 5, No. 3, pp. 154-163	1994. 6	
24. The matrix analysis for optical free-space switching network and optical crossover network with four-function interchange nodes	M. Cao, H. Li, J. Ai, F. Luo, L. Wu, W. Gao	Optics & Laser Technology, Vol. 26, No. 4, pp. 271-280	1994. 8	

25. The research on free-space crossover micro-optical interconnection package (in Chinese)	H. Li, M. Cao, X. Zhao, F. Luo, Z. Li	Chinese Journal of Lasers, Vol. 22, No. 5, pp. 155-160	1995. 2	
26. Measurement of diffractive efficiency for Fresnel microlens arrays (in Chinese)	F. Luo, M. Cao, X. Zhao, H. Li, Z. Li	Chinese Journal of Lasers, Vol. 22, No. 5, pp. 343-346	1995. 5	
27. The implement of four-function interchange nodes based on an optical crossover switching network (in Chinese)	H. Li, M. Cao, J. Xu, F. Luo, Z. Li	Chinese Journal of Lasers, Vol. 22, No. 7, pp. 546-550	1995. 7	
28. A novel free-space comega network and its optical implementation	M. Cao, Y. Li, F. Luo, A. Wan, H. Li	Opt. Rev., Vol. 4, No. 3, pp. 349-353	1997. 6	
29. Optical inverse perfect shuffle interconnection and its application to polynomial evaluation	H. Li, M. Cao, F. Luo, K. Ogusu	Opt. Rev., Vol. 5, No. 3, pp. 138-142	1998. 6	
(C) 研究会及び口頭発表				
1. Nonlinearity of saturable absorber BDN and its application to bistable optical devices	H. Li, H. Shao, K. Ogusu	電子情報通信学会総合大会、C-4-70	1997. 3	Chap. 2
2. Experimental study of laser-induced thermal effect in BDN dye solution by z-scan method	H. Li, K. Ogusu	電子情報通信学会総合大会、C-4-4	1998. 3	Chap. 2
3. 反復法よる非線形ファブリ・ペロ共振器の光双安定性と不安定性の解析	神園 隆司、李 洪譜、小楠 和彦	電子情報通信学会総合大会、C-4-6	1998. 3	Chap. 3
4. Experimental study of laser-induced thermal effect in BDN dye solution by z-scan methods	H. Li, K. Ogusu	Technical report of IEICE, OPE98-22, pp. 41-46	1998. 6	Chap. 2
5. フアイバ形ファブリ・ペロ共振器の光双安定性の過渡特性と不安定性	神園 隆司、李 洪譜、小楠 和彦	電子情報通信学会技術報告、OPE98-22 pp. 35-41	1998. 6	Chap. 3
6. Optical bistability and instability in a double-coupler nonlinear fiber ring	H. Li, K. Ogusu	電子情報通信学会エレクトロニクスソサイエテイ大会、C-4-31	1998. 9	Chap. 4
7. Transient stimulated Brillouin scattering in a single-mode optical fiber	H. Li, K. Ogusu	Technical report of IEICE, OPE99-22, pp. 91-98	1999. 1	Chap. 5
8. Transient stimulated Brillouin scattering in a single-mode optical fiber	H. Li, K. Ogusu	電子情報通信学会総合大会、C-4-37	1999. 3	Chap. 5
9. Transient stimulating Brillouin scattering in a fiber ring resonator	H. Li, K. Ogusu	電子情報通信学会エレクトロニクスソサイエテイ大会、C-3-82	1999. 9	Chap. 6